

# Evaluation and analysis of vibrationally resolved electronic spectra with ab initio semiclassical dynamics

THÈSE N° 6737 (2015)

PRÉSENTÉE LE 2 OCTOBRE 2015

À LA FACULTÉ DES SCIENCES DE BASE

LABORATOIRE DE CHIMIE PHYSIQUE THÉORIQUE

PROGRAMME DOCTORAL EN CHIMIE ET GÉNIE CHIMIQUE

ÉCOLE POLYTECHNIQUE FÉDÉRALE DE LAUSANNE

POUR L'OBTENTION DU GRADE DE DOCTEUR ÈS SCIENCES

PAR

Marius WEHRLE

acceptée sur proposition du jury:

Prof. L. Helm, président du jury  
Prof. J. Vanicek, directeur de thèse  
Dr F. Grossmann, rapporteur  
Prof. M. Ceotto, rapporteur  
Prof. U. Röthlisberger, rapporteuse



ÉCOLE POLYTECHNIQUE  
FÉDÉRALE DE LAUSANNE

Suisse  
2015



*Every time I see a math word problem it looks like this: If I have 10 ice cubes and you have 11 apples. How many pancakes will fit on the roof?*

*Answer: Purple because aliens don't wear hats. [arrg! e-cards]*



---

# Acknowledgements

First and foremost, I thank Jiří for all the discussions about science and also about “God and the world”. You made me to rethink many of my points of view and for this, I am grateful. Thanks for accepting me as a greenhorn; I really appreciate the time in the LCPT group.

A very important acknowledgement should be devoted to Miroslav. You helped me a lot with your scientific and technical knowledge. You evaluated with patience all my ideas that ranged from “too crazy” to “could work”. Besides science, we spent also many good times cycling and having beers.

Moreover, the other members of the LCPT group have also made important contributions to my life in numerous ways. Especially Alberto and Eduardo who now participate together with Miroslav and me in the SThAR project. I am also grateful to Cesare, Tomáš, Ray, Aurélien, Konstantin and Solène for being excellent colleagues.

The LCPT group wouldn't thrive without Sylvie. Many thanks for all your help with the tedious administration.

To all my friends, Russian, Colombian, Czech, Spanish, French, Portuguese, Italian, Chinese, Swiss, and from other places as well, thanks for all the good moments.



---

# Abstract

Linear and nonlinear spectroscopy techniques are widely used to study numerous important chemical and physical processes. However, the interpretation of these experimental spectra often becomes very complicated because a particular spectrum constitutes a mere footprint of a host of various, possibly intertwined, effects. In this spirit, calculations in the time-dependent picture provide a useful tool for decoding such spectra. Nevertheless, the ultimate challenge is to devise a theoretical framework that could yield sufficient efficiency as well as accuracy to describe the molecular system of interest in a satisfactory way.

The strategy is relatively straightforward for low dimensional systems that are directly tractable, e.g., with exact quantum dynamics performed on an equidistant grid. Despite the formidable overall exponential scaling, these calculations can be significantly accelerated by using higher-order split-operator propagation schemes. In general however, one is forced to seek an affordable balance between physical accuracy on one hand and computational efficiency on the other by employing, for instance, some of the techniques from the broad family of semiclassical methods based on classical trajectories.

To this end, the thawed Gaussian approximation (TGA) is combined with an on-the-fly ab initio scheme (OTF-AI). The resulting OTF-AI-TGA algorithm is efficient enough to treat all vibrational degrees of freedom (DOFs) on an equal footing even in case of larger molecules such as pentathiophene (105 DOFs). Moreover, in sharp contrast to popular approaches based on global harmonic approximation, OTF-AI-TGA reproduces almost perfectly the absorption and photoelectron spectra of ammonia, i.e., spectra with strong dependence on large amplitude motions.

In addition to the mere reproduction of experimental spectra, a novel systematic approach is introduced to assess the importance and the dynamical couplings of individual vibrational DOFs. This is in turn used to gain a deeper insight into the associated physical and chemical processes by attributing specific spectral features to the underlying molecular motion. Specifically, in the case of oligothiophenes, this approach was used to assign the dynamical interplay between quinoid and aromatic characters of individual rings to par-

---

ticular spectral patterns and, furthermore, to explain the changes in the vibrational line shape with an increasing number of rings.

Furthermore, in systems that are too large to be treated with accurate quantum methods, efficient methods such as OTF-AI-TGA are expected to be useful as a preliminary tool for identification of the subspace of the important DOFs. On this subspace, one can then unleash some of the less efficient yet better-suited methods. In summary, OTF-AI-TGA combined with this novel analysis approach is intended to provide the first crucial step in a hierarchical computational protocol for studying large molecules such as dyes.

**Keywords:** On-the-fly *ab initio* semiclassical dynamics, accelerating quantum dynamics, split-operator method, linear spectroscopy, oligothiophene, ammonia, thawed Gaussian approximation



---

## Résumé

Les techniques de spectroscopie linéaire et non-linéaire sont de nos jours très répandues afin d'étudier de nombreux processus physique et chimique importants. Cependant, une interprétation des spectres obtenus est souvent très compliquée car un spectre donné constitue l'empreinte d'une multitude d'effets différents et éventuellement entrelacés. Dans cette optique, effectuer des calculs en utilisant une image temporelle nous fournit ainsi un moyen très utile pour décoder de tels spectres. Néanmoins, le but ultime est de concevoir une structure théorique qui se veut efficace et précise afin de décrire le système moléculaire qui nous intéresse de manière satisfaisante.

La stratégie à adapter est relativement directe pour des systèmes à faible dimension. En effet, ces derniers peuvent facilement être obtenus, e.g., par calcul de dynamique quantique exacte sur une grille équidistante. Malgré le fameux mur exponentiel qui est inévitable, ces calculs peuvent être très largement accélérés en utilisant des schémas de propagation du type split-operator d'ordres supérieurs. Cependant, le scientifique est en général obligé de choisir entre la précision physique d'un coté, et l'efficacité computationnelle de l'autre, en employant, par exemple, des techniques qui font parties de la grande famille des méthodes basées sur le calcul de trajectoires obéissant à des lois de la mécanique classique.

A cette fin, l'approximation de “thawed Gaussian” (TGA) est combiné à un schéma *ab initio* réalisé à la volée (OTF-AI). L'algorithme résultant, OTF-AI-TGA, est suffisamment efficace pour traiter tous les degrés de liberté (DOFs) vibrationnels sur un pied d'égalité même dans le cas de grosses molécules comme un pentathiophène (105 DOFs). De plus, OTF-AI-TGA est en net contraste avec les approches basées sur l'approximation harmonique globale puisqu'il est capable de reproduire de manière quasiment parfaite le spectre d'absorption et le spectre de photoélectron de l'ammoniac, i.e., des spectres qui sont grandement dépendants d'une large amplitude de mouvement.

En outre, une nouvelle approche systématique vient s'ajouter à la simple reproduction de spectres expérimentaux. Cette dernière est introduite afin d'évaluer l'importance et le couplage dynamique de chaque DOF vibrationnel individuel. Elle est à son tour utilisée pour acquérir une compréhension plus profonde des processus physiques et chimiques associés

---

en attribuant des caractéristiques spectrales spécifiques au mouvement moléculaire sous-jacent. Plus spécifiquement, dans le cas des oligothiophènes, cette approche a été utilisée pour assigner certains motifs spectraux à l'interaction dynamique entre les caractères quinoides et aromatiques des anneaux individuels ainsi que pour expliquer les changements dans la forme de la ligne vibrationnelle avec l'augmentation du nombre d'anneaux.

Pour des systèmes trop larges pour être traités avec les méthodes quantiques précises, des méthodes comme OTF-AI-TGA sont attendues à être utilisées comme des objets préliminaires permettant d'identifier le sous-espace des DOFs importants. Sur ce sous-espace, il est alors possible d'utiliser une méthode plus coûteuse mais mieux adaptée. En résumé, OTF-AI-TGA combinée à cette nouvelle approche d'analyse est destinée à fournir la première étape dans un protocole de calcul hiérarchique pour étudier les grandes molécules telles que les colorants.

**Mots clés:** Dynamique semiclassique à la volée *ab initio*, accélération de la dynamique quantique, split-operator, spectroscopie linéaire, oligothiophène, ammoniac, approximation de thawed Gaussian

---

# Contents

<b>Acknowledgements</b>	<b>i</b>
<b>Abstract</b>	<b>iii</b>
<b>Résumé</b>	<b>v</b>
<b>List of Figures</b>	<b>ix</b>
<b>List of Tables</b>	<b>xiii</b>
<b>List of Acronyms</b>	<b>xv</b>
<b>Chapter 1 Introduction</b>	<b>1</b>
1.1 Overview	1
1.2 Time-dependent picture of linear spectroscopy	3
1.3 Multi-trajectory semiclassical methods	7
1.3.1 Dephasing representation of quantum fidelity	8
1.4 Thawed Gaussian approximation	10
1.5 On-the-fly scheme	13
1.5.1 On-the-fly <i>ab initio</i> thawed Gaussian wave packet dynamics	14
<b>Chapter 2 Accelerating calculations of ultrafast time-resolved electronic spectra with efficient quantum dynamics methods</b>	<b>19</b>
2.1 Abstract	19
2.2 Introduction	20
2.3 Finding a minimum set of sufficiently accurate electronic surfaces	21
2.4 Accelerating quantum dynamics with high order split operator methods	22
2.5 Semiclassical dynamics for time-resolved spectroscopy	24
2.6 Results and discussion	26
2.6.1 The system	26
2.6.2 Efficiency of various split-operator methods	27
2.6.3 Time-resolved spectra and correlation functions	29
2.7 Conclusion	31
<b>Chapter 3 On-the-fly <i>ab initio</i> semiclassical dynamics: Identifying degrees of freedom essential for emission spectra of oligothiophenes</b>	<b>33</b>
3.1 Abstract	33
3.2 Introduction	34
3.3 Theory	36
3.3.1 Emission spectrum calculation	36

---

3.3.2	Stability matrix propagation: Symplecticity and effect of Hessian interpolation	36
3.3.3	Identification of the essential DOFs	39
3.3.4	TGA in subspaces of reduced dimensionality	42
3.4	Computational details	44
3.5	Results and discussion	45
3.5.1	Comparison with experimental spectra	45
3.5.2	Vibrational analysis	49
3.5.3	Quinoid structure of S1	53
3.5.4	Analysis of the effective conjugation coordinate	54
3.5.5	Time dependence of the width matrix of the OTF-AI-TGA GWP	57
3.5.6	Comparison of the OTF-AI-TGA approach to the global harmonic approximation	57
3.6	Conclusion	59
<b>Chapter 4 On-the-fly ab initio semiclassical dynamics of floppy molecules: Absorption and photoelectron spectra of ammonia</b>		<b>61</b>
4.1	Abstract	61
4.2	Introduction	62
4.3	Theory	64
4.3.1	Absorption and photoelectron spectra calculations	64
4.3.2	Global harmonic potential construction	64
4.3.3	Derivation of the TGA Gaussian wave packet energy	65
4.4	Computational Methods	67
4.5	Results and discussion	68
4.5.1	Absorption spectrum	68
4.5.2	Photoelectron spectrum	69
4.6	Conclusion	71
<b>Chapter 5 Influence of decoupling a thawed Gaussian wave packet dynamics on spectrum calculations</b>		<b>73</b>
5.1	Abstract	73
5.2	Introduction	74
5.3	Theory	75
5.3.1	Spectrum calculation	75
5.3.2	Harmonic model	76
5.3.3	Construction of the information flow matrix B	78
5.4	Computational details	79
5.5	Results and discussion	80
5.5.1	Effect of fully decoupled harmonic models on the spectrum	80
5.5.2	Effect of consecutive decoupling on the spectrum	81
5.6	Conclusions	88
<b>Chapter 6 Conclusion and outlook</b>		<b>91</b>
<b>Chapter 7 Bibliography</b>		<b>95</b>

---

# List of Figures

- Figure 1: Influence of perturbing the harmonic force constant on the correlation function computed with dephasing representation (DR) [Eq. (1.24)]. In the one-dimensional harmonic model (1D), ground state  $g$  and the excited state  $e$  are displaced ( $d = 0.5$ ). Both states have the same harmonic force constant  $k_g = k_e = 1$ . For the two-dimensional model (2D), a further dimension is added that is characterized by a change in the force constants between the states, i.e.,  $k_g = 1$ ,  $k_e = 0.5$ , and by no displacement  $d = 0$ . This new degree of freedom affects strongly the DR result, whereas the exact quantum (QM) correlation function is only slightly perturbed..... 10
- Figure 2 - Error of the quantum wave function (at time  $t = 128$  a.u.) as a function of the time step  $\Delta t$  (in a.u.) for various split-operator methods..... 28
- Figure 3 - Pump-probe stimulated emission spectra: (a) Quantum results (contours are plotted for intensities from -0.34 to 0.2 at intervals of 0.04). (b) Semiclassical results for the delay time of 300 a.u. (the number of trajectories used is shown after the name of the approximation)..... 29
- Figure 4 - The magnitude of the time-dependent correlation function as a function of time computed with various SC methods. (The number of trajectories used is shown after the name of the method.) (a) The slow convergence of the HK method can be remedied by heuristic filtering out of trajectories with exponentially growing prefactors. (b) The improvement of the FGA by renormalization and the fast convergence of the DR. [The displayed correlation functions were multiplied by the damping function (shown by a dashed gray curve) in order to obtain finite-resolution spectra in Figure 3.] ..... 31
- Figure 5: Effects of Hessian interpolation scheme of second order ( $b = 2$ ) for several sizes of the interpolation interval  $s$ . Panel (a): Extent of the violation of the symplectic condition Eq. (3.6). Panel (b): Accuracy of the quantum dynamics measured with fidelity  $F_s$ ,  $b_t$  introduced in Eq. (3.7) ..... 38
- Figure 6: Partitioning of S1 normal-mode coordinates of dithiophene T2 into approximately independent subsets for the threshold value  $\epsilon_B = 0.045$  [see Eq. (3.9)]. Colored circles represent individual modes, i.e., elements of  $D$ . The dynamically important modes [Eq. (3.12)] comprising  $G \epsilon_Q$  with the threshold value  $\epsilon_Q = 0.6$  are shown in red. Finally, solid lines represent inter-mode couplings above the threshold  $\epsilon_B$ . Vibrational frequencies are given in  $\text{cm}^{-1}$ ..... 42
- Figure 7: Emission spectra of the oligothiophene  $T_n$  family for: Comparison of experimental emission spectra (exp., dashed green line) with the full-dimensional OTF-AI-TGA calculations using all  $21n$  normal modes (solid black line) ..... 46
- Figure 8: Emission in the oligothiophene  $T_n$  family for  $n \in \{2, 3, 4, 5\}$ . (a)  $L^\infty$ -normalized line-shape spectra. To facilitate their comparison, the spectra are shifted independently for each  $n$  so that the

---

$\alpha_0$ peak appears at zero energy. (b) Dependence of the vertical-transition energy $E_{\text{vert}}$ and positions of the $\alpha_0$ and $\alpha_1$ -peaks ( $E_{\alpha_0}, E_{\alpha_1}$ ) on $1/n$ (see text for details). Linear fits are denoted with lines. ....	48
Figure 9: Emission spectra of oligothiophenes T2 (a) and T5 (b): comparison of the full-dimensional OTF-AI-TGA spectrum $\sigma_D$ (solid black line) with the spectrum $\sigma_A$ (dotted green line) computed within the subspace $A$ of the active modes and the spectrum $\sigma_{C1 \cup C2}$ (dashed blue line) taking into account only modes belonging to the classes $C1$ and $C2$ (see Figure 11 and Table 3) introduced in Eq. (3.22). ....	50
Figure 10: Characterization of the active normal modes in the set $A \subseteq D$ [see Eqs. (3.14) and (3.22)] by the nature of the deformation which they exert on the oligothiophene $T_n$ skeleton. To cover all cases presented in Table 3, these deformations are shown on the examples of T3 and T4. Panel labels correspond to the classification in Table 3. ....	51
Figure 11: Classification of normal modes of the oligothiophene $T_n$ family according to their influence on the resulting emission spectrum see Eqs. (3.14) and (3.22)]. Detailed description of individual classes is contained in Table 3. (a) Inter-ring stretch modes responsible for the $\alpha$ -peaks shown in Figure 8. (b) Ring-squeeze mode reflected in the $\beta$ -peaks in Figure 8. (c) Remaining modes causing overall broadening of the spectra ....	52
Figure 12: Equilibrium S1 geometry of oligothiophenes $T_n$ family. Corresponding bond lengths for different oligothiophenes $T_n$ are juxtaposed with each other next to individual bonds, whereas the dashed lines represent the end of the half-chain for each $T_n$ . E.g., to the right of the dashed line marked as T3 there are only one or two bond-length values since those bonds are not present in the half-chain of T2 and T3. ....	53
Figure 13: Time dependence of the bond length alternation (BLA) parameter during the dynamics induced by the emission in pentathiophene T5 [see Eq. (3.23) and Figure 12]. The character of the outer rings (rings 1 and 2) is mainly aromatic (positive BLA), while the transition to the quinoid structure (negative BLA) occurs almost exclusively within the inner ring (ring 3). ....	54
Figure 14: Comparison of the static, $v_j$ [see Eq. (3.27)], and dynamic, $v_j$ [see Eq. (3.29)], contribution of individual normal modes to the ECC $R$ of Eq. (3.24) for the oligothiophenes $T_n$ , $n \in \{2,3,4,5\}$ ....	56
Figure 15: Time dependence of the Gaussian “nuclear-density” width $\sigma_{it} = 4\text{Re}A_{iit}$ along the $i$ th mode in oligothiophenes T5. The quantity $\sigma_i$ is shown for the four different modes in which the spreading of the GWP is most pronounced. ....	57
Figure 16: Emission spectra of the oligothiophenes $T_n$ family: Comparison of global harmonic approximation (“S0 planar” and “S0 twisted”) to the OTF-AI-TGA approach and the experimental data. The “S0 twisted” case is shown only for T2. ....	59
Figure 17: Absorption spectrum of $\text{NH}_3$ : Comparison of the experimental spectrum <sup>173</sup> recorded at the temperature of 175 K with the spectra computed with the OTF-AI-TGA, vertical harmonic (VH), and adiabatic harmonic (AH) models within the B3LYP and CASPT2 <i>ab initio</i> methods. All spectra are rescaled so that the highest spectral peak in each spectrum is of unit intensity. ....	69
Figure 18: Photoelectron spectrum of $\text{NH}_3$ : Comparison of the experimental spectrum <sup>166</sup> with the spectra computed with the OTF-AI-TGA, vertical harmonic (VH), and adiabatic harmonic (AH) models	

---

using MP2 and CCSD <i>ab initio</i> methods. All spectra are rescaled so that the highest spectral peak in each spectrum is of unit intensity. ....	70
Figure 19: Time dependence of the classical ( $E_{cl}$ ) and semiclassical ( $E_{sc}$ ) energies for the OTF-AI-TGA and vertical harmonic (VH) model using CCSD level of theory. The total GWP energy EGWP is the sum of $E_{cl}$ evaluated along the central trajectory and $E_{sc}$ resulting from the nuclear GWP width. The TGA is exact for quadratic PESs and, consequently, EGWP is constant in the VH model. For general potentials, however, $E_{cl}$ stays constant, whereas $E_{sc}$ increases with time due to the time dependence of the effective potential. ....	71
Figure 20: Spectrum of the harmonic model system: Comparison of the exact spectrum with the spectra calculated within three different decoupled harmonic models by neglecting the Duschinsky rotation ( $J = 1$ ), neglecting the dynamical couplings (“negl. dyn. coup.”), or neglecting the initial couplings (“negl. init. coup.”). ....	80
Figure 21: Density plots showing the extent of the couplings between different DOFs. The couplings are estimated by different choices for the information flow matrix $B$ [Eqs. (5.9), (5.10), (5.12), (5.13)]. Here, the couplings arise due to the propagation of the GWP on the coupled harmonic potential, i.e., the dynamical couplings. The 15 normal mode coordinates $q_{S1}$ are labeled consecutively starting with the coordinate associated with the lowest frequency. Darker shades correspond to stronger couplings between two DOFs. ....	82
Figure 22: Error in the spectrum calculation [defined in Eq. (5.14)] introduced as a function of the extent of the decoupling $c_D, \epsilon_B$ [Eq. (5.1)]. Here, the couplings arise due to the propagation of the GWP on the coupled harmonic potential, and these dynamical couplings are measured by $B_p, B_M, B_B, B_J$ introduced in Subsection 5.3.3. ....	84
Figure 23: Adjacency matrices [Eq. (5.2)] as a function of the extent of the decoupling $c_D, \epsilon_B$ (1 to 15) and different measure of couplings ( $B_p, B_M, B_B, B_J$ ) introduced in Subsection 5.3.3. Each adjacency matrix shows which pairs of modes are coupled (black squares) and which are decoupled (white squares). In the panel “dynamical couplings” the couplings arise due to the propagation of the GWP on the coupled harmonic potential; the couplings in the panel “initial couplings” are due to the properties of the initial GWP. The frequencies of the corresponding normal mode coordinates increase from top to bottom and from left to right. ....	85
Figure 24: Error in the spectrum [defined in Eq. (5.14)] as a function of computational cost of spectrum calculations estimated using Eq. (5.15). The error in the spectrum calculations is due to neglecting the couplings among the DOFs, i.e., forming uncoupled subsets. The couplings are measured by $B_p, B_M, B_B, B_J$ , and they are due here to the propagation of the GWP on the coupled harmonic potential, i.e., dynamical couplings. ....	86
Figure 25: Density plots showing the extent of the couplings between different DOFs. The couplings are estimated by two different choices for the information flow matrix $B$ [Eqs. (5.12), (5.13)]. Here, the couplings are due to the properties of the initial GWP, which are then propagated on an uncoupled PES, i.e., initial couplings. The 15 normal mode coordinates $q_{S1}$ are labeled consecutively starting with the coordinate associated with the lowest frequency. Darker shades correspond to stronger coupling between two DOFs. ....	87
Figure 26: Error in the spectrum calculation [defined in Eq. (5.14)] introduced as a function of the extent of the decoupling $c_D, \epsilon_B$ [Eq. (5.1)]. Here, the couplings are the initial couplings, due to the properties of the initial GWP, which is then propagated on an uncoupled PES. These couplings were measured using $B_p$ or $B_J$ introduced in Subsection 5.3.3. ....	87

---

Figure 27: Overview of the analysis approach: First, groups of the most important DOFs are identified on the basis of OTF-AI-TGA dynamics. Second, the underlying classical motion within the DOFs comprising these groups is attributed to specific spectral features. .... 92

Figure 28: Time-resolved stimulated emission spectrum [Eq. (2.3)] of dithiophene computed with OTF-AI-TGA using b3lyp/6-31+G(d,p) *ab initio* setup. The larger the delay time  $\tau$  between the pump and the probe pulses, the better the resolution of the spectrum. Such effects were already reported in experiments with similar molecules.<sup>181</sup> ..... 92



---

# List of Tables

Table 1: CPU time in second for gradient or Hessian evaluations performed with Gaussian09 package <sup>65</sup> for different OTF-AI-TGA calculations presented in this thesis. These calculations were done on an AMD Opteron 2427 CPU running at 2.2 GHz. ....	17
Table 2: Parameters (in a.u.) of the approximative potential fit from Eq. (12). ....	27
Table 3: Normal-mode classification based on decompositions (3.14) and (3.22) with $\epsilon B = 0.55$ and $\epsilon \rho = 0.6$ for the oligothiophene $T_n$ family, Vibrational frequencies $\omega_i$ are given in $\text{cm}^{-1}$ , while the maximum relative displacements $\rho_i$ of Eq. (3.11) are dimensionless. The modes are further classified into 7 groups by the character of the deformation which they exert on the oligothiophene skeleton. These groups are distinguished by superscript labels next to frequency values. For schematic depiction of these deformations see Figure 10. ....	52
Table 4: Contribution of the $i$ th group $\mathcal{A}_i$ to ECC in terms of $\kappa_i$ introduced in Eq. (3.30). ....	56
Table 5: Overall energy shifts in eV introduced into the spectra. ....	67
Table 6: Frequencies $\omega$ , given in $\text{cm}^{-1}$ , and relative displacements Eq. (5.16) corresponding to the normal mode coordinates of $S_0$ , i.e., $qS_0$ , and $S_1$ , i.e., $qS_1$ . ....	88

---

---

# List of Acronyms

AI	<i>Ab initio</i>
BLA	Bond length alternation
CD	Cellular dynamics
CHK	Cellularized Herman-Kluk
CL	Classical
DFT	Density functional theory
DOF	Degree of freedom
OTF-AI-TGA	On-the-fly <i>ab initio</i> thawed Gaussian approximation
DR	Dephasing representation
ECC	Effective conjugation coordinate
FFT	Fast Fourier Transform
FGA	Frozen Gaussian approximation
GWP	Gaussian wave packet
HA	Global harmonic approximation
HK	Herman-Kluk
HWHM	Half-width at half-maximum
LHA	Local harmonic approximation
OTF	On-the-fly
PES	Potential energy surface
QD	Quantum dynamics
SC	Semiclassical
TD-DFT	Time-dependent DFT
TDPT	Time-dependent perturbation theory
TDSE	Time-dependent Schrödinger equation
TGA	Thawed Gaussian approximation
T <sub>n</sub>	Oligothiophene with n number of rings



---

# Chapter 1 Introduction

## 1.1 Overview

Electronic spectroscopy, ranging from simple absorption and emission to multi-photon time-resolved spectroscopy, belongs among the most important experimental tools for studying chemical and physical processes that occur on the femtosecond ( $10^{-15}$  second) time scale. Such ultrafast spectra contain valuable information about the molecular structure, electronic states, or underlying dynamics. Theoretical methods then help not only to predict the experimentally measured spectra but also to do the nontrivial “decoding” of such spectra by attributing specific spectral features to particular dynamic processes, for example.

Before even starting such simulations, one is faced with two main questions: First, which theoretical method reproduces the experimental spectrum with desired accuracy. Second, how does the simulation have to be analyzed to gain new insight? Clearly, the dimensionality of the system of interest constitutes one of the main limiting factors for both questions.

For low-dimensional systems, the most accurate and straightforward approach is to solve directly the time-dependent Schrödinger equation (TDSE)

$$i\hbar \frac{d}{dt} |\psi(t)\rangle = \hat{H} |\psi(t)\rangle. \quad (1.1)$$

We show in Chapter 2 that using higher-order split-operator methods can significantly accelerate quantum dynamics performed on a fixed equidistant grid. However, these acceleration techniques cannot ameliorate the inherent exponential scaling of the computational costs with dimensionality. Thus the dimensionality of the system is typically still limited to a few, say, 5 degrees of freedom (DOFs).

In practice, one has to resort to methods that provide a good compromise between accuracy and computational efficiency. Of these, the broad family of trajectory-based semi-

---

classical methods remains a popular choice. Such methods typically employ an ensemble of classical trajectories augmented with a complex phase factor that gives rise to interference effects. Although not exact, these methods can describe various quantum effects that are inaccessible to standard classical molecular dynamics. It should be noted that the accuracy typically deteriorates at longer times. However, thanks to the ultrafast character of the dynamics, this is in practice of minor importance.

Although trajectory-based semiclassical methods tend to be computationally much more efficient than full quantum dynamics and, hence, open the door to larger systems, the number of classical trajectories required for convergence usually grows rapidly with dimensionality. Thus, one is restricted to rather small chemical systems comprised of a few atoms. How then to include quantum effects, at least to some extent, in case of large systems? We can either use:

1. Highly efficient multi-trajectory semiclassical methods, e.g., the dephasing representation (DR) of quantum fidelity (see Subsection 1.3.1). This semiclassical method, for which the number of trajectories required for converging the calculation is, perhaps counterintuitively, independent of dimensionality.
2. Semiclassical methods based merely on a single trajectory, e.g., the thawed Gaussian approximation (TGA) (see Section 1.4).

Thanks to their favorable properties, these methods can be applied to molecules as large as dyes. TGA especially is a promising method for computing absorption or emission spectra of larger (Chapter 3) and/or floppy molecules (Chapter 4).

As a crucial ingredient for each method, we have to define the potential energy surface(s) (PESs) – the landscapes, defined by the electrons of the molecule, on which the nuclear wave function evolves. Traditionally, one aspires to determine these PESs *a priori*, which introduces a significant practical bottleneck for larger molecules. Generally,  $n^N$  evaluations of the PES are required assuming an equidistant grid, an  $N$ -dimensional system, and  $n$  grid points per dimension. Subsequent interpolation of the PES further increases the already formidable computational costs. However, because only local knowledge of the PES is required for trajectory-based methods and most parts of the PES are not explored at all during the dynamics, one can conveniently employ an on-the-fly (OTF) scheme. The PES is then computed only where needed and the exponential scaling with  $N$  is thus avoided.

The main goal of theoretical studies is to provide new insights into the underlying physical and chemical processes and not the mere reproduction of experimental results. In

---

contrast to an experimentalist, a theorist has access to a very large amount of information that is collected during the dynamics. The analysis of this host of information can be then understood, in a modern parlance, as a *data-mining* problem: How can we extract the essential information from the simulation data and how can we transform it into an understandable picture? This question is even more important when an OTF scheme is used, since then the PES is not explicitly available and the dynamics is the only source of information about the system under consideration. In this respect, we present a novel approach in Chapter 3 that allows decoding spectra calculated within the TGA. In Chapter 5 this framework is further studied within the limit of a harmonic model system.

## 1.2 Time-dependent picture of linear spectroscopy

In the time-dependent approach, pioneered by Heller,<sup>1</sup> the molecular spectrum is determined by the Fourier transform of an appropriate correlation function whose shape is modulated by the nuclear motion induced by the electronic excitation. While the time-dependent and time-independent approaches provide complementary pictures for linear spectroscopy, the former is the obvious natural choice for time-resolved spectra.

Here, we briefly illustrate the theoretical framework of linear spectroscopy formulated in the wave-packet language<sup>2-3</sup> using the example of electronic absorption. We follow closely the derivation presented in Ref. [4], in which, however, a more general treatment on the basis of density-operator formalism is used.

In the following, we consider the total Hamiltonian to be of the form  $\hat{H}_{\text{tot}}(t) = \hat{H}_{\text{mol}} + \hat{V}_{\text{int}}(t)$ , where  $\hat{H}_{\text{mol}}$  represents the time-independent molecular Hamiltonian and  $\hat{V}_{\text{int}}$  describes the interaction of the molecule with a classical electromagnetic field. Here, we are interested in electronic transitions in the range of visible or UV light. Therefore, we can invoke the *electric-dipole approximation*, which is valid if the characteristic wave length is much larger than the spatial extent of the molecule, i.e., the spatial part of the radiation field is approximated by  $e^{ik \cdot r} \approx 1$ . Further, assuming linearly polarized electric field  $\vec{E}(t) = \vec{\epsilon} E(t)$ , the interaction potential  $\hat{V}_{\text{int}}$  takes a simple form

$$\hat{V}_{\text{int}}(t) = -\hat{\mu} E(t), \quad (1.2)$$

where  $\hat{\mu}$  is the molecular electric dipole operator projected on the unit polarization vector  $\vec{\epsilon}$ , i.e.,

$$\hat{\mu} = \hat{\mu} \cdot \vec{\epsilon}. \quad (1.3)$$

---

The rate of change of the molecule's energy  $H_{\text{tot}}(t)$  in state  $|\psi(t)\rangle$  is easily evaluated as the time derivative of the expectation value of the total Hamiltonian

$$\frac{d}{dt}H_{\text{tot}}(t) = \frac{d}{dt}\langle\psi(t)|\hat{H}_{\text{tot}}(t)|\psi(t)\rangle = -P(t)\frac{d}{dt}E(t), \quad (1.4)$$

where we introduced the *polarization*

$$P(t) = \langle\psi(t)|\hat{\mu}|\psi(t)\rangle. \quad (1.5)$$

The total energy absorbed per unit frequency is then found by expressing the right hand side of Eq. (1.4) in the frequency domain. The unitarity of the Fourier transform and the Fourier-derivative relations readily yield

$$\Delta H(\omega) = -2\pi\omega \text{Im}\left[\tilde{P}(\omega)^* \tilde{E}(\omega)\right]. \quad (1.6)$$

The spectrum, or more precisely, the frequency-dependent cross section for the energy transfer from the field to the molecule is then given by

$$\sigma(\omega) = \frac{\Delta H(\omega)}{I_0(\omega)} = -\frac{4\pi\omega}{c} \frac{\text{Im}\left[\tilde{P}(\omega)^* \tilde{E}(\omega)\right]}{|\tilde{E}(\omega)|^2}, \quad (1.7)$$

where  $c$  denotes the speed of light in vacuum and the incident energy per area  $I_0(\omega) = \frac{1}{2}c|\tilde{E}(\omega)|^2$  is found by integrating the incident energy flux  $S(t) = c|\vec{E}(t) \times \vec{B}(t)|/4\pi = cE(t)^2/(4\pi)$  over all times.

It should be noted that the nonperturbative expression for the spectrum in Eq. (1.7) retains its validity independent of the strength and/or character of the field. Moreover, it is applicable to linear as well as nonlinear phenomena.

The time-dependent polarization of Eq. (1.5) constitutes the crucial, and in general computationally costly, ingredient for the evaluation of the spectrum in Eq. (1.7). For weak interactions, one can employ the time-dependent perturbation theory (TDPT) and expand the polarization  $P(t)$  in a perturbative manner. The first two leading terms are

$$P^{(0)}(t) = \langle\psi^{(0)}(t)|\hat{\mu}|\psi^{(0)}\rangle \quad (1.8)$$

$$P^{(1)}(t) = \langle\psi^{(0)}(t)|\hat{\mu}|\psi^{(1)}\rangle + \text{c.c.} \quad (1.9)$$



, where  $\psi^{(n)}$  denotes the  $n$ th term in the expansion of the wave function in a power series in  $\lambda$ , i.e.,  $\psi(t) = \sum_n \lambda^n \psi^{(n)}(t)$ . The even-order terms, notably  $P^{(0)}(t)$ , vanish in isotropic media when averaged over the orientation of the molecule (or, equivalently, over the orientation of the unit polarization vector  $\vec{\epsilon}$ ). Therefore, the first-order polarization  $P^{(1)}(t)$  is of primary interest. To demonstrate its evaluation on a particular example, we consider absorption in a two-level system where the levels are coupled exclusively via the electric field and only the ground state is initially populated, i.e.

$$\begin{aligned}\hat{H}_{\text{mol}} &= \begin{bmatrix} \hat{H}_g & 0 \\ 0 & \hat{H}_e \end{bmatrix}, \\ \hat{V}_{\text{int}} &= \begin{bmatrix} 0 & -\hat{\mu}_{ge} E(t) \\ -\hat{\mu}_{eg} E(t) & 0 \end{bmatrix}, \\ \psi(0) &= \begin{bmatrix} |\psi_g(0)\rangle \\ 0 \end{bmatrix}.\end{aligned}\tag{1.10}$$

Now, the chief contribution to the  $e \leftarrow g$  absorption process originates in the first term of the right-hand side of Eq. (1.9). In the setting of Eq. (1.10), we denote this term as  $P_{ge}^{(1)}(t)$ . Within TDPT we directly obtain

$$P_{ge}^{(1)}(t) = \frac{i}{\hbar} \int_0^\infty dt' E(t-t') C_\mu(t')\tag{1.11}$$

$$C_\mu(t) = \langle \psi_g(0) | e^{i\hat{H}_g t/\hbar} \hat{\mu}_{ge} e^{-i\hat{H}_e t/\hbar} \hat{\mu}_{eg} | \psi_g(0) \rangle,\tag{1.12}$$

where  $C_\mu(t)$  is the so-called *dipole time autocorrelation function*. To calculate the absorption spectrum via Eq. (1.7) we need to express  $P_{ge}^{(1)}(t)$  in the frequency domain. Thus, we first introduce the causal form of  $C_\mu(t)$ , namely

$$S_\mu(t) = \begin{cases} C_\mu(t) & t > 0 \\ 0 & t < 0 \end{cases},\tag{1.13}$$

since this permits to express  $P_{ge}^{(1)}(t)$  as a convolution, i.e.,  $P_{ge}^{(1)}(t) = \frac{1}{\hbar} (E * S_\mu)(t)$ . Fourier convolution theorem then immediately yields the desired spectral representation of the first-order polarization as

---


$$\tilde{P}_{ge}^{(1)}(\omega) = \frac{1}{2\pi} \int_{-\infty}^{\infty} P_{ge}^{(1)}(t) e^{i\omega t} dt = \frac{2\pi i}{\hbar} \tilde{E}(\omega) \tilde{S}_{\mu}(\omega). \quad (1.14)$$

The linear absorption spectrum, still assuming a fixed orientation of the molecule, is then given by combining Eqs. (1.14) and (1.7)

$$\sigma_{\text{abs}}(\omega) = \frac{8\pi^2 \omega}{\hbar c} \text{Re}[\tilde{S}_{\mu}(\omega)] = \frac{2\pi\omega}{\hbar c} \text{Re} \int_0^{\infty} C_{\mu}(t) e^{i\omega t} dt. \quad (1.15)$$

Note that the final expression for the absorption spectrum does not contain any explicit dependence on the field. Equation (1.15) is thus valid for pulsed as well as continuous-wave experiments. In isotropic media, an experimentally accessible spectrum  $\sigma_{\text{iso,abs}}$  is obtained by averaging  $\sigma_{\text{abs}}$  over all orientations of the molecule. However, this averaging produces merely a constant scaling factor, namely,  $\sigma_{\text{iso,abs}} = \frac{1}{3} \sigma_{\text{abs}}$ .

Further assuming that the transition dipole moment is coordinate independent, i.e.  $\hat{\mu} = \mu$ , which is known as the *Condon approximation*, the dipole time autocorrelation function [Eq. (1.12)] simplifies as

$$C_{\mu}(t) = |\mu|^2 f(t) \quad (1.16)$$

$$f(t) = \langle \psi(0) | e^{i\hat{H}_g t/\hbar} e^{-i\hat{H}_e t/\hbar} | \psi(0) \rangle, \quad (1.17)$$

where the correlation function  $f$  may be called ‘‘fidelity’’ amplitude (see Section 1.3.1). The well-known equation relating the spectrum to the Fourier transform of the autocorrelation function

$$C(t) = \langle \psi(0) | e^{-i\hat{H}_e t/\hbar} | \psi(0) \rangle \quad (1.18)$$

follows then from employing the low temperature limit, i.e.  $\hat{H}_g |\psi(0)\rangle = E_0 |\psi(0)\rangle$  :

$$\sigma_{\text{iso,abs}}(\omega) = A \omega \text{Re} \int_0^{\infty} C(t) e^{it(\omega+E_0/\hbar)} dt, \quad (1.19)$$

where  $A = |\mu|^2 2\pi/3\hbar c$  is a constant prefactor and  $E_0$  represents the energy of the vibrational ground state of the ground electronic state.

In summary, the TDPT picture significantly simplifies interpretation of the absorption spectrum by providing the connection with the Fourier transform of the corresponding autocorrelation function that is determined by nuclear motion on the excited electronic

---

surface. Analogously, the correlation function relevant for emission spectrum is computed by propagating ground vibrational state of the excited electronic state on the ground electronic surface. Finally, let us note that for calculations of nonlinear spectra, such as time-resolved stimulated emission spectra, the polarization  $P$  has to be expanded to third order.

### 1.3 Multi-trajectory semiclassical methods

The following section summarizes various semiclassical methods based on classical trajectories applicable for evaluation of the correlation function in Eq. (1.17) central to the previous section. While the dephasing representation detailed in Subsection 1.3.1 provides an approximation directly for the correlation function  $f(t)$  [Eq. (1.17)], the Herman-Kluk propagator and frozen Gaussians approximation (FGA) constitute “dynamical methods”, i.e., the two copies of the initial state in Eq. (1.17) are independently propagated with two different Hamiltonians, and the correlation function  $f(t)$  is then evaluated explicitly as an overlap of the evolving states.

Although the semiclassical Van Vleck propagator<sup>5</sup> had been known for decades, the numerical difficulties associated with its direct application amplified by the limited computational power at that time hindered its widespread use in practical calculations. In the now seminal paper by Herman and Kluk,<sup>6</sup> the authors proposed to formulate the propagator (HK propagator) in a “mixed representation” of coherent states. In this spirit, the evolving state is represented as a superposition of independent (uncoupled) Gaussians

$$\langle q | q^t, p^t \rangle = \left( \frac{\det \gamma}{\pi^D} \right)^{1/4} \exp \left[ -(q - q^t)^T \cdot \frac{\gamma}{2} \cdot (q - q^t) + \frac{i}{\hbar} (p^t)^T \cdot (q - q^t) \right] \quad (1.20)$$

the phase-space centers  $x^t = (q^t, p^t)$  of which are guided by classical trajectories and each Gaussian is moreover equipped with a phase and a complex prefactor.<sup>6-9</sup> Formally

$$|\psi(t)\rangle = \left( \frac{1}{2\pi\hbar} \right)^D \int dq^0 dp^0 C(q^0, p^0, t) e^{i S_{\text{cl}}(q^0, p^0, t)} |q^t, p^t\rangle \langle q^0, p^0 | \psi(0)\rangle, \quad (1.21)$$

where  $S_{\text{cl}}$  denotes the classical action and the prefactor  $C(q^0, p^0, t)$  reads

$$C(q^0, p^0, t) = \det \left[ \frac{1}{2} \left( M_{qq}^t + M_{pp}^t + \frac{\hbar\gamma}{i} M_{qp}^t + \frac{i}{\hbar\gamma} M_{pq}^t \right) \right]^{1/2} \quad (1.22)$$

---

Here,  $M = \partial x^t / \partial x^0$  is the stability matrix that indicates the “sensitivity” of a given trajectory with respect to the initial conditions.

The prefactor  $C(q^0, p^0, t)$  constitutes a significant computational bottleneck because its evaluation requires the stability matrix which in turn necessitates evaluation of the Hessians. Unfortunately, already relatively low-dimensional systems seem to require a rather high number of trajectories to achieve convergence.<sup>10-11</sup> To alleviate this difficulty, Tatchen et al.<sup>12</sup> proposed the “poor-person's HK propagator” within which the prefactor is assumed to be common for all Gaussians (trajectories), i.e., only one Hessian per step is required. Alternatively, one can also profit from the log-derivative formulation of the prefactor as suggested by Gelabert et al.<sup>13</sup> or various other techniques such as time averaging,<sup>14</sup> time slicing,<sup>15</sup> or smoothening of the integral over initial conditions in terms of (generalized) Filinov filter.<sup>16-17</sup>

The main prescription for the HK propagator [Eq. (1.21)] closely resembles the “Frozen Gaussians approximation”.<sup>18</sup> Within this approach, the evolving state is also represented as a superposition of independent Gaussians as in Eq. (1.20), however, there is no additional prefactor and the classical action is replaced with an “effective” action that is “non-local”. In general, it is necessary to calculate this ingredient approximately, e.g., by applying local harmonic approximation to the potential. Thus, it is tempting to invoke the HK propagator [Eq. (1.21)] ignoring the prefactor altogether. Although this “unit-prefactor” HK propagator<sup>12</sup> rapidly loses normalization per se, it was used successfully in *ab initio* setting to reproduce the absorption spectrum of formaldehyde.<sup>19</sup> However, around 6000 trajectories were required in this 6-dimensional on-the-fly calculation.

### 1.3.1 Dephasing representation of quantum fidelity

The dephasing representation<sup>20-22</sup> (DR), inspired by the semiclassical perturbation theory of Miller and coworkers,<sup>23-24</sup> is a semiclassical approximation for quantum fidelity  $F_{\text{QM}}$ , which has been introduced by Peres<sup>25</sup> to measure the sensitivity of quantum dynamics to perturbations. This quantity is defined as the time-dependent overlap of two copies of an initial state propagated with an unperturbed Hamiltonian  $\hat{H}_1$  and a perturbed Hamiltonian  $\hat{H}_2$ :

$$F_{\text{QM}} = \left| \langle \psi(0) | e^{i\hat{H}_2 t/\hbar} e^{-i\hat{H}_1 t/\hbar} | \psi(0) \rangle \right|^2 = |f(t)|^2. \quad (1.23)$$

---

We see directly that  $F_{\text{QM}}$  can be interpreted as the square of the time-correlation function [Eq. (1.17)] employed in electronic spectroscopy. We can then approximate this time-correlation function by the DR amplitude  $f_{\text{DR}}$ , which is expressed as an interference integral over “dephasing trajectories” with initial conditions  $x^0 = (q^0, p^0)$  and weighted by the Wigner function  $\rho_W$  of the initial state

$$f_{\text{DR}}(t) = \int dx^0 \rho_W(x^0) e^{-i\Delta S(x^0, t)/\hbar}$$

$$\rho_W(x^0) = h^{-D} \int ds \psi^* \left( q + \frac{s}{2} \right) \psi \left( q - \frac{s}{2} \right) \exp \left( i \frac{qp}{\hbar} \right). \quad (1.24)$$

The phase is given by the time integral  $\Delta S(x^0, t) = -\int_0^t \Delta V[q^{t'}(x^0)] dt'$  of the potential difference along the trajectory with initial condition  $x^0$  propagating on the average potential  $\Delta V = (V_1 + V_2)/2$ .

In electronic spectroscopy, closely related approximations like Mukamel’s phase averaging,<sup>26-27</sup> Wigner-averaged classical limit, or linearized semiclassical initial value representation<sup>28-29</sup> have been used by several authors.<sup>28-34</sup> DR also has many other applications—it provides a measure of the accuracy of quantum molecular dynamics on an approximate potential energy surface<sup>35-36</sup> or describes the transition from the Fermi-Golden-Rule to the Lyapunov regime of fidelity decay in the field of quantum chaos.<sup>37-40</sup> Its generalization to multiple surfaces is important in the study of nonadiabatic effects: It has been used to measure the dynamical importance of diabatic,<sup>41</sup> nonadiabatic,<sup>42</sup> or spin-orbit couplings.<sup>43</sup> Furthermore, by using multiple-surface DR, non-adiabatic effects have been included into absorption and time-resolved stimulated emission spectra computations of pyrazine.<sup>4</sup>

Mollica and Vanicek<sup>44</sup> have shown analytically that the number of trajectories required for convergence of Eq. (1.24) is independent of the system’s dimensionality, Hamiltonian, or total evolution time. Furthermore, the computational efficiency of the DR can be further increased in the spirit of Heller’s *cellularization*,<sup>45</sup> in which the contribution of neighboring trajectories is considered analytically.<sup>46-48</sup>

Here, we want to briefly describe the drawbacks of DR for computing electronic spectra of isolated molecules. Consider two electronic potentials each described by a harmonic model. It has been shown that DR is exact in displaced harmonic oscillators.<sup>26-27</sup> However, if these harmonic potentials are not displaced, but their force constants are different, the DR breaks down. This situation is common in molecular systems because only a few DOFs are strongly affected, e.g. displaced, by a (de)excitation. The remaining

DOFs are “silent”, and their frequencies are only slightly perturbed. But these silent DOFs introduce decay in DR, and therefore, the information about the interesting DOFs is covered.

Figure 1 demonstrates this effect:  $C_{\text{DR}}(t)$  decays when one DOF with perturbed frequency is added, whereas the corresponding  $C_{\text{QM}}(t)$  oscillates closely to 1. This decay introduces an artificial broadening in the spectrum. Therefore, the bigger the molecule, the faster DR decays and the broader is the spectrum. Hence, DR is not well-suited for linear spectroscopy, e.g. absorption and emission, because one is often interested in vibrationally resolved spectra. In the case of time-resolved electronic spectra, the energy resolution is less important than its time-dependence, which is well reproduced by DR.

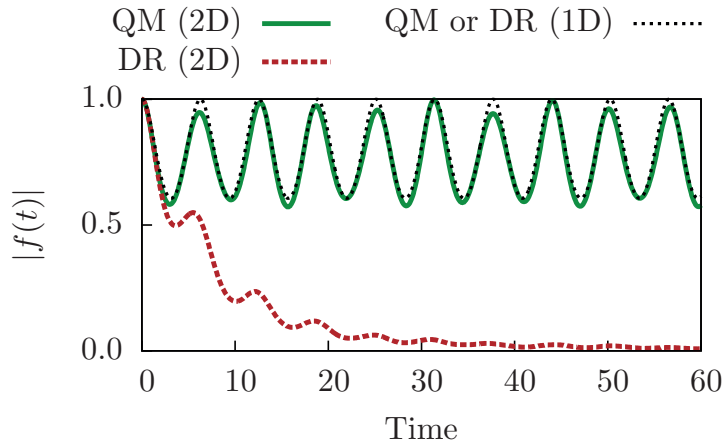


Figure 1: Influence of perturbing the harmonic force constant on the correlation function computed with dephasing representation (DR) [Eq. (1.24)]. In the one-dimensional harmonic model (1D), ground state  $g$  and the excited state  $e$  are displaced ( $d = 0.5$ ). Both states have the same harmonic force constant  $k_g = k_e = 1$ . For the two-dimensional model (2D), a further dimension is added that is characterized by a change in the force constants between the states, i.e.,  $k_g = 1$ ,  $k_e = 0.5$ , and by no displacement  $d = 0$ . This new degree of freedom affects strongly the DR result, whereas the exact quantum (QM) correlation function is only slightly perturbed.

Zambrano and Ozorio de Almeida<sup>49</sup> proposed a prefactor that qualitatively corrects—at least in some cases—the artificial decay of DR. However, the cost per trajectory as well as the required number of trajectories increase significantly.<sup>46</sup>

#### 1.4 Thawed Gaussian approximation

Another possibility to compute vibronic spectra for large molecules is to use semiclassical methods based on one trajectory like the celebrated *thawed Gaussian approxima-*

---

tion<sup>50-51</sup> (TGA) of Heller. TGA belongs among the earliest practical semiclassical approaches to quantum dynamics. The main idea is exceedingly simple—since a Gaussian wave packet (GWP) evolving in a globally harmonic potential retains its functional form, one expects that propagating a single thawed GWP using a local harmonic approximation for the potential can provide a reasonable approximation in many applications. This is especially true when the dynamics of interest have ultrafast character.

Within TGA, the evolving GWP is assumed to take the form of

$$\psi^t(q) = N^0 \exp \left\{ -(q - q^t)^T \cdot A^t \cdot (q - q^t) + \frac{i}{\hbar} \left[ (p^t)^T \cdot (q - q^t) + \gamma^t \right] \right\}, \quad (1.25)$$

where  $N^0$  is a normalization constant,  $x^t = (q^t, p^t)$  denotes the GWP's phase-space center,  $A^t$  is a complex, symmetric width matrix, and  $\gamma^t$  represents an overall phase factor. Note that  $\gamma^t$  is a time-dependent complex number. Its imaginary part guarantees normalization of  $\psi^t(q)$  for  $t \geq 0$ . The key ingredient of the method consists in expressing the potential  $V(q)$  in the *local harmonic approximation* (LHA). This in turn yields a time-dependent effective potential

$$V_{\text{eff}}^t(q) = V|_{q^t} + \left( \text{grad}_q V|_{q^t} \right)^T \cdot (q - q^t) + \frac{1}{2} (q - q^t)^T \cdot \text{Hess}_q V|_{q^t} \cdot (q - q^t). \quad (1.26)$$

Here, the potential  $V|_{q^t}$ , gradient  $\text{grad}_q V|_{q^t}$ , and Hessian  $\text{Hess}_q V|_{q^t}$  are evaluated at the current coordinate center  $q^t$  of the evolving GWP at time  $t$ . As already alluded to above, the second-order Taylor expansion (1.26) ensures that the ansatz (1.25) is plausible even for  $t > 0$ . Denoting by

$$H_{\text{eff}}^t := p^T \cdot (G^{-1} / 2) \cdot p + V_{\text{eff}}^t \quad (1.27)$$

the effective Hamiltonian and inserting the ansatz (1.25) into the TDSE

$$i\hbar \frac{\partial}{\partial t} \psi^t(q) = H_{\text{eff}}^t \psi^t(q), \quad (1.28)$$

gives equations of motion for  $x^t$ ,  $A^t$ , and  $\gamma^t$ :

$$\dot{x}^t = \{x, H_{\text{eff}}^t\}, \quad (1.29)$$

$$\dot{A}^t = -2i\hbar A^t \cdot G^{-1} \cdot A^t + \frac{i}{2\hbar} \nabla^2 V(q^t), \quad (1.30)$$

---


$$\dot{\gamma}^t = \mathcal{L}_{\text{eff}}^t - \hbar^2 \text{Tr}[G^{-1} \cdot A^t], \quad (1.31)$$

where  $G$  is the mass matrix and  $\mathcal{L}_{\text{eff}}^t$  denotes Lagrangian dual to  $H_{\text{eff}}^t$ . Numerical integration of the classical equations of motion (1.29) is easily carried out in a symplectic fashion. In order to integrate Eq. (1.30), Lee and Heller<sup>51</sup> proposed to factorize matrix  $A^t$  by two auxiliary matrices  $P^t$  and  $Z^t$  as

$$A^t = -\frac{i}{2\hbar} P^t \cdot (Z^t)^{-1}. \quad (1.32)$$

Since this decomposition is clearly not unique, a further constraint is imposed, namely

$$\dot{Z}^t = G^{-1} \cdot P^t. \quad (1.33)$$

In matrix notation, the unique solution of Eqs. (1.32) and (1.33) can be written as

$$\begin{pmatrix} Z^t \\ P^t \end{pmatrix} = M^t \cdot \begin{pmatrix} Z^0 \\ P^0 \end{pmatrix}, \quad (1.34)$$

with initial conditions  $Z^0 = I$  and  $P^0 = 2i\hbar A^0$ . The time-dependent matrix  $M^t := \partial x^t / \partial x^0$  is the stability matrix corresponding to the evolving phase-space point  $x^t$ . Finally, by inserting Eqs. (1.32) and (1.34) into Eq. (1.31) and by employing the matrix identity  $\det(\exp B) = \exp(\text{Tr} B)$ , one directly obtains an explicit solution for  $\gamma^t$  in the form

$$\gamma^t = \int_0^t \mathcal{L}_{\text{eff}}^\tau d\tau + \frac{i\hbar}{2} \ln(\det Z^t). \quad (1.35)$$

The real part of the complex number  $\gamma^t$  represents an overall phase factor while its imaginary part guarantees normalization of  $\psi^t(q)$  for  $t \geq 0$ . Note that since the matrix  $Z^t$  is complex, one has to ensure that a proper branch of the logarithm be taken to make  $\gamma^t$  continuous in time.

If the potential happens to be globally quadratic, the effective potential of Eq. (1.26) ceases to be time-dependent because the particular point with respect to which one constructs the Taylor expansion is irrelevant. Also, the classical phase-space trajectory  $x^t$  and the stability matrix  $M^t$  are in this case easily accessible analytically.

Although the accuracy of the single GWP description is clearly limited and its error increases in time, effects of anharmonic or double-well potentials are, at least, partially captured by TGA. More importantly, TGA can treat all vibrational degrees of freedom



---

on an equal footing even in a large system due to its moderate computational cost. Furthermore, the single GWP dynamics provides a tractable picture and interpretation of rather complicated physical processes such as absorption, emission and Raman spectroscopy.<sup>1, 51-55</sup>

## 1.5 On-the-fly scheme

Traditional quantum dynamics requires an *a priori* determination of the PESs. As mentioned above, this constitutes a computational bottleneck especially for larger systems unless the PESs can be described, e.g., by global harmonic approximation. For trajectory-based methods such as classical molecular dynamics, semiclassical dynamics, or methods employing Gaussian basis sets, an alternative strategy is to use an on-the-fly (OTF) scheme.

Within OTF, also known as *direct*, scheme,<sup>56-57</sup> the PESs are evaluated only where needed by solving the electronic Schrödinger equation at the relevant nuclear geometry using *ab initio* (AI) electronic-structure methods. Employing the Born-Oppenheimer approximation, the time-dependent Schrödinger equation for the nuclear wave packet reads

$$i\hbar \frac{\partial \psi(t, R)}{\partial t} = [\hat{T} + V(R)] \psi(t, R), \quad (1.36)$$

where  $\hat{T}$  is the nuclear kinetic energy operator and  $R$  denotes a particular geometry of the nuclei. The effective potential energy  $V(R)$  for given  $R$  is obtained by solving the electronic time-independent Schrödinger equation

$$\hat{H}_{\text{el}}(r; R) \psi_{\text{el}}(r; R) = V(R) \psi_{\text{el}}(r; R), \quad (1.37)$$

where  $\hat{H}_{\text{el}}$  denotes the electronic Hamiltonian describing electron-electron, electron-nuclear, and nuclear-nuclear interactions as well as the electronic kinetic energy. Note that the electronic wave function  $\psi_{\text{el}}$  depends on the nuclear geometry  $R$  only parametrically. Within the Born-Oppenheimer approximation, the couplings between the electronic states corresponding to different solutions in Eq. (1.37) are neglected, and therefore the nuclear motion follows a specific electronic state. These couplings would give rise to non-adiabatic effects that are beyond the scope of this work.

Equation (1.37) is solved approximately during the nuclear dynamics by standard software packages tailored for electronic-structure calculations. For a given nuclear geome-

---

try  $R$ , these packages typically provide the energy, the gradient, and, if required, even the more expensive Hessian.

OTF-AI simulations are conceptually simple, but the “art” consists in the design of the *ab initio* setup. This controls the accuracy to which Eq. (1.37) is solved as well as the overall computational costs. Whereas highly accurate electronic structure methods combined with large basis sets are affordable for smaller molecules and/or methods based on a few trajectories, one is forced to seek an optimal balance between accuracy and computational efficiency for larger molecules. This is especially true when excited state calculations are involved for which less efficient electronic structure methods are available. Here, the *ab initio* level of theory has to be chosen with great care.

In an OTF-AI dynamics, the required potential information is provided in Cartesian coordinates  $\xi$  at each propagation step by an electronic-structure package. In contrast to classical trajectory propagation, which necessitates only evaluation of the force, TGA (among other semiclassical methods) requires repeated evaluation of the Hessian along the evolving trajectory because the Hessian is needed for propagation of the stability matrix  $M^t$ .

### 1.5.1 On-the-fly *ab initio* thawed Gaussian wave packet dynamics

In the case of OTF-AI-TGA, the evolving GWP is properly defined only in the subspace of the vibrational degrees of freedom of the molecule of interest. Therefore, a germane choice of the coordinate system is essential. We illustrate the procedure employed in the numerical calculations done in Chapter 3 and in Chapter 4 on a specific scenario of two PESs—ground and excited. The initial GWP corresponding to the ground vibrational state of the ground PES is subsequently propagated on the excited PES. We published this framework in Ref. [58].

Let us consider a reference equilibrium geometry  $\xi_{\text{ref}}$  on the ground PES where  $\xi_{\text{ref}}$  is a Cartesian  $3N$ -vector with  $N$  denoting the number of atoms in the molecule. Any displaced molecular configuration  $\xi$  obtained, e.g. by propagation on a different PES, can be related to the normal-mode coordinates  $\eta$  as

$$\xi - \xi_{\text{ref}} = G^{-\frac{1}{2}} \cdot O \cdot \eta = T \cdot \eta, \quad (1.38)$$

with  $T := G^{-\frac{1}{2}} \cdot O$  and  $O$  denoting the orthogonal matrix that diagonalizes the mass-scaled Cartesian Hessian matrix evaluated at  $\xi_{\text{ref}}$ , i.e.,  $T^T \cdot \text{Hess}_{\xi} V|_{\xi_{\text{ref}}} \cdot T = \Omega^2$ . Here,

---

$\Omega = \text{diag}(\omega_1, \dots, \omega_{3N})$  is the diagonal matrix containing the normal-mode frequencies. Note that  $\eta$  in Eq. (1.38) has  $3N$  components, i.e., also incorporates the 3 translational and 3 rotational degrees of freedom. However, the initial values of these displacements are zero and one would also like to preserve this constraint during the dynamics on the excited PES. The translational modes are easily projected out by shifting the center of mass to the origin of the Cartesian frame of reference. Next, to minimize the coupling to the remaining 3 rotational modes, we closely follow the axis-switching procedure devised by Hougen and Watson.<sup>59-60</sup> In this spirit, any displaced configuration  $\xi$  is rotated relatively to  $\xi_{\text{ref}}$  in order to satisfy Eckart's conditions:

$$\sum_{a=1}^N m_a (\mathbf{P}_a \cdot \xi_{\text{ref}}) \times \mathbf{P}_a \cdot (\Lambda \cdot \xi) = 0. \quad (1.39)$$

In Eq. (1.39), the sum runs over all  $N$  atoms,  $\Lambda$  is a  $3N \times 3N$  block-diagonal matrix, where each of the  $N$  blocks is a copy of a 3-dimensional rotation matrix  $R$ , and the  $3 \times 3N$  matrix  $\mathbf{P}_a$  is defined as  $(\mathbf{P}_a)_{i,j} = \delta_{i,1} \delta_{j,3a-2} + \delta_{i,2} \delta_{j,3a-1} + \delta_{i,3} \delta_{j,3a}$ . Application of  $\mathbf{P}_a$  to a configuration  $\xi$  essentially selects coordinates of the  $a$ th atom. Having minimized the coupling to the rotational modes, one can afford to consider in Eq. (1.38) only the first  $(3N - 6)$  columns of the matrix  $O$ . In that case, the transformation matrix  $T$  also reduces to a  $3N \times (3N - 6)$  form. Kudin and Dymarsky showed<sup>61</sup> that the rotation matrix  $R$  solving Eq. (1.39) can be obtained by minimizing the mass-weighted root-mean-square distance of  $\xi$  with respect to the reference configuration  $\xi_{\text{ref}}$ . In practice, this is efficiently achieved by employing direct methods based on singular value decomposition or quaternion formalism.<sup>62-63</sup>

The transformation from the Cartesian to the vibrational normal-mode coordinates is thus performed in three consecutive steps. First, the configuration  $\xi$  is shifted to the center-of-mass system. Second, it is rotated to the Eckart frame, and finally it is projected onto the vibrational normal modes, i.e.,

$$\eta = W \cdot [\Lambda \cdot (\xi - \Delta) - \xi_{\text{ref}}], \quad (1.40)$$

where  $W := T^T \cdot G$  and the center-of-mass vector  $\Delta$  is defined as

$$\Delta := \left( \sum_{a=1}^N \mathbf{P}_a \right)^T \cdot \sum_{a=1}^N m_a \mathbf{P}_a \cdot \xi / \sum_{a=1}^N m_a. \quad (1.41)$$

Finally, one also needs to express the Cartesian gradient  $\text{grad}_\xi V$  and the Cartesian Hessian matrix  $\text{Hess}_\xi V$  in the  $\eta$ -coordinates:

---


$$\text{grad}_\eta V = \text{grad}_\xi V \cdot (W \cdot \Lambda)^T, \quad (1.42)$$

$$\text{Hess}_\eta V = (W \cdot \Lambda) \cdot \text{Hess}_\xi V \cdot (W \cdot \Lambda)^T. \quad (1.43)$$

Every step in an OTF-AI-TGA calculation is well defined—there is no “free parameter” to be set up. First, an optimization followed by a frequency computation are performed on the initial electronic surface using an *ab initio* electronic structure package to determine the initial wave packet and the normal mode coordinates. Second, the geometries, gradients, and Hessians along the trajectory propagated on the final electronic state are evaluated in Cartesian coordinates by an *ab initio* electronic structure package and then transformed to normal mode coordinates using Eqs. (1.40), (1.42), and (1.43).

In practice, the *ab initio* results evaluated along the trajectory are stored for two reasons: First, the OTF-AI-TGA calculations can be further accelerated by using an interpolation scheme for the expensive Hessians (see Subsection 3.3.2). Second, the analysis of the GWP dynamics using the approach introduced in Subsection 3.3.3 requires reevaluations of the dynamics on different subspaces.

The main idea for constructing the OTF-AI-TGA framework was to compute electronic spectra of molecular systems that are not accessible by traditional semiclassical methods. In Chapter 3 we show via the emission spectra calculation of oligothiophenes, that OTF-AI-TGA is efficient enough for molecules up to 37 atoms. We also test a common situation among floppy molecules. The excitation from an electronic state with a single minimum on a final electronic state features double minima along non-totally symmetric modes. The excited (totally symmetric) DOFs are, however, rather harmonic in the case of oligothiophenes. Therefore, the performance of OTF-AI-TGA in the case of large amplitude motions is addressed in Chapter 4. In addition, the limit of OTF-AI-TGA for describing higher-resolved spectra where long time dynamics is required is probed in Subsection 4.5.2.

#### 1.5.1.1 Computational protocol

Even though OTF-AI-TGA is an efficient semiclassical method, the associated *ab initio* computations can still pose significant bottleneck, especially for larger molecules. One is thus forced to optimize the computational protocol within the limits of the available computational resources. Therefore, we usually first propagate the classical *ab initio* trajectory since this requires only the evaluation of the gradient. This step is performed using our in-house code ‘Dynamics’ that provides an interface to quantum chemistry codes in terms of a collection of Perl scripts. In the next step, the expensive *ab initio*

---

Hessian evaluations are dealt with in a parallel fashion in order to fully profit from the available HPC infrastructure. The CPU time per step for various on-the-fly calculations can be found in Table 1.

Finally, the ab initio data (in Cartesian coordinates) are assembled into a single database. The TGA dynamics (Section 1.4) and the required Cartesian to normal-mode coordinate transformation [Eqs. (1.40), (1.42), and (1.43)] are then performed by reading the constructed database using a code written in Wolfram Mathematica.<sup>64</sup> Mathematica provides many powerful functions for computation and visualization that are especially useful for analyzing spectra computed with OTF-AI-TGA (Subsection 3.3.3).

Table 1: CPU time in second for gradient or Hessian evaluations performed with Gaussian09 package<sup>65</sup> for different OTF-AI-TGA calculations presented in this thesis. These calculations were done on an AMD Opteron 2427 CPU running at 2.2 GHz.

Molecule	<i>Ab initio</i> setup	Gradient CPU time [sec.]	Hessian CPU time [sec.]
Dithiophene (Chapter 3)	CAM-B3LYP/6-31+G(d,p)	50	430
Pentathiophene (Chapter 3)	CAM-B3LYP/6-31+G(d,p)	460	6900
NH <sub>3</sub> <sup>+</sup> (Chapter 4)	MP2/ aug-cc-pVTZ	100	1520
NH <sub>3</sub> <sup>+</sup> (Chapter 4)	CCSD/ aug-cc-pVTZ	3180	172920



---

## Chapter 2 Accelerating calculations of ultrafast time-resolved electronic spectra with efficient quantum dynamics methods

The motivation for this work was twofold: First, speeding up the full quantum calculation and, second, to use it as a reference for various semiclassical approximations. The semiclassical methods have been implemented by M. Šulc, whereas I extended our in-house code with new split-operator methods needed for accurate quantum calculations. The two-dimensional model potentials for the ground and excited electronic states of a collinear NCO molecule were small enough to converge all semiclassical approximations, but not too trivial to preclude reliable conclusions. The content of this chapter has been published in the *CHIMIA* issue dedicated to NCCR-MUST: “A New Swiss Research Priority in Molecular Ultrafast Science and Technology”.<sup>11</sup>

### 2.1 Abstract

We explore three specific approaches for speeding up the calculation of quantum time correlation functions needed for time-resolved electronic spectra: The first relies on finding a minimum set of sufficiently accurate electronic surfaces. The second approach increases the time step required for convergence of exact simulations by using different split-step algorithms to solve the time-dependent Schrödinger equation. The third approach lowers the number of trajectories needed for convergence of approximate semiclassical dynamics methods.

---

## 2.2 Introduction

Typical chemical reactions occur on the femtosecond (fs) time scale. In order to understand the reaction process in detail, one needs to observe it with a femtosecond time resolution. Once a femtosecond time-resolved spectrum is obtained, however, it is often nontrivial to translate the spectrum into a picture of the quantum dynamics (QD) occurring during the reaction. For a theorist, on the other hand, the dynamical picture is frequently the starting point. While the time-dependent picture is extremely useful even for understanding continuous wave spectra,<sup>1</sup> for time-resolved spectra it is obviously a natural choice. Instead of inferring the dynamics of the system from the measured spectra, the theorist does exactly the opposite: he or she computes the QD first and converts it to a time-resolved spectrum later. The main problem is the calculation of a certain time-correlation function; the spectrum is then obtained easily by a Fourier transform. E.g., for the pump-probe stimulated emission spectrum, within the electric dipole approximation, time-dependent perturbation theory, and for ultra short pulse length, the correlation function of interest is

$$C_{\text{st.em.}}(t, \tau) = E_{\text{pu}}^2 E_{\text{pr}} \text{Tr}[\rho_0(T) \mu_{01} U_1(-t - \tau) \mu_{10} U_0(t) \mu_{01} U_1(\tau) \mu_{10}], \quad (2.1)$$

$$U_j(t) = \exp(-iH_j t / \hbar).$$

Here  $E_{\text{pu}}$  and  $E_{\text{pr}}$  are the amplitudes of the pump and probe pulses,  $\rho_0(T)$  is the nuclear density operator in the electronic ground state at temperature  $T$ ,  $U_j$  is the quantum (QM) evolution operator for the nuclei on the  $j^{\text{th}}$  surface,  $\mu_{ij}$  is the dipole moment between states  $i$  and  $j$ ,  $\tau$  is the time delay between the pump and probe pulses, and  $t$  is time after the probe pulse. In order to focus on (and enhance) the QD nature of the problem, let us assume  $T = 0$ . Adopting the Franck-Condon approximation, the correlation function (2.1) becomes  $C(t, \tau) = (E_{\text{pu}})^2 E_{\text{pr}} |\mu_{10}|^4 f(t, \tau)$  where the so-called ‘‘fidelity’’ amplitude is

$$f_{\text{st.em.}}(t, \tau) = \langle \psi_0 | U_1(-\tau) U_1(-t) U_0(t) U_1(\tau) | \psi_0 \rangle \quad (2.2)$$

and  $\psi_0$  is the vibrational ground state on the ground electronic surface. The time-resolved stimulated emission spectrum is given by the Fourier transform

$$\sigma_{\text{st.em.}}(\omega, \tau) \propto \int_{-\infty}^{\infty} f_{\text{st.em.}}(t, \tau) e^{i\omega t} dt. \quad (2.3)$$

Below, we will not consider the contribution to the pump-probe spectrum from the ground-state absorption (or ‘‘bleach’’), which can be computed from Eq. (2.2) by exchanging the roles of ground and excited surfaces during the dynamics. While playing



---

a role in the pump-dump-pump-probe experiment we shall analyze below, the bleach is independent of the delay time for the strict pump-probe experiment, in which the initial state is stationary, and hence can be subtracted from the time-resolved spectrum. Note that a general pulse shape, nonperturbative effects, and non-Franck-Condon transitions can be included similarly as nonadiabatic couplings discussed below. The finite temperature effects can be treated via averaging with a QM Boltzmann factor, using, e.g., path integral Monte Carlo or path integral molecular dynamics methods that are used in our group for computing thermal rate constants and isotope effects.<sup>66-68</sup> The hardest part, however, remains, namely the calculation of the time-dependent state of the system, i.e., solving the time-dependent Schrödinger equation (TDSE),

$$i\hbar \frac{d}{dt} |\psi(t)\rangle = \hat{H} |\psi(t)\rangle, \quad (2.4)$$

or, more generally, the Liouville-von Neumann equation for the density operator.

There are two general ways to solve the TDSE. One can either solve it numerically exactly, which unfortunately scales exponentially with the number ( $D$ ) of QM degrees of freedom, or use an approximation that scales favorably with  $D$  and hope that the approximation is good enough for the given system. In both cases, the calculations are usually much more expensive than, e.g., molecular dynamics, and so one has to compromise between the accuracy of the method and its efficiency.

In this chapter, we will explore three specific approaches for speeding up the calculation of time correlation functions needed for time-resolved electronic spectra: The first relies on a choice of a minimum set of sufficiently accurate electronic surfaces. The second approach increases the required time step in exact simulations by using different split-step algorithms to solve the TDSE. The third approach lowers the number of trajectories needed for convergence of approximate semiclassical (SC) dynamics methods.

### 2.3 Finding a minimum set of sufficiently accurate electronic surfaces

Before starting a QD calculation, one has to decide how many coupled electronic potential energy surfaces (PESs) to include in the calculation and choose an appropriate method to compute these surfaces as well as nonadiabatic or spin-orbit couplings between them. Ability to find a minimum number of sufficiently accurate surfaces is the first important contribution to the efficiency of a QD simulation.

The calculation of PESs can be done either beforehand or “on the fly”, i.e., simultaneously with the QD. The surfaces and couplings must be accurate enough, yet not too

---

expensive since the QD itself is very expensive. However, it is very difficult to predict the effect of the accuracy of a PES on the QD without performing the QD itself. Mollica and Vanicek have found an efficient SC method that can do exactly this.<sup>35</sup> The accuracy at time  $t$  is defined as the QM fidelity  $F(t) = |f(t)|^2$ , i.e., the squared fidelity amplitude or the overlap of the time-dependent wave functions propagated on the accurate (but expensive) and approximate (yet cheap) surfaces. The fidelity is evaluated with a SC approximation, called dephasing representation<sup>21-22</sup> (DR) which only requires running classical dynamics on the approximate surface (and some potential, but not force evaluations on the accurate surface).

Knowing how to balance accuracy and efficiency for a given PES, one must further decide how many coupled PESs to include in the calculation. Including additional PESs makes the calculation more accurate but also much more expensive. Moreover, the importance of additional surfaces depends on the dynamics (in particular, on the initial condition): so in principle, one would have to perform the QD on many coupled surfaces to determine which surfaces are needed for the dynamics. It turns out that there is a simple way to estimate the dynamical importance of nonadiabatic (or spin-orbit or diabatic) couplings between PESs, using the DR of QM fidelity.<sup>41</sup> E.g., the significance of nonadiabatic couplings is measured by “nonadiabaticity,” i.e., fidelity defined as the overlap between the wave functions propagated using the uncoupled Born-Oppenheimer Hamiltonian and the fully coupled Hamiltonian.

## 2.4 Accelerating quantum dynamics with high order split operator methods

Once the choice of PESs has been made, the numerically exact QD can be performed on either a fixed or moving grid. The moving grid approaches, such as the multi-configuration time-dependent Hartree method (MCTDH),<sup>69</sup> allow treating a higher number of degrees of freedom, but it is more difficult to estimate rigorously their errors.<sup>70</sup> Here we focus on fixed-grid methods.

If the QM state  $|\psi(t)\rangle$  at time  $t$  is known, the state at time  $t + \Delta t$  is computed as

$$|\psi(t + \Delta t)\rangle = e^{-iH\Delta t/\hbar} |\psi(t)\rangle. \quad (2.4)$$

One way to increase the time step  $\Delta t$  in a simulation without sacrificing the accuracy is to realize that the TDSE (2.4) is not *any* differential equation, but a very specific one with many nice properties, such as time-reversibility, unitarity (the norm of the wave

---

function is preserved under time-evolution), and symplecticity (a somewhat technical generalization of unitarity).<sup>70</sup> A method that preserves these properties is more likely to remain accurate with a longer time step  $\Delta t$ . Among such methods are the so-called split operator methods<sup>71-77</sup>

$$e^{-i\Delta t H/\hbar} = \prod_{j=1}^n e^{-ia_j \Delta t V/\hbar} e^{-ib_j \Delta t T/\hbar} + O(\Delta t^{m+1}), \quad (2.5)$$

where  $V$  is the potential energy,  $T$  is the kinetic energy, and  $m$  is the order of the method. For real  $a_j, b_j$ , all such methods are automatically symplectic and unitary since both the kinetic and potential propagations themselves are. If the splitting (2.5) is also symmetric, then the method is time-reversible. Below we implement and compare several such methods.

The simplest method, a discrete-time implementation of the Lie-Trotter formula,<sup>78</sup> is the *first order split operator* (SO1) algorithm ( $n = 1, a_1 = 1, b_1 = 1$ ), which is however not time-reversible. The algorithm works as follows:

- i) wave function in position representation is Fourier-transformed to momentum representation in which  $T$  is diagonal [with the cost  $O(n \log n)$ , where  $n$  is the dimension of the Hilbert space representing the state],
- ii) kinetic propagation is trivially done by multiplication [with a cost  $O(n)$ ],
- iii) momentum wave function is inverse-Fourier-transformed back to the position representation in which the potential is diagonal [cost  $O(n \log n)$ ],
- iv) potential propagation is done by multiplication [cost  $O(n)$ ].

For this as well as other algorithms, the most expensive part is the Fast Fourier Transform (FFT), and so the cost of an algorithm for a given  $\Delta t$  is estimated by the number of FFTs. The SO1 algorithm requires two FFT operations ( $f = 2$ ) and it is of first order in  $\Delta t$  ( $m = 1$ ).

An improved algorithm is the *second order split operator* (SO2) algorithm<sup>71</sup> ( $n = 2, a_1 = a_2 = 1/2, b_1 = 1, b_2 = 0, f = 2, m = 2$ ), which requires also only two FFTs, but is accurate to second order in  $\Delta t$ . It is possible to design algorithms of any order, but they become increasingly complicated and beyond fourth order are rarely used. Hence we consider three types of fourth order split-operator algorithms that differ significantly in their design. The most straightforward one is an algorithm with all *real coefficients* [SO4-R,  $n = 4, a_1 = a_4 = \alpha/2, a_2 = a_3 = \alpha(1 - 2^{1/3})/2, b_1 = b_3 = \alpha, b_2 = -2^{1/3}\alpha, b_4 = 0$  where  $\alpha = (2 -$

$2^{1/3})^{-1}, f=6, m=4]$ .<sup>72-73, 77</sup> While this is an optimal fourth order algorithm (i.e., an algorithm minimizing  $f$ ) with all real coefficients, one can lower the number of the FFT operations by either considering complex coefficients or by allowing commutators of  $T$  and  $V$  in the splitting defined by Eq. (2.5).

The former approach starts with a 3<sup>rd</sup> order algorithm with *complex coefficients* SO3-C,  $n=3, a_1 = a_3^* = \beta/4, a_2 = 1/2, b_1 = b_2^* = \beta/2$  where  $\beta = 1 + 3^{-1/2} i, f=4, m=4]$ ,<sup>75-76</sup> which unfortunately is not strictly unitary. The order is increased by concatenating the SO3-C algorithm for odd steps with its conjugate algorithm SO3-C\* for even time steps, resulting in the 4<sup>th</sup> order algorithm SO4-C. The error is measured by the norm of the difference of the approximate and exact wave functions. [If the error is only measured by the (less stringent) overlap of the two wave functions, the 4<sup>th</sup> order can be reached simply by renormalizing the wave function after each step of the SO3-C algorithm.<sup>76</sup>

The latter approach generalizes the splitting by permitting the exponential of the commutator

$$[V, [T, V]] = \sum_i \frac{\hbar^2}{m_i} (\nabla_i V)^2 \quad (2.6)$$

in the splitting (6). An optimal resulting algorithm, requiring only four FFTs, is an algorithm with the *gradients* of  $V$  (SO4-G,  $n=3, f=4, m=4$ ),<sup>74, 79</sup>

$$e^{-i\Delta H/\hbar} = e^{-i\frac{1}{6}\Delta V/\hbar} e^{-i\frac{1}{2}\Delta T/\hbar} e^{-i\frac{2}{3}\Delta V_{\text{eff}}/\hbar} e^{-i\frac{1}{2}\Delta T/\hbar} e^{-i\frac{1}{6}\Delta V/\hbar} + O(\Delta t^5), \quad (2.7)$$

$$V_{\text{eff}} = V - \frac{1}{48} \left( \frac{\Delta t}{\hbar} \right)^2 [V, [T, V]].$$

## 2.5 Semiclassical dynamics for time-resolved spectroscopy

An alternative approach to speeding up QD calculations is to use SC dynamics. While not exact, SC methods can approximately describe all types of QM effects, such as interference, coherence, tunneling, zero-point energies, etc. This distinguishes SC dynamics from classical molecular dynamics that describes the motion of nuclei purely classically even though it may use *ab initio* quantum chemistry methods to compute the electronic PESs.

All SC methods use classical trajectories, but in addition attach phase information to each trajectory. When contributions of various trajectories are added up, this phase

---

permits interference effects, absent in purely classical dynamics. A SC wave function can be generally written as

$$\psi(q,t) = \sum_j A_j e^{i\phi_j}, \quad (2.8)$$

where the sum runs over classical trajectories  $j$ ,  $A_j$  is the square root of classical probability to be at point  $q$  at time  $t$ , and  $\phi_j$  is the corresponding phase. As a result, SC dynamics resembles very much geometrical optics, making QM phenomena more intuitively understandable.

A starting point in all SC methods is the so-called Van-Vleck-Gutzwiller propagator<sup>80</sup> describing the probability amplitude to get from point  $q'$  to point  $q''$  in time  $t$ . This propagator is hard to use in practice because in many-dimensional systems it is very difficult (and expensive) to find all classical trajectories from  $q'$  to  $q''$  in time  $t$ . A clever solution was provided by Miller's initial value representation that transforms this boundary value problem to an initial value problem which is much easier to solve.<sup>81-82</sup> One has to sample the initial coordinates and momenta from a distribution in phase space describing the initial QM state, run trajectories, and at time  $t$  compute the wave function using a formula similar to Eq. (2.8).

Here we focus on four SC initial value methods that provide extensions to Miller's idea by applying it to the coherent states, i.e., Gaussian wave packets (GWPs).<sup>6, 16, 18, 83</sup> The propagated GWPs smooth out wild oscillations in the Van Vleck-Gutzwiller propagator and, as a consequence, GWPs lead to faster convergence. All four methods can be written in the same general form that describes the overlap of an initial GWP  $g_{x_i}$  centered at  $x_i$  with a final GWP  $g_{x_f}$  centered at  $x_f$ ,

$$\langle g_{x_f} | e^{-iHt/\hbar} | g_{x_i} \rangle = h^{-D} \int d^D x^0 C(x^0, t) R(x^0, t) e^{iS(x^0, t)/\hbar}, \quad (2.8)$$

where  $S(x^0, t)$  is the classical action at time  $t$  along a trajectory starting at a phase space point  $x^0 = (q^0, p^0)$  and ending at point  $x^t$ , and  $C$  and  $R$  are factors depending on the method. In the original *Frozen Gaussian Approximation* (FGA),<sup>18</sup> the  $C$  and  $R$  factors are the simplest possible,

$$\begin{aligned} C_{\text{FGA}}(x^0, t) &= \langle g_{x_f} | g_{x^t} \rangle \langle g_{x^0} | g_{x_i} \rangle, \\ R_{\text{FGA}}(x^0, t) &= 1. \end{aligned} \quad (2.8)$$

---

In words, the FGA covers the initial state with GWPs, propagates their centers to time  $t$  while neglecting their spreading (i.e., Gaussians are “frozen” like snowballs<sup>18</sup>), computes the action along each trajectory, and averages the phase factor  $\exp(iS/\hbar)$  over the trajectories. While the FGA is remarkably simple and works surprisingly well, it can be improved in two ways: First, Herman and Kluk corrected the  $R$  factor to get a more accurate and, in fact, uniform SC approximation called the *Herman-Kluk* (HK) *propagator*, in which  $R$  depends on the classical stability matrix.<sup>6</sup> Second, the convergence of the FGA can be sped up by smoothing the frozen Gaussians via (who could have guessed?) new Gaussians. This procedure modifies the  $C$  factors and results in the *cellular dynamics* (CD).<sup>83</sup> Both ideas were used simultaneously in the *cellularized Herman-Kluk* (CHK) *propagator*, originally called *cellularized frozen Gaussian approximation*,<sup>16</sup> which is both the most accurate (due to improved  $R$ ) and the most efficient (due to improved  $C$ ) of the four methods.

Finally, we will compute the correlation function  $f(t, \tau)$  and the time-resolved stimulated emission spectrum using the DR of fidelity, a SC method used to measure the sensitivity of QD to perturbations.<sup>21</sup> In the present setting,

$$f_{\text{DR}}(t, \tau) = h^{-D} \int dx^0 \rho_w(x^0) \exp\left(\frac{i}{\hbar} \int_{\tau}^{\tau+t} dt' (V_1(q') - V_0(q'))\right) \quad (2.8)$$

where  $\rho_w$  is the Wigner-Weyl transform of the initial state and  $V_j$  is the  $j^{\text{th}}$  PES. Each trajectory  $x^t$  is propagated on the excited PES  $V_1$  for time  $\tau$  and subsequently on the average PES  $(V_0 + V_1)/2$  for time  $t$ . The method is analogous to the phase averaging of Mukamel<sup>84</sup> which has been previously used for computing transient absorption spectra by several authors.<sup>28, 32-33</sup>

## 2.6 Results and discussion

### 2.6.1 The system

For numerical tests we chose a two-dimensional system describing the vibrational dynamics of a collinear NCO molecule. Li et al.<sup>85</sup> give an analytical fit to the *ab initio* data for the  $X^2\Pi$  ground and  $A^2\Sigma^+$  excited electronic states, where the NC and CO bond lengths are confined to the interval [2.0-2.6] a.u. In the SC approach it was necessary to have the potential defined on a larger domain and we have thus used an approximate fit

to this potential by a sum of two Morse terms defined in the bond-length coordinates  $r_j$  as

$$V(r_1, r_2) = V_0 + \sum_{j=1,2} D_j \cdot \left(1 - \exp(-\beta_j \cdot (r_j - R_j))\right)^2, \quad (2.8)$$

and coupled via the kinetic term. The fitted parameters (atomic units are used throughout this paper) are listed in Table 2. In mass-scaled normal mode coordinates and within the harmonic approximation, the ground vibrational state of the  $X^2\Pi$  surface is a single GWP with the widths equal to 14.44 and 10.35. The exact ground state was found by imaginary-time propagation<sup>86</sup> of the above-mentioned GWP. In numerical tests, this exact ground state was approximated by fitting to a Gaussian form, which resulted in slightly different widths, namely 14.55 and 10.43. For calculation of the pump-probe spectra, a nonstationary initial state was generated by a pump-dump technique,<sup>87</sup> in which the original state was promoted to the upper surface, propagated there for a net time of 520 a.u., dumped to the lower surface, and propagated there for additional 480 a.u. The shape of the resulting wave packet resembled again a single shifted GWP<sup>88</sup> to which it was fitted.

Table 2: Parameters (in a.u.) of the approximative potential fit from Eq. (12).

	$R_1$	$R_2$	$D_1$	$D_2$	$\beta_1$	$\beta_2$	$V_0$
$X^2\Pi$	2.302	2.246	0.1273	0.1419	1.414	1.718	-167.653
$A^2\Sigma^+$	2.234	2.232	0.1432	0.1417	1.516	1.816	-167.548

## 2.6.2 Efficiency of various split-operator methods

Before showing the time-resolved spectra, we compare the efficiency of the various split-operator methods. Besides the number of FFTs, the efficiency is determined predominantly by the size  $\Delta t$  of the time step that introduces a fixed discretization error (determined, e.g., by machine precision) to the wave function after each step. The faster a propagation method converges, the larger the time step can be chosen. Figure 2 shows the error of the wave function propagated for time  $t = 128$  a.u. on the  $A^2\Sigma^+$  PES as a function of  $\Delta t$  for different split operator algorithms. The error is defined as  $\|\psi_{\Delta t}(t) - \psi_0(t)\|$  where  $\psi_0(t)$  is the benchmark wave function propagated with the same method and a very small time step of  $2^{-9}$ , i.e., 0.00195 a.u.

Figure 2 shows that the complex propagation schemes SO3-C and SO4-C are unstable for time steps larger than 6.4 and 4 a.u., respectively, due to the non-unitary propaga-

tion.<sup>76</sup> A rough estimate on the maximal time step size can be deduced from the near-unitarity condition on the kinetic evolution operator  $U_T$ . Employing the Heisenberg uncertainty relation, the maximal momentum is related to the grid spacing  $\Delta q$  as  $p_{\max} \leq \pi\hbar / \Delta q$ . In order for  $U_T$  to be almost unitary, the time step  $\Delta t$  has to fulfill the condition

$$\Delta t < \frac{2m\Delta q^2}{\pi^2\hbar \text{Im} z}, \quad (2.9)$$

where  $z$  is the complex splitting constant. The denser the grid in coordinate space, the larger the maximal phase in the kinetic term, and the smaller the maximal  $\Delta t$  for complex splitting propagation. For a grid spacing of 4 a.u. in each dimension  $\Delta t$  has to be smaller than 22 a.u. which corresponds to the actual behavior of the SO4-C and SO3-C methods. The earlier breakdown of the SO4-C method is due to the combined effect of the last and the first splitting step of each time step, resulting in a larger effective time step.

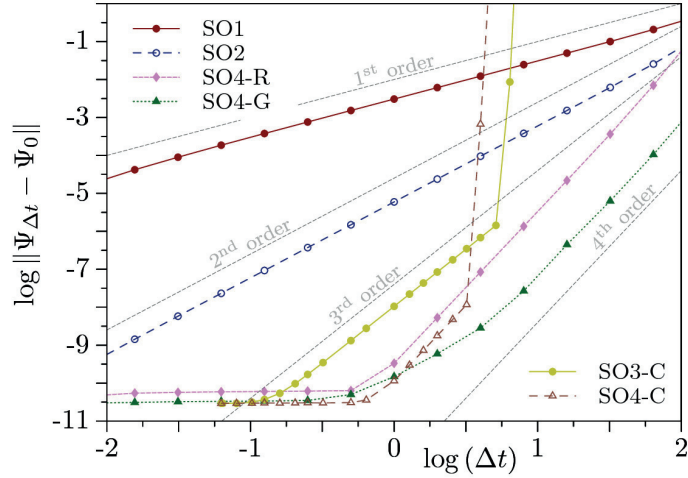


Figure 2 - Error of the quantum wave function (at time  $t = 128$  a.u.) as a function of the time step  $\Delta t$  (in a.u.) for various split-operator methods.

Incidentally, for very dense grids, the 4<sup>th</sup> order splitting with real coefficients (SO4-R) also runs into difficulties by effectively exhibiting a second order behavior. The culprit could be related to the numerical issues resulting from large phase factors in the kinetic evolution operator following again directly from the uncertainty relations. Finally, in the opposite case of a very *low* grid density, the predicted 4<sup>th</sup> order convergence of SO4-G deteriorated to the 2<sup>nd</sup> order. To conclude, high order methods can result in much small-



er errors and a much higher efficiency, but they must be used with great care as the errors depend strongly on the grid spacing.<sup>70</sup>

### 2.6.3 Time-resolved spectra and correlation functions

Numerical tests consisted in the computation of the correlation function and transient spectrum, i.e., quantities defined in Eqs. (2.2) and (2.3), where  $U_0$  and  $U_1$  denote the evolution operators corresponding to the  $X^2\Pi$  and  $A^2\Sigma^+$  electronic states, respectively. Panel (a) of Figure 3 depicts the resulting benchmark QM transient stimulated emission spectra<sup>89</sup> calculated using the 4<sup>th</sup> order split operator method SO4-R with a time step  $\Delta t = 5$  a.u. Prior to the actual spectra calculation by the Fourier transform (2.3), the correlation function (2.2) was damped<sup>16</sup> by a Gaussian decay function  $\exp(-t^2/T^2)$  with  $T$  set to  $10^4$  a.u. (see Figure 4).

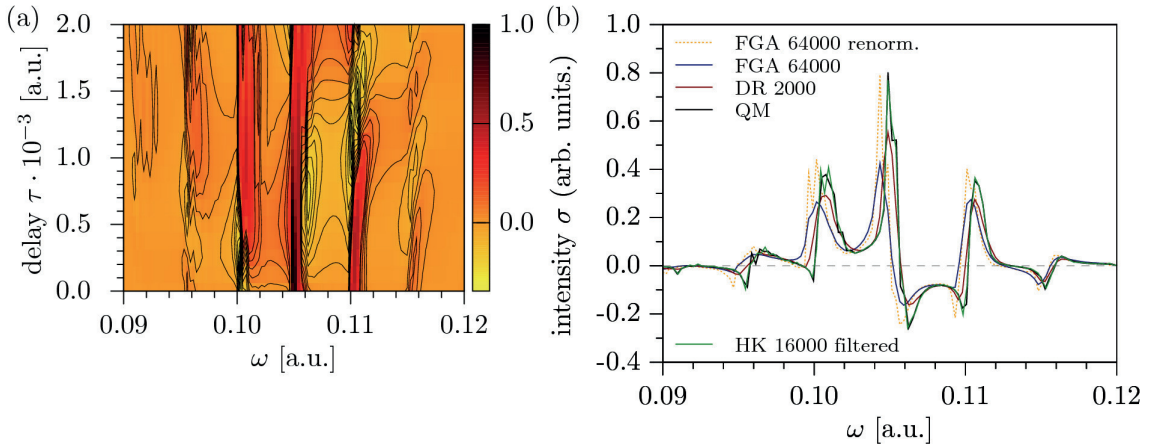


Figure 3 - Pump-probe stimulated emission spectra: (a) Quantum results (contours are plotted for intensities from -0.34 to 0.2 at intervals of 0.04). (b) Semiclassical results for the delay time of 300 a.u. (the number of trajectories used is shown after the name of the approximation).

Panel (b) of Figure 3 compares QM and converged SC spectra computed at a specific delay time  $\tau$  of 300 a.u. All SC calculations used a SC symplectic integrator that we have designed based on Chin's 4<sup>th</sup> order classical symplectic integrator utilizing force gradients.<sup>79</sup> Chin's integrator, in turn, is a classical analog of the QM propagator SO4-G.

The original FGA method reproduces the spectrum at least qualitatively; nevertheless it is improved by a repeated renormalization of the correlation function  $f$  [see Figure 3(b)]. While the HK method with filtering (to be explained below) gives almost exact spec-

---

trum, the DR spectrum is reasonably accurate yet converges with much fewer trajectories.

A stringent criterion on the accuracy of various SC methods is the undamped correlation function  $f(t, \tau)$ ; its absolute value squared is shown in Figure 4. In agreement with conclusions made by Kay as well as Walton and Manolopoulos,<sup>16, 90-91</sup> we observed that the convergence of the HK is significantly slowed down by just a few trajectories the prefactor of which grows exponentially fast in time [see Figure 4(a)]. We were unable to obtain sensible results based on the implementation of the original HK method for times larger than, roughly,  $10^4$  a.u. Similar observation led Walton and Manolopoulos to the introduction of the CHK method mentioned above.<sup>16</sup> Nevertheless, as pointed out by Kay,<sup>90</sup> even a much simpler heuristic approach, consisting in a repeated elimination of trajectories with the largest prefactors, can lead to reasonable results. Figure 4(a) supports this claim: The green dashed line represents HK results for 64000 trajectories whereas the solid red line corresponds to the “filtered HK” results obtained using this heuristic procedure with just 16000 trajectories (fewer than 1% of the trajectories had to be discarded). Finally, Figure 4(b) compares the FGA and the DR with the QM result. Once again, the renormalization greatly improves the FGA. Unlike the filtered HK method and renormalized FGA, the DR cannot unfortunately describe the recurrence of  $|f(t, \tau)|$  after 8000 a.u. However, this should not matter at finite temperature or in the condensed phase where the magnitude of the recurrence will be greatly diminished due to the coupling to the environment, and its effect on the spectrum will be very small. This was already demonstrated by Figure 3(b), where the spectra were computed from damped correlation functions. We should also highlight the computational efficiency of the DR which, unlike the HK method, does not require the Hessian of the potential, and, moreover, as can be seen in Figure 4(a), converges with much fewer trajectories than both the FGA and the HK method. In fact, the work in our group has demonstrated that under quite general assumptions, the number of trajectories required in the DR is independent of dimensionality.<sup>44</sup> Finally, we currently work on speeding up the DR even further, using ideas similar to those behind the CD or CHK propagator.

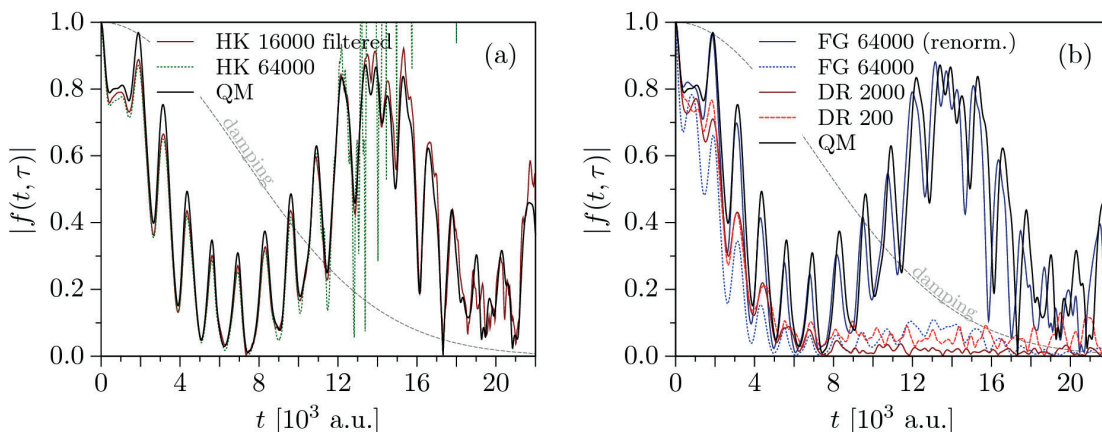


Figure 4 - The magnitude of the time-dependent correlation function as a function of time computed with various SC methods. (The number of trajectories used is shown after the name of the method.) (a) The slow convergence of the HK method can be remedied by heuristic filtering out of trajectories with exponentially growing prefactors. (b) The improvement of the FGA by renormalization and the fast convergence of the DR. [The displayed correlation functions were multiplied by the damping function (shown by a dashed gray curve) in order to obtain finite-resolution spectra in Figure 3.]

## 2.7 Conclusion

In summary, we have presented, analyzed, and compared several conceptual approaches intended for speeding up the quantum dynamics calculation of ultrafast time-resolved spectra.

In case of quantum dynamics performed on an equidistant grid using split operator approach, higher-order splitting schemes yield higher efficiency, but care has to be taken as to their numerical stability with respect to the grid spacing.

As for the semiclassical methods, we demonstrate that the DR requires much fewer trajectories than the FGA and HK propagators even if one employs renormalization in the former or primitive "cellularization" by means of trajectory filtering in the latter case. However, unlike FGA and/or HK, the DR reproduces with sufficient accuracy only the first decay of the correlation function. Nevertheless, for reasons discussed above, the importance of the recurrences in the correlation function is typically marginal. For practical purposes, the DR spectra are thus competitive with the, otherwise presumably more accurate, HK spectra. This is especially attractive from the computational point of view since the DR does not require any costly renormalization and/or knowledge of the Hessian of the PES.

---

Finally, we would like to remark that the method denoted above as FGA is not, strictly speaking, a direct implementation of the original Frozen Gaussian Approximation proposed by Heller.<sup>18</sup> The main discrepancy lies in the fact that the action in the phase factor accompanying each evolving GWP is calculated on the basis of local potential, i.e., it corresponds to the classical action of the classical trajectory traced out by the evolving GWP's center, while the original approach employs potential averaged over the full GWP, i.e., mean value of the potential in the GWP state instead of the value of the potential at the GWP's center. In this spirit, our modified FGA propagator employing classical action and repetitive renormalization closely resembles the poor-person's HK propagator published almost simultaneously by Tatchen et al.<sup>12</sup>

---

## Chapter 3 On-the-fly *ab initio* semiclassical dynamics: Identifying degrees of freedom essential for emission spectra of oligothiophenes

Chemists are not only interested in small molecules. Well-established semiclassical methods, however, already require several thousand trajectories in a 2-dimensional system (see Chapter 2), and DR can only describe the envelopes of the electronic spectra of larger molecular systems (see Subsection 1.4). The approach I have chosen is to take a rather crude approximation—the thawed Gaussian approximation (TGA) and combine it with an on-the-fly scheme to avoid a cumbersome prescreening of the potential energy surfaces. The TGA has several desirable properties: First, in harmonic systems, the most important simplified models of molecules, it is exact. Second, the initial dynamics, which is the most important determinant of moderately resolved spectra, is well described for general potentials. Finally, the TGA is simple and computationally less expensive than other semiclassical methods.

Oligothiophenes were suitable to study this approach due to their scalability and marked dependence of the emission spectra on the number of rings. In order to explain this effect, we introduced a systematic approach to decode spectra computed with TGA. The content of this chapter has been published in the *Journal of Chemical Physics*.<sup>58</sup>

### 3.1 Abstract

Vibrationally resolved spectra provide a stringent test of the accuracy of theoretical calculations. We combine the thawed Gaussian approximation (TGA) with an on-the-fly *ab initio* (OTF-AI) scheme to calculate the vibrationally resolved emission spectra of oligothiophenes with up to five rings. The efficiency of the OTF-AI-TGA permits treat-

---

ing all vibrational degrees of freedom on an equal footing even in pentathiophene with 105 vibrational degrees of freedom, thus obviating the need for the global harmonic approximation, popular for large systems. Besides reproducing almost perfectly the experimental emission spectra, in order to provide a deeper insight into the associated physical and chemical processes, we also develop a novel systematic approach to assess the importance and coupling between individual vibrational degrees of freedom during the dynamics. This allows us to explain how the vibrational line shapes of the oligothiophenes change with increasing number of rings. Furthermore, we observe the dynamical interplay between the quinoid and aromatic characters of individual rings in the oligothiophene chain during the dynamics and confirm that the quinoid character prevails in the center of the chain.

### 3.2 Introduction

Polythiophenes ( $T_n$ ) and their functional derivatives belong among the most studied compounds among  $\pi$ -conjugated polymers due to their potential in organic electronics,<sup>92-95</sup> since they combine remarkable conductivity with excellent thermo- and chemo-stability. Detailed experimental investigations of polythiophenes have shown that their optical properties are closely related to the structure of the polymer backbone: For instance, the 0–0 transition energies are approximately a linear function of  $1/n$ , where  $n$  is the number of thiophene rings in the polymer.<sup>96-98</sup> Bandgap computations confirmed validity of this semi-empirical rule for short polymers as well as its violation for longer chains.<sup>99-101</sup>

For a direct comparison with experiments it is, however, crucial to calculate the vibrationally resolved spectra.<sup>102-103</sup> Here, we therefore determine the vibrationally resolved emission spectra of oligothiophenes  $T_n$  with two to five rings, i.e.,  $n \in \{2,3,4,5\}$ , since the vibrational line shape is changing drastically in this range of  $n$ .<sup>98</sup>

The cost of computing a vibrationally resolved spectrum is much higher than the cost of vertical transition energy calculations since the spectrum calculation requires the knowledge of the involved potential energy surfaces (PESs). As it is often difficult to describe PESs accurately in terms of analytical functions, a popular approach, especially for larger molecules is to approximate the PESs by harmonic potentials with respect to certain reference structures.<sup>104-107</sup> The absorption and emission line shapes of dithiophene have been calculated by Stendardo *et al.*<sup>108</sup> using a double-well potential describing the torsional mode and global harmonic approximation in the remaining degrees of freedom. In order to get a good correspondence with experiment, the authors show that

---

an appropriate choice of these reference structures is essential, e.g., the ground PES reference structure for the emission spectrum calculation is found using symmetry constraints.

Alternative strategy employs trajectory-based methods in combination with an on-the-fly (OTF) *ab initio* (AI) scheme, in which the required potential energies, forces, and Hessians are computed with an electronic structure package during the dynamics. It is becoming increasingly clear that *ab initio* semiclassical dynamics provides a powerful spectroscopic tool useful, e.g., for evaluating internal conversion rates<sup>109</sup> or vibrationally resolved spectra.<sup>19, 110-113</sup> Not only do the evolving trajectories provide an intuitive classical-like picture of the underlying physical and chemical processes, but via interference, they also partially account for the most important nuclear quantum effects. The overall computational cost, however, restricts almost all of these methods to small systems.

As a result, one is forced to strike a balance between physical accuracy and computational efficiency. In this spirit, OTF-AI Gaussian wave packet propagation can provide a useful compromise. Within the thawed Gaussian approximation (TGA), the nuclear wave packet is guided by a central classical trajectory, which feels the anharmonicity of the potential, while its width is propagated using the local harmonic approximation.<sup>50</sup> Hence, the effects of anharmonic or double-well potentials are partially captured by TGA; moreover, the OTF-AI framework obviates the need of an a priori knowledge of the landscape of the final PES. More importantly, due to its moderate computational cost, TGA can treat all vibrational degrees of freedom on an equal footing even in large systems, while in smaller systems, it permits using a more accurate electronic structure description. A well-known shortcoming of the TGA is that it captures accurately only the short-time dynamics and, therefore, only describes the broad spectral features.<sup>1</sup> Nevertheless, due to interaction with solvent and other phenomena contributing to spectral broadening, the experimental spectra are also typically not fully vibrationally resolved.

Although rewarding, a mere reproduction of an experimental spectrum, no matter how accurate, does not provide a deeper insight into the associated physical and chemical processes; it is a careful analysis of the simulation that can provide such information. The extraction of this essential information, which is often omitted, can be as difficult as the simulation itself, especially for larger molecules. For example, explanation of changes in the vibrational line shape of the spectra due to increasing polymer chain length, which is done here for oligothiophenes, increases drastically the complexity of the analysis. Therefore, in addition to providing an efficient computational protocol for

---

computing vibrationally resolved electronic spectra we also present a systematic approach for extracting the essential information about the underlying dynamics.

### 3.3 Theory

#### 3.3.1 Emission spectrum calculation

Analogously to absorption spectrum evaluation [Eqs. (1.18) and (1.19)], the correlation function relevant for emission spectrum is computed by propagating ground vibrational state of the excited electronic state  $S_1$  on the ground electronic surface  $S_0$ . Within the electric dipole approximation, time-dependent perturbation theory, and Condon approximation, the correlation function is

$$C_{\text{em}}(t) = \langle \Psi_{\text{init}} | e^{-i\hat{H}_{S_0}t/\hbar} | \Psi_{\text{init}} \rangle, \quad (3.1)$$

where  $|\psi_{\text{init}}\rangle$  is the ground vibrational state of  $S_1$  with energy  $E_{S_1}$ . The spectrum is then obtained via Fourier transform

$$\sigma(\omega) = A\omega^k \int C_{\text{em}}(t) e^{i(\omega + E_{S_1}/\hbar)t} dt, \quad (3.2)$$

where  $k = 0$  for the line shape and  $k = 3$  for the emission spectrum in contrast to absorption spectrum [Eq. (1.19)] for which  $k = 1$ . Prefactor  $A$  is a constant factor depending on the type of spectra.<sup>102, 104, 114</sup> Since it is constant, in our calculations  $A$  was chosen so that the spectra are normalized in the  $L^\infty$  norm, i.e., the highest spectral peak is of unit intensity.

#### 3.3.2 Stability matrix propagation: Symplecticity and effect of Hessian interpolation

The GWP's center and the accompanying stability matrix  $M^t$  are propagated classically using the second-order symplectic algorithm.<sup>10</sup> Propagation of  $M^t$  is the most expensive part of the entire OTF-AI calculation since it requires knowledge of the Hessian of the PES along the evolving trajectory.

The associated computational costs can be alleviated by employing a Hessian update scheme, within which the Hessian is evaluated directly only once every  $s \geq 1$  steps and approximated at the remaining steps with an extrapolation method requiring gradients. Note that these Hessian update schemes are in the context of dynamics typically used for the propagation of the classical trajectory itself, e.g., within the framework of high-



---

er-order predictor-corrector schemes (see Refs. [115-119] and references therein). In contrast, in Refs. [109], [120], and [121] as well as in the present work, approximative treatment of the Hessian is used only for the propagation of  $M^t$ . However, whereas in Refs. [109], [120], and [121] the Hessian update is based on extrapolation, in this work polynomial interpolation of order  $b$  is used to obtain the Hessian at intermediate steps. A Hessian extrapolation update scheme would be convenient in cases for which analytical *ab initio* Hessians are not available, e.g., for absorption spectrum calculation.

Note that our approach requires propagating the full classical trajectory and storing the necessary information regarding the potential first, and interpolating the Hessian later. The TGA GWP is computed in the second pass through the stored data. The advantage of this approach is twofold: First, the independent Hessian calculations in the second pass are easily parallelized. Second, one can perform a global analysis of the trajectory (see Subsection 3.3.3) over the entire propagation range.

As the first test, we check the conservation of the *symplectic condition*

$$M^{tT} \cdot J \cdot M^t = J \quad (3.3)$$

by the  $2D \times 2D$  stability matrix  $M^t$ , where  $J$  is the standard symplectic matrix

$$J := \begin{pmatrix} 0_D & I_D \\ -I_D & 0_D \end{pmatrix} \quad (3.4)$$

and  $I_D$  is the  $D$ -dimensional identity matrix. The deviation from Eq. (3.3) is evaluated in terms of the error

$$\varepsilon^t := \| M^{tT} \cdot J \cdot M^t - J \|_{\mathbb{F}}, \quad (3.5)$$

where  $\| A \|_{\mathbb{F}} := \sqrt{\text{Tr}(A^T \cdot A)} = \sqrt{\sum_{i=1}^{2D} \sum_{j=1}^{2D} |A_{ij}|^2}$  denotes the Frobenius norm of matrix  $A$  and the exact stability matrix satisfies

$$\varepsilon^t = 0. \quad (3.6)$$

For instance, in the T2 calculation, Eq. (3.6) is well satisfied even for Hessian interpolated from AI values computed only every 2, 4, 8, or 16 steps [see Figure 5(a)]. It is important to note that any violations of Eq. (3.5) are due to round-off errors, since in an infinite-precision arithmetics, Eq. (3.6) would be satisfied even if the true Hessian were replaced by an arbitrary symmetric matrix  $\mathcal{H}^t$ . The only additional requirement is that

$M^t$  be propagated symplectically,<sup>10</sup> since the symmetry of  $\mathcal{H}^t$  is guaranteed by the interpolation algorithm. Incidentally, note that Eq. (3.6) is much more stringent than the widely used Liouville condition, which only requires conservation of the phase-space volume, expressed by the requirement  $\det(M^{t^T} \cdot M^t) = 1$ , and automatically follows from symplecticity [Eq. (3.6)].

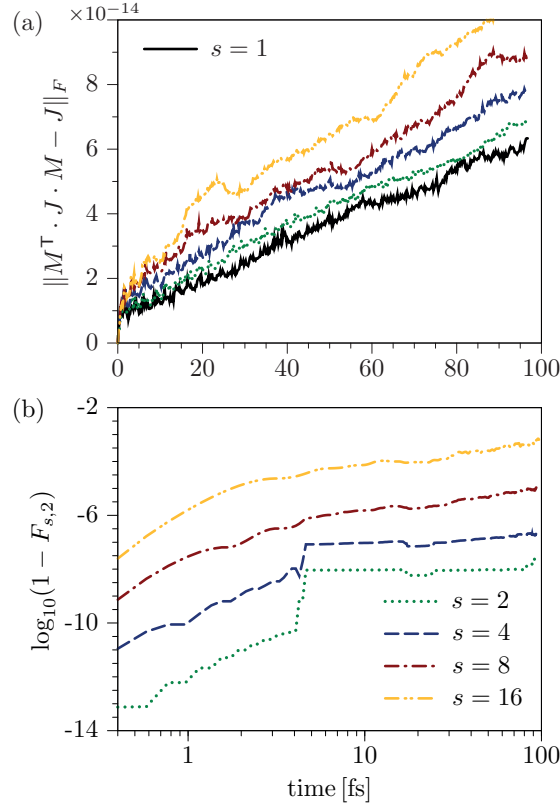


Figure 5: Effects of Hessian interpolation scheme of second order ( $b = 2$ ) for several sizes of the interpolation interval  $s$ . Panel (a): Extent of the violation of the symplectic condition Eq. (3.6). Panel (b): Accuracy of the quantum dynamics measured with fidelity  $F_{s,b}(t)$  introduced in Eq. (3.7).

The influence of the interpolation procedure with  $s > 1, b \geq 0$  on the GWP evolved with the TGA is quantified in terms of fidelity—a quantity introduced by Peres<sup>25</sup> to measure sensitivity of quantum dynamics to perturbations. In our setting, the fidelity is defined as the squared magnitude of the time-dependent overlap of GWPs propagated using the TGA with and without interpolation:

$$F_{s,b}(t) := \left| \langle \psi_{1,b}^t | \psi_{s,b}^t \rangle \right|^2. \quad (3.7)$$

---

In the T2 case, e.g., interpolating every four steps using the second order interpolation ( $b = 2$ ) has almost no effect on the propagated GWP [see Figure 5(b)], while the OTF-AI calculation is accelerated almost four times.

### 3.3.3 Identification of the essential DOFs

Perhaps the greatest advantage of trajectory-based methods is the possibility to visualize the dynamics and directly study its influence on the resulting spectra. However, direct analysis can become quite cumbersome for systems of high dimensionality. Moreover, the dynamical couplings among individual degrees of freedom (DOFs) pose additional complications since all the coupled DOFs must be analyzed simultaneously. In this subsection, we introduce a particular approach for extracting the essential characteristics of the dynamics of a generic system with  $D$  vibrational DOFs. To some extent, this method shares common grounds with other “effective modes” techniques aspiring to identify the modes responsible for the main spectral features, e.g., methods tailored for the description of nonadiabatic transitions.<sup>122-123</sup> However, in contrast to Refs. [122-123], the identification of the essential DOFs is here performed on the fly. The “tool” proposed here is used in Subsection 3.5.2 for analyzing and interpreting the emission spectra of the oligothiophene  $T_n$  family.

In order to simplify the discussion below, we introduce the symbol  $\mathcal{D}$  to denote the space spanned by all  $D$  DOFs. Any subspace of  $\mathcal{D}$  is then identified with the subset of indexes of those DOFs that span the given subspace. In this spirit,  $\mathcal{D}$  itself is identified with the set  $\mathcal{D} = \{1, 2, \dots, D\}$ . Note that the set of normal mode coordinates provide a natural physical realization of  $\mathcal{D}$ , nevertheless our approach is not limited to this particular choice.

Briefly put, our strategy is as follows. First, we decompose the set  $\mathcal{D}$  of all vibrational DOFs into mutually disjoint subsets, where the DOFs in different subsets can be thought of as approximately dynamically independent. Second, we identify the dynamically most important DOFs and then consider only those subsets of  $\mathcal{D}$  which contain at least one of these “important” DOFs.

To quantify the coupling between various DOFs, we utilize the stability matrix to measure the *information flow* among individual DOFs. The “flow”  $B_{ij}$  between  $i$ th and  $j$ th DOF is then defined as

---


$$B_{ij} := \left| \frac{\beta_{ij}}{\beta_{ii}} \right|, \text{ with } \beta := \frac{1}{T} \int_0^T dt \kappa^T \cdot \tilde{M}^t \cdot \kappa, \quad (3.8)$$

where  $\tilde{M}_{ij}^t = |M_{ij}^t|$  and  $\kappa^T = (I_D, I_D)$  denotes a two-component vector, each component of which is a  $D$ -dimensional identity matrix. The value of  $\beta_{ij}$  is rescaled in Eq. (3.8) by  $1/\beta_{ii}$  in order to make the diagonal elements unital ( $B_{ii} = 1$ ), as in uncoupled systems, and to focus solely on the coupling effects among different DOFs ( $i \neq j$ ).

The decomposition of  $\mathcal{D}$  into (approximately) dynamically decoupled subsets of DOFs is then constructed by means of the concept of  $\varepsilon_B$ -partitioning:

$$\mathcal{D} = \bigcup_{\alpha=1}^{\bar{c}(\mathcal{D}, \varepsilon_B)} \mathcal{D}_\alpha^{\varepsilon_B}, \quad (3.9)$$

where  $\bar{c}(\mathcal{D}, \varepsilon_B)$  denotes the number of mutually disjoint subsets  $\mathcal{D}_\alpha^{\varepsilon_B}$  defined as the maximal connected components of an undirected graph with adjacency matrix

$$E_{ij} := \begin{cases} 1 & \text{if } \max\{B_{ij}, B_{ji}\} \geq \varepsilon_B \\ 0 & \text{otherwise} \end{cases}, \quad (3.10)$$

with a particular threshold value  $\varepsilon_B$ .

Any nontrivial decomposition (3.9), where each subset  $\mathcal{D}_\alpha^{\varepsilon_B}$  is interpreted as uncoupled, yields a partially separable dynamics. Depending on the value  $\bar{c}(\mathcal{D}, \varepsilon_B)$ , this separation can significantly reduce computational costs, since the total correlation function can be obtained as a product of individual contributions evaluated independently on each subspace (i.e., subset  $\mathcal{D}_\alpha^{\varepsilon_B}$ ).

Next, we identify the set  $\mathcal{G}^{\varepsilon_e} \subseteq \mathcal{D}$  of the dynamically most important DOFs. For this purpose, we employ the *relative displacement* vector  $\varrho$ , the  $i$ th component of which is defined as the maximal relative displacement in the coordinate  $\zeta_i$ , describing the  $i$ th DOF, where the maximum is understood to be taken over the total propagation range  $[0, T]$ , i.e.,

$$\varrho_i := \max_{0 \leq t \leq T} |\zeta_i^t| (A_{ii}^0 / \ln 2)^{1/2} \text{ for } 1 \leq i \leq D. \quad (3.11)$$

Here, the scaling factor containing the diagonal element  $A_{ii}^0$  of the width matrix of the initial GWP ensures that the spread of the nuclear wave function be taken into account: A small displacement of a high-frequency (stiff) mode modulates the correlation func-

---

tion much more than the same displacement of a low-frequency (soft) mode. The set  $\mathcal{G}^{\varepsilon_\rho}$  of dynamically most important modes is then defined by

$$i \in \mathcal{G}^{\varepsilon_\rho} \Leftrightarrow \rho_i \geq \varepsilon_\rho, \quad (3.12)$$

where  $\varepsilon_\rho$  is a prescribed threshold value. A particular DOF is thus interpreted as “dynamically important” if the dynamics displaces it sufficiently relative to the width of the initial vibrational state.

Finally, we combine the two ideas, i.e. the decoupling based on the  $\varepsilon_B$ -partitioning [Eq. (3.9)], and the selection of important modes based on the relative displacement  $\rho$  [Eq. (3.11)], to form an “active space”  $\mathcal{A}^{\varepsilon_B, \varepsilon_\rho}$  comprised of all subsets  $\mathcal{D}_\alpha^{\varepsilon_B}$  containing at least one dynamically important DOF from  $\mathcal{G}^{\varepsilon_\rho}$ :

$$\mathcal{A}^{\varepsilon_B, \varepsilon_\rho} = \bigcup_{\alpha \in \mathcal{S}} \mathcal{D}_\alpha^{\varepsilon_B}, \text{ with } \mathcal{S} := \{\beta: \mathcal{G}^{\varepsilon_\rho} \cap \mathcal{D}_\beta^{\varepsilon_B} \neq \emptyset\}. \quad (3.13)$$

Note that the number  $c(\mathcal{D}, \varepsilon_B, \varepsilon_\rho) := |\mathcal{S}|$  of contributing subsets  $\mathcal{D}_\alpha^{\varepsilon_B}$  is in general smaller than  $\bar{c}(\mathcal{D}, \varepsilon_B)$  of Eq. (3.9). In order to obtain a contiguous labeling of the subsets in decomposition (3.13), we introduce a bijective (but otherwise arbitrary) mapping  $l$  between sets  $\mathcal{S}$  and  $\{1, \dots, c(\mathcal{D}, \varepsilon_B, \varepsilon_\rho)\}$ . This allows to restate Eq. (3.13) as

$$\mathcal{A}^{\varepsilon_B, \varepsilon_\rho} = \bigcup_{\alpha=1}^{c(\mathcal{D}, \varepsilon_B, \varepsilon_\rho)} \mathcal{A}_\alpha^{\varepsilon_B, \varepsilon_\rho}, \text{ where } \mathcal{A}_\alpha^{\varepsilon_B, \varepsilon_\rho} := \mathcal{D}_{l(\alpha)}^{\varepsilon_B}. \quad (3.14)$$

The subsets  $\mathcal{A}_\alpha^{\varepsilon_B, \varepsilon_\rho}$  are in the following referred to as *groups*. (Mathematically, these “groups” are just “sets” and should not be confused with a precise mathematical notation of group.)

In summary, individual DOFs are by definition considered to be coupled only within groups the union of which forms the space  $\mathcal{A}^{\varepsilon_B, \varepsilon_\rho}$ . Each group then contains at least one DOF classified as dynamically important on the basis of the rule (3.12). The total number of groups  $c(\mathcal{D}, \varepsilon_B, \varepsilon_\rho)$  and their structure is mainly determined by the values of the two thresholds  $\varepsilon_\rho$  and  $\varepsilon_B$  which have to be chosen appropriately according to the system and process of interest.

Let us now demonstrate the approach outlined above on one particular example of T2, the dithiophene molecule. Since an oligothiophene  $Tn$  is comprised of

$$N(n) = 7n + 2 \quad (3.15)$$

atoms, the space  $\mathcal{D}$  is of dimensionality  $D(n) := 3N(n) - 6 = 21n$ , i.e., in the case of T2 ( $n = 2$ ), there are 42 vibrational DOFs. To be explicit, these vibrational DOFs are identified with normal-mode coordinates of PES  $S_1$ . Individual modes are in Figure 6 represented by colored circles with juxtaposed vibrational frequencies. Now, for  $\varepsilon_B = 0.045$ , one obtains 4 subsets in the decomposition (3.9), i.e.,  $\bar{c}(\mathcal{D}, \varepsilon_B) = 4$ . Further, we identify the set of important modes  $\mathcal{G}$  using rule (3.12). With threshold value  $\varepsilon_Q = 0.6$ , we isolate 8 modes, i.e.,  $|\mathcal{G}^{\varepsilon_Q}| = 8$ . These modes are shown in red color in Figure 6. Finally, we see that for this choice of the thresholds, we obtain only one group in the decomposition (3.14) since  $\mathcal{G}^{\varepsilon_Q} \cap \mathcal{D}_\beta^{\varepsilon_B} \neq \emptyset$  only for  $\beta = 1$ . Thus  $c(\mathcal{D}, \varepsilon_B, \varepsilon_Q) = 1$  and the bijective mapping  $l$  is merely an identity.

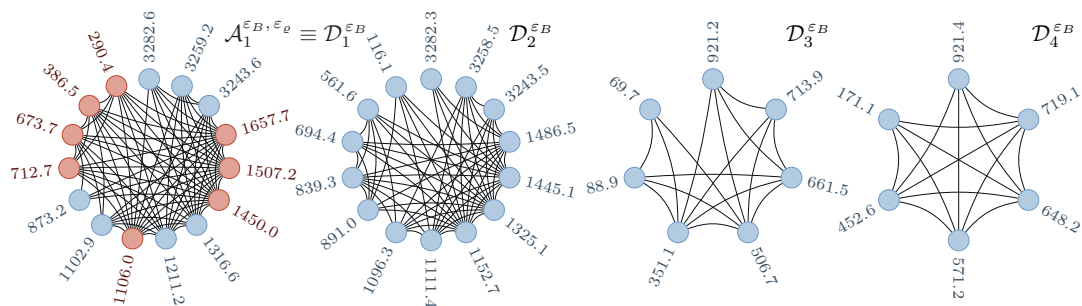


Figure 6: Partitioning of  $S_1$  normal-mode coordinates of dithiophene T2 into approximately independent subsets for the threshold value  $\varepsilon_B = 0.045$  [see Eq. (3.9)]. Colored circles represent individual modes, i.e., elements of  $\mathcal{D}$ . The dynamically important modes [Eq. (3.12)] comprising  $\mathcal{G}^{\varepsilon_Q}$  with the threshold value  $\varepsilon_Q = 0.6$  are shown in red. Finally, solid lines represent inter-mode couplings above the threshold  $\varepsilon_B$ . Vibrational frequencies are given in  $\text{cm}^{-1}$ .

In practical calculations,  $\varepsilon_Q$  and  $\varepsilon_B$  must be chosen carefully. For high threshold values  $\varepsilon_B$ , one can profit from an approximate separability of the model. However, too high values of either  $\varepsilon_B$  or  $\varepsilon_Q$  might yield inaccurate results.

### 3.3.4 TGA in subspaces of reduced dimensionality

One of the main goals of the normal mode analysis elaborated in previous subsection is identifying the normal modes essential for the dynamics. Restriction to these most important modes allows one to devise a simplified model of reduced dimensionality, e.g., in the spirit of the well-studied pyrazine vibronic coupling model.<sup>124</sup> Moreover, this reduction also broadens the class of computationally available methods. After the reduc-

---

tion, one may be able to employ, e.g., the Gaussian basis methods,<sup>125-127</sup> or various approaches from the family of the semiclassical initial value representation.<sup>7, 17, 128-129</sup>

Let us consider a system with  $D$  vibrational DOFs. In a typical OTF-AI-TGA calculation, one evolves the  $D$ -dimensional GWP by classically propagating its center  $x^t$  and by evaluating the phase factor  $\gamma^t$  and the complex time-dependent width matrix  $A^t$  by means of Lee and Heller's  $P$ - $Z$  algorithm<sup>51</sup> summarized in Section 1.4 [Eqs. (1.32) and (1.35)].

As in Subsection 3.3.3, we identify the  $D$ -dimensional space of vibrational DOFs with the set  $\mathcal{D} = \{1, \dots, D\}$ . We would like to take advantage of the stored  $D$ -dimensional trajectory information, and, at the same time, to restrict ourselves to a subset  $\mathcal{P} \subseteq \mathcal{D}$  of only  $d < D$  most important vibrational degrees of freedom and define a linear projection  $\pi: \mathbb{R}^D \rightarrow \mathbb{R}^d$  from the full space of  $D$  vibrational DOFs to the subspace of physical interest. Formally

$$\pi_{ij} := \delta_{\mathcal{P}_i, j} \text{ for } 1 \leq i \leq d \text{ and } 1 \leq j \leq D, \quad (3.16)$$

where  $\mathcal{P}_i$  denotes the  $i$ th element of the ordered set  $\mathcal{P}$ .

The “reduced”  $d$ -dimensional GWP is again propagated using the  $P$ - $Z$  formalism. However, if  $(q^t, p^t)$  denotes the trajectory followed by the original,  $D$ -dimensional GWP, then the center of the reduced Gaussian follows a classical trajectory  $(\pi \cdot q^t, \pi \cdot p^t)$  in the reduced,  $2d$ -dimensional phase space. Also, the initial conditions for the time-dependent  $P^t, Z^t$  matrices must be replaced with

$$\bar{Z}^0 = \pi \cdot \pi^T = I_d, \quad (3.17)$$

$$\bar{P}^0 = 2i\hbar\pi \cdot A^0 \cdot \pi^T. \quad (3.18)$$

Here,  $d$ -dimensional matrices are denoted with a bar and  $A^0$  is the initial width matrix of the  $D$ -dimensional GWP.

Finally, we need to isolate the  $\mathcal{P}$ -contribution to the effective Lagrangian  $\mathcal{L}_{\text{eff}}$ , which is required in Eq. (1.35) for evaluating the time-dependent complex phase  $\gamma^t$ . This is conveniently done using conservation of energy, since in all our calculations we consider only stationary initial states. Therefore,

$$\frac{1}{2}\zeta^{tT} \cdot \zeta^t + V(\eta^t) = V(\eta^0), \quad (3.19)$$

---

with  $\zeta$  denoting momentum conjugated to  $\eta$ ; mass factors do not explicitly appear since  $\eta$  is already mass-scaled. Using Eq. (3.19), the  $\mathcal{L}_{\text{eff}}$ -contribution to  $\gamma^t$  in Eq. (1.35) then reads

$$\begin{aligned} \int_0^t \mathcal{L}_{\text{eff}}^\tau d\tau &= \int_0^t \left[ \frac{1}{2} (\zeta^\tau)^\top \cdot \zeta^\tau - V(\eta^\tau) \right] d\tau = \int_0^t \left[ (\zeta^\tau)^\top \cdot \zeta^\tau - V(\eta^0) \right] d\tau \\ &= \int_0^t (\zeta^\tau)^\top \cdot \zeta^\tau d\tau - V(\eta^0)t. \end{aligned} \quad (3.20)$$

The part of this expression pertinent to the dynamics within the subset of vibrational DOFs  $\mathcal{P}$  is then easily obtained by replacing  $\zeta^t$  with  $\pi \cdot \zeta^t$ , i.e.,

$$\int_0^t \mathcal{L}_{\text{eff}}^\tau d\tau \Big|_{\mathcal{P}} = \int_0^t (\pi \cdot \zeta^\tau)^\top \cdot (\pi \cdot \zeta^\tau) d\tau - V(\eta^0)t. \quad (3.21)$$

The term  $V(\eta^0)t$  generates an overall phase depending linearly on  $t$  and is responsible only for shift of the resulting spectrum without altering its shape.

### 3.4 Computational details

All *ab initio* calculations were performed with the Gaussian09 package.<sup>65</sup> Its output was extracted directly from the checkpoint file. The ground PES  $S_0$  was handled with the density functional theory (DFT), whereas the first excited singlet PES ( $S_1$ ) was described with the time-dependent DFT (TD-DFT). Following the work of Stendardo *et al.*,<sup>108</sup> our TD-DFT calculations were based on the long-range corrected CAM-B3LYP functional with 6-31+G(d,p) basis set. Within this TD-DFT setup, the energy gap between the  $S_0$  and  $S_1$  PESs of oligothiophenes is described quite accurately. Although Gaussian09 provides analytical gradients for both DFT and TD-DFT, analytical Hessians are available only for DFT. No symmetry constraints were enforced and the “fine” and “ultra fine” integration grids were used for OTF-AI calculations and geometry optimization, respectively.

In order to find the physically relevant equilibrium geometry of  $S_1$  for each oligothiophene  $T_n$ , we first performed an  $S_0$  geometry optimization of the “all-trans” conformer, the rings of which are oriented in an anti conformation with respect to their neighbors. The work by Becker and co-workers<sup>98</sup> suggests that this is the most stable conformer. The  $S_1$  geometry optimization was started from this  $S_0$  equilibrium geometry. It has been well-established that in contrast to the inter-ring twisted  $S_0$  equilibrium geometry



---

and its shallow potential,  $S_1$  exhibits a steep, deep, harmonic-like well in the vicinity of its planar equilibrium geometry.<sup>98, 130</sup> The  $S_1$  equilibrium geometry, served as the reference structure for the OTF-AI-TGA dynamics.

Within the OTF-AI-TGA, the GWP was propagated for the total time of 7976 a. u.  $\approx$  193 fs with a time step of 8 a. u.  $\approx$  0.2 fs using the second order symplectic algorithm. The resulting spectra were subjected to a phenomenological (inhomogeneous) Gaussian broadening with half-width at half-maximum (HWHM) of 0.025 eV  $\approx$  200  $\text{cm}^{-1}$ .

## 3.5 Results and discussion

### 3.5.1 Comparison with experimental spectra

Our results confirm the utility of the OTF-AI-TGA approach for electronic spectra calculation, since all important features of the experimental spectra are almost perfectly reproduced. Figure 7 demonstrates the agreement with the overall shape, peak intensities, as well as the trend of the spectra to gradually shift towards lower frequencies with increasing number of rings in the molecule. Note that particular experimental conditions, notably the interaction with the solvent (here, ethanol glass at 77 K), can produce a shift of the spectrum. However, we disregard this effect since the resulting shift is expected to be small for a broad class of solvents.<sup>98, 130-131</sup> Also, the exact prediction of the spectrum position is partly beyond the level of the *ab initio* setup employed here (see Sec. 3.4).

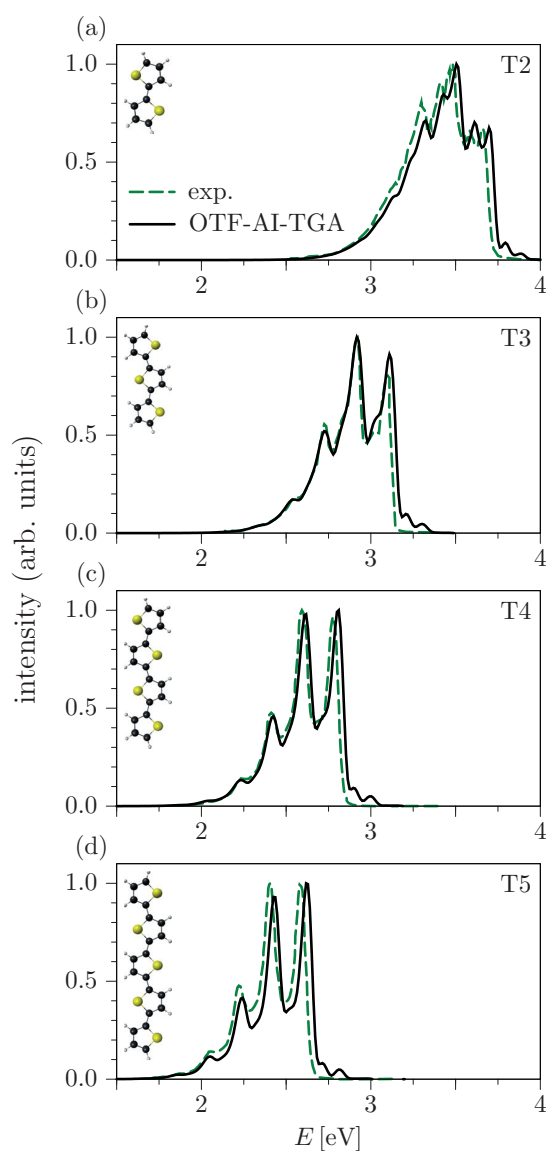


Figure 7: Emission spectra of the oligothiophene  $T_n$  family for: Comparison of experimental emission spectra (exp., dashed green line) with the full-dimensional OTF-AI-TGA calculations using all  $21n$  normal modes (solid black line).

Becker *et al.*<sup>132</sup> reported a significant red shift of the oligothiophene absorption spectra at low temperatures and attributed this phenomenon to the twisted $\rightarrow$ planar conformational transition induced by solvent freezing. Interestingly, this shift was not observed in the emission spectra, which suggests that in the whole temperature range it is only the planar conformation that plays a significant role in this process. Even without imposing explicit planarity constraints, no deviations from the planar conformation were observed during the ground-state gas-phase OTF-AI dynamics due to planarity of the initial geometry. This fact makes the comparison of our gas-phase results to the experimental

---

data more legitimate. Finally note that the *ab initio* ground state equilibrium geometry is twisted in contrast to the equilibrium geometry in ethanol glass at 77 K. Therefore, the  $n - 1$  torsional degrees of freedom connecting the planar and twisted geometries of  $Tn$  have imaginary frequencies. Since our approach is unable to describe wave-packet splitting, the TGA GWP only spreads along these degrees of freedom ( see Subsec. 3.5.5). However, since we are mainly interested in short-time dynamics, this behavior is qualitatively correct. Hence, the OTF-AI-TGA approach remains in this case robust even for floppy molecules and the question about the “harmonicity” of the system is of much lesser importance due to the employment of the local harmonic approximation. Although the global harmonic approximation is quite adequate for  $Tn$ ,<sup>108</sup> small changes of the peak positions and intensities can be observed as compared to OTF-AI-TGA (see Subsec. 3.5.6).

To facilitate comparison between line-shape spectra of oligothiophenes with different numbers of thiophene rings, the spectra shown in Figure 8(a) are first  $L^\infty$  normalized and subsequently shifted so that the “ $\alpha_0$ -peaks” overlap at zero energy. This reveals that the relative peak positions are rather insensitive to  $n$ , while their prominence is increasing with increasing  $n$ . The peak at the highest energy (in our notation:  $\alpha_0$ ) in the emission spectrum is attributed to the 0–0 transition.<sup>133</sup> The position of the  $\alpha_1$ -peak is close to the vertical transition energy  $E_{\text{vert}}$ , which, in loose terms, justifies its dominance in Figure 8(a). More detailed classification of individual spectral peaks into the  $\alpha, \beta$  groups and their interpretation from the dynamical viewpoint is discussed in Subsection 3.5.2.

It has been found experimentally that the 0–0 transition energy  $E_{0-0}$  in the polythiophene family  $Tn$  is a linear function of  $1/n$ .<sup>96-98, 101</sup> In accordance with this observation and our identification of  $E_{0-0}$  with  $E_{\alpha_0}$ , we found that  $E_{\alpha_0}$  is accurately described by the function  $E_{\alpha_0}(n) \approx (3.58/n + 1.91)$  eV. Good agreement with the experiment can be directly inferred from Figure 7. Furthermore, from the *ab initio* data, we determined in a similar fashion that  $E_{\text{vert}}(n) \approx (3.33/n + 1.77)$  eV. Fits of  $E_{\alpha_0}$ ,  $E_{\alpha_1}$  and  $E_{\text{vert}}$  are shown in Figure 8(b).

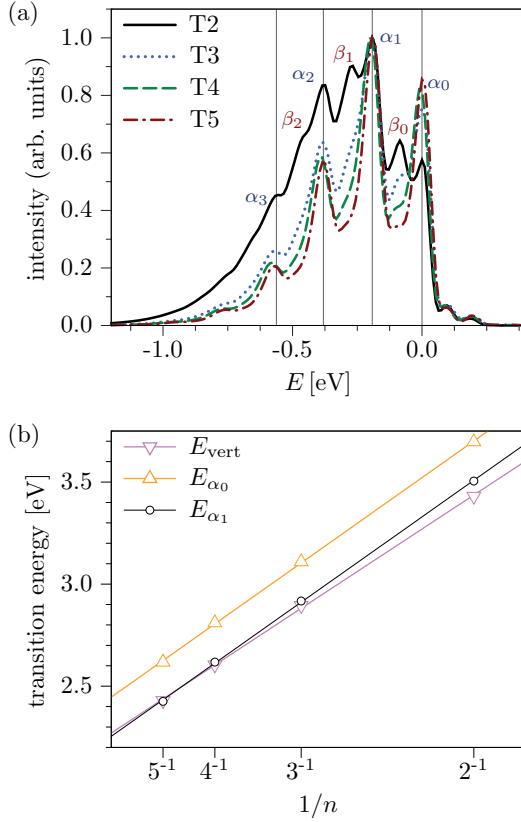


Figure 8: Emission in the oligothiophene  $T_n$  family for  $n \in \{2, 3, 4, 5\}$ . (a)  $L^\infty$ -normalized line-shape spectra. To facilitate their comparison, the spectra are shifted independently for each  $n$  so that the  $\alpha_0$  peak appears at zero energy. (b) Dependence of the vertical-transition energy  $E_{\text{vert}}$  and positions of the  $\alpha_0$  and  $\alpha_1$ -peaks ( $E_{\alpha_0}, E_{\alpha_1}$ ) on  $1/n$  (see text for details). Linear fits are denoted with lines.

Note that the relative intensity of the  $\alpha_0$ -peak, identified with the 0–0 transition, in Figure 8(a) increases with  $n$ . This can be related to the fact that the slope of  $E_{\alpha_1}(n)$  is larger than the slope of  $E_{\text{vert}}(n)$  [see Figure 8(b)], using the following heuristic argument: Neglecting the difference between the  $S_0$  and  $S_1$  zero-point energies, the 0–0 transition energy depends solely on the energy gap between these PESs. On the other hand,  $E_{\text{vert}}$  is influenced also by the relative displacement of the  $S_0$  and  $S_1$  potential minima. Therefore, if  $E_{\text{vert}}$  decreases more slowly with increasing  $n$  than does the 0–0 transition energy, one can expect a decrease not only in the energy gap between  $S_0$  and  $S_1$  PESs but also in the relative displacement of their minima, which, in turn, is responsible for the gain in intensity of the 0–0 transition, i.e., the  $\alpha_0$ -peak. This observation is in agreement with the Huang-Rhys analysis performed by A. Yang *et al.*<sup>96</sup> on fluorescence spectra of  $T_n$  for  $n \in \{3, 4, 5, 6\}$ .

---

### 3.5.2 Vibrational analysis

To gain a deeper understanding of the emission spectra shown in Figure 7 and Figure 8, we employ independently for each oligothiophene  $T_n$  the analysis proposed in Subsection 3.3.3 adapted to the normal-mode coordinates of the  $S_1$  PES of  $T_n$ . To this end, we closely follow the example presented at the end of Subsection 3.3.3. The normal-mode classification based on decompositions Eq. (3.14) with  $\varepsilon_B = 0.55$  and  $\varepsilon_Q = 0.6$  results for all  $T_n$  in an active space  $\mathcal{A}$  comprised of six groups of modes (see Table 3). This space is spanned by ten “active” modes (i.e.,  $|\mathcal{A}| = 10$ ) for T2-T4, while  $|\mathcal{A}| = 8$  for T5. The thresholds were chosen in order to obtain a minimal set  $\mathcal{A}$  of active modes with as many subsets as possible on condition that the reduced OTF-AI-TGA spectrum  $\sigma_{\mathcal{A}}$  recovers all important features of the “complete” spectrum  $\sigma_{\mathcal{D}}$ . For clarity, the subscript of  $\sigma$  denotes explicitly the set of modes taken into account in the spectra calculation. Formally, the spectrum  $\sigma_{\mathcal{A}}$  can be thought of as the computationally cheapest, yet still sufficiently accurate approximation of  $\sigma_{\mathcal{D}}$ .

For details regarding correlation function and spectra calculations within proper subspaces of  $\mathcal{D}$  we refer to the Subsection 3.3.4. From now on, to simplify notation, the implicit dependence of, e.g.,  $\mathcal{A}$  on the threshold values  $\varepsilon_B$  and  $\varepsilon_Q$  will not be denoted explicitly.

Figure 9(a) demonstrates that ten modes were sufficient to essentially reproduce the complete spectrum  $\sigma_{\mathcal{D}}$  for T2. The simplification achieved is the most striking for T5 [Figure 9(b)], for which eight modes were sufficient and hence the dimensionality was reduced more than ten times without losing any major feature in the spectrum. However, note that the “ $|\mathcal{A}|$ -mode” spectra in Figure 9 are slightly shifted due to dependence of the zero-point energy on the choice of  $\mathcal{A}$ .

The modes in  $\mathcal{A}$  are by definition considered to be coupled only within individual groups. Therefore, one can attempt to assign a characteristic vibrational movement of the entire molecule induced by excitation of the modes belonging to a particular group. Among the 24 groups ( $24 = 4$  oligothiophenes  $\times$  6 groups per oligothiophene), we identified 7 characteristic motions shown on the examples of T3 and T4 molecules in Figure 10. In Table 3, these characteristic motions are distinguished with a superscript.

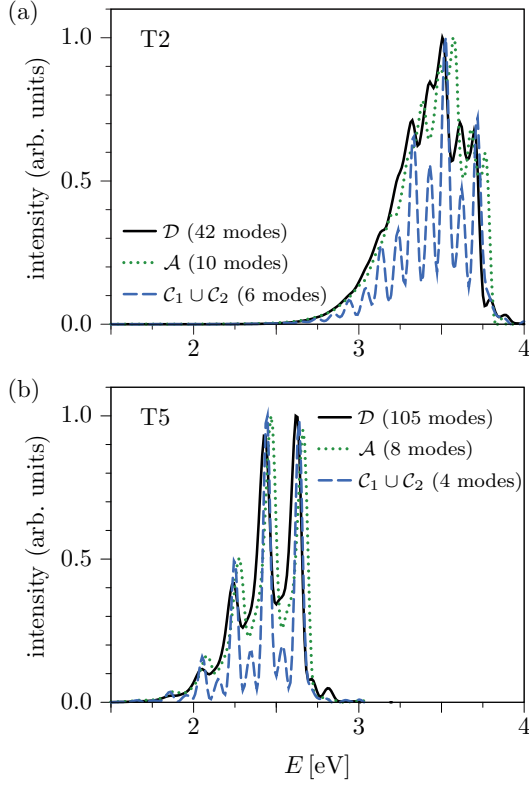


Figure 9: Emission spectra of oligothiophenes T2 (a) and T5 (b): comparison of the full-dimensional OTF-AI-TGA spectrum  $\sigma_{\mathcal{D}}$  (solid black line) with the spectrum  $\sigma_{\mathcal{A}}$  (dotted green line) computed within the subspace  $\mathcal{A}$  of the active modes and the spectrum  $\sigma_{\mathcal{C}_1 \cup \mathcal{C}_2}$  (dashed blue line) taking into account only modes belonging to the classes  $\mathcal{C}_1$  and  $\mathcal{C}_2$  (see Figure 11 and Table 3) introduced in Eq. (3.22).

Next, the six groups of normal modes are, for each  $n \in \{2, 3, 4, 5\}$ , merged into three disjoint classes  $\mathcal{C}_1$ ,  $\mathcal{C}_2$ , and  $\mathcal{C}_3$  as

$$\mathcal{C}_1 := \mathcal{A}_1, \mathcal{C}_2 := \mathcal{A}_2, \text{ and } \mathcal{C}_3 := \bigcup_{\alpha=3}^6 \mathcal{A}_\alpha. \quad (3.22)$$

The reason for introducing an additional logical layer is the observation in Figure 11 that the overall character of the spectrum  $\sigma_{\mathcal{C}_i}$  corresponding to the  $i$ th group is only mildly influenced by  $n$ , whereas the dependence on  $i$  is dominant. In loose terms, the first group  $\mathcal{C}_1$  comprises inter-ring stretch modes and is mainly reflected in the “ $\alpha$ -peaks” of the complete spectrum  $\sigma_{\mathcal{D}}$  [see Figure 8(a)]. The second group  $\mathcal{C}_2$  consists of a ring-squeeze mode and produces the “ $\beta$ -peaks” in Figure 8(a). Finally, the modes contained in the third group cause merely an overall broadening of the spectrum. Such a classification of vibrational modes, essential for a theoretical interpretation of the emis-

sion spectra, is also useful in practice, e.g., in the design of organic light-emitting diodes (OLEDs).<sup>134</sup>

The difference between individual classes is further emphasized by introducing an “overall relative displacement” of the  $i$ th class as  $R_i^2 := \sum_{j \in \mathcal{C}_i} \varrho_j^2$ . We have found that  $R_1$  is highly correlated with  $-n$  while  $R_2$  with  $1/n$ . Therefore, for low  $n$ , the dynamical importance of the class  $\mathcal{C}_2$  decreases faster with increasing  $n$ . This results in less structured spectra, shown in Figure 8(b), in which the  $\beta$ -peaks are almost invisible already for T3.

In summary, the inter-ring stretch motion is seen to have a dominant effect on the  $T_n$  spectra, especially for  $n > 2$ . Comparing the relative displacements of the classes  $\mathcal{C}_1$  and  $\mathcal{C}_2$  helps to further corroborate the hypothesis (stated above) that the  $S_0$  and  $S_1$  geometries become less displaced with increasing  $n$  since the 0–0 transition energy  $E_{0-0}(n)$  decreases faster than the vertical excitation energy  $E_{\text{vert}}(n)$ .

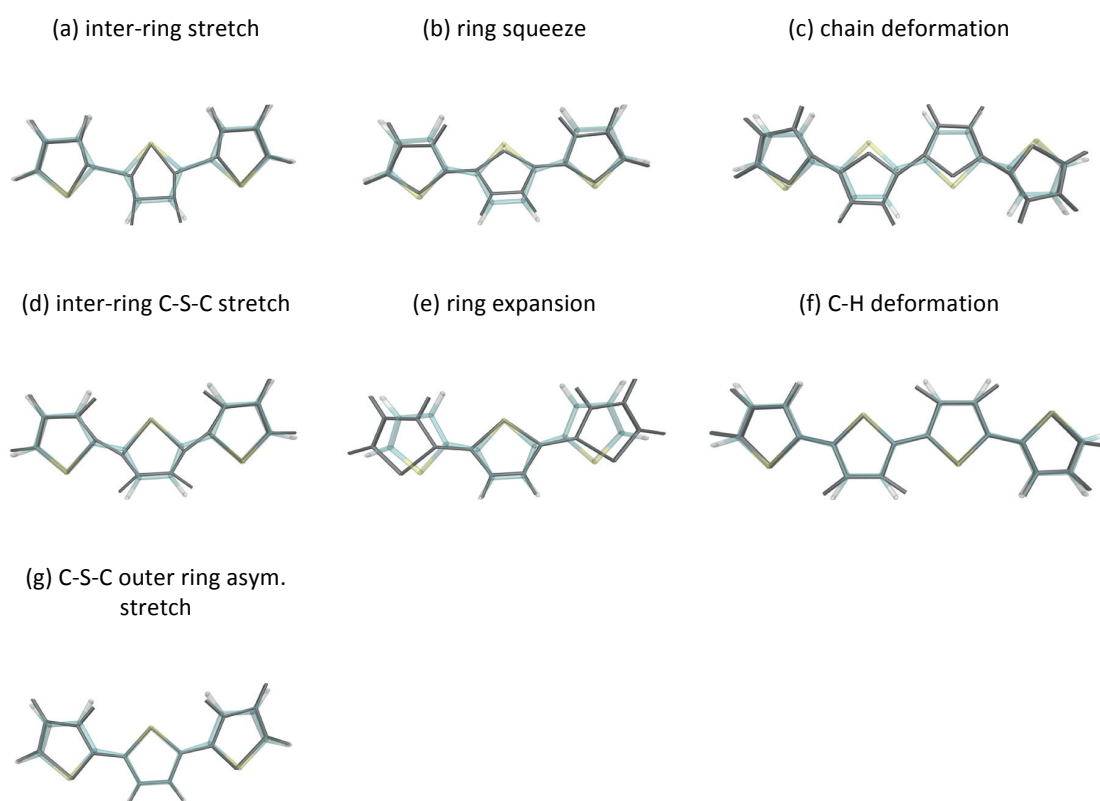


Figure 10: Characterization of the active normal modes in the set  $\mathcal{A} \subseteq \mathcal{D}$  [see Eqs. (3.14) and (3.22)] by the nature of the deformation which they exert on the oligothiophene  $T_n$  skeleton. To cover all cases presented in Table 3, these deformations are shown on the examples of T3 and T4. Panel labels correspond to the classification in Table 3.

Table 3: Normal-mode classification based on decompositions (3.14) and (3.22) with  $\varepsilon_B = 0.55$  and  $\varepsilon_Q = 0.6$  for the oligothiophene  $T_n$  family, Vibrational frequencies  $\omega_i$  are given in  $\text{cm}^{-1}$ , while the maximum relative displacements  $\rho_i$  of Eq. (3.11) are dimensionless. The modes are further classified into 7 groups by the character of the deformation which they exert on the oligothiophene skeleton. These groups are distinguished by superscript labels next to frequency values. For schematic depiction of these deformations see Figure 10.

class group	$\omega_i [\text{cm}^{-1}]$				$\rho_i$				
	T2	T3	T4	T5	T2	T3	T4	T5	
$\mathcal{C}_1$	$\mathcal{A}_1$	1657.7 <sup>(a)</sup>	1630.5 <sup>(a)</sup>	1615.5 <sup>(a)</sup>	1598.6 <sup>(a)</sup>	2.57 <sup>(a)</sup>	2.50 <sup>(a)</sup>	2.41 <sup>(a)</sup>	1.93 <sup>(a)</sup>
		1507.2 <sup>(a)</sup>	1553.9 <sup>(a)</sup>	1545.2 <sup>(a)</sup>	1590.1 <sup>(a)</sup>	1.23 <sup>(a)</sup>	1.10 <sup>(a)</sup>	1.12 <sup>(a)</sup>	1.35 <sup>(a)</sup>
		1450.0 <sup>(a)</sup>	1501.2 <sup>(a)</sup>	1581.3 <sup>(a)</sup>	1548.5 <sup>(a)</sup>	0.88 <sup>(a)</sup>	0.86 <sup>(a)</sup>	0.56 <sup>(a)</sup>	1.13 <sup>(a)</sup>
		1211.2 <sup>(a)</sup>	1461.9 <sup>(a)</sup>	1498.2 <sup>(a)</sup>		0.59 <sup>(a)</sup>	0.36 <sup>(a)</sup>	0.55 <sup>(a)</sup>	
		3243.6 <sup>(a)</sup>	1341.6 <sup>(a)</sup>	1462.6 <sup>(a)</sup>		0.25 <sup>(a)</sup>	0.34 <sup>(a)</sup>	0.36 <sup>(a)</sup>	
$\mathcal{C}_2$	$\mathcal{A}_2$	673.7 <sup>(b)</sup>	696.7 <sup>(b)</sup>	704.7 <sup>(b)</sup>	710.8 <sup>(b)</sup>	2.05 <sup>(b)</sup>	1.56 <sup>(b)</sup>	1.32 <sup>(b)</sup>	1.17 <sup>(b)</sup>
$\mathcal{C}_3$	$\mathcal{A}_3$	290.4 <sup>(e)</sup>	210.1 <sup>(e)</sup>	162.3 <sup>(e)</sup>	122.5 <sup>(c)</sup>	1.27 <sup>(e)</sup>	1.92 <sup>(e)</sup>	2.15 <sup>(e)</sup>	0.99 <sup>(e)</sup>
	$\mathcal{A}_4$	386.5 <sup>(c)</sup>	350.3 <sup>(c)</sup>	333.0 <sup>(c)</sup>	136.7 <sup>(c)</sup>	1.61 <sup>(c)</sup>	1.49 <sup>(c)</sup>	1.39 <sup>(c)</sup>	2.09 <sup>(c)</sup>
	$\mathcal{A}_5$	712.7 <sup>(g)</sup>	739.6 <sup>(g)</sup>	1112.9 <sup>(f)</sup>	322.6 <sup>(c)</sup>	1.09 <sup>(g)</sup>	0.64 <sup>(g)</sup>	0.63 <sup>(f)</sup>	1.35 <sup>(c)</sup>
	$\mathcal{A}_6$	1096.3 <sup>(f)</sup>	1261.6 <sup>(d)</sup>	1275.0 <sup>(d)</sup>	1109.5 <sup>(f)</sup>	0.78 <sup>(f)</sup>	0.70 <sup>(d)</sup>	0.66 <sup>(d)</sup>	0.78 <sup>(f)</sup>

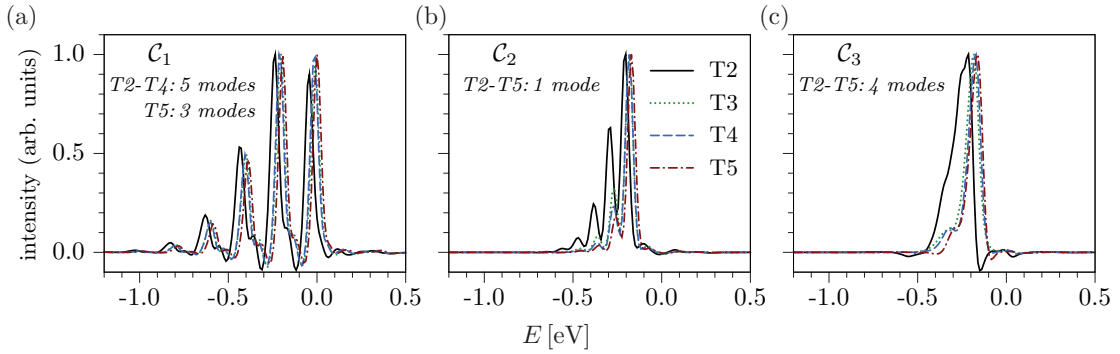


Figure 11: Classification of normal modes of the oligothiophene  $T_n$  family according to their influence on the resulting emission spectrum see Eqs. (3.14) and (3.22)]. Detailed description of individual classes is contained in Table 3. (a) Inter-ring stretch modes responsible for the  $\alpha$ -peaks shown in Figure 8. (b) Ring-squeeze mode reflected in the  $\beta$ -peaks in Figure 8. (c) Remaining modes causing overall broadening of the spectra



### 3.5.3 Quinoid structure of $S_1$

The extent of  $\pi$ -conjugation along the oligomer chain is reflected in the quinoid structure of individual rings. The degree of the quinoid/aromatic character of the  $i$ th ring in  $T_n$  can be quantified in terms of the so-called *bond length alternation*<sup>135-137</sup> (BLA)

$$BLA_i = R_{\beta_i} - (R_{\alpha_i} + R_{\alpha'_i}) / 2, \quad (3.23)$$

where  $R$  denotes the length of the  $\beta$ ,  $\alpha$ , and  $\alpha'$  bonds of the  $i$ th ring (see Figure 12). Hence, quinoid rings have a negative BLA, while aromatic rings have a positive BLA.

The  $S_1$  equilibrium geometries of  $T_n$  in Figure 12 reveal that for  $n > 2$ , both quinoid and aromatic ring types are present in the chain: The inner rings are quinoid, while the end rings are aromatic. On the other hand, both rings of  $T_2$  have quinoid character. However, the large difference between the lengths of  $\alpha$  and  $\alpha'$  bonds suggests a double-bond character of the outer  $\alpha$  bond in  $T_2$ . In general, the DFT  $S_1$  geometries exhibit more pronounced quinoid character in comparison with the  $S_1$  geometries calculated at the MNDO level,<sup>137</sup> which describe  $T_2$  as slightly aromatic.

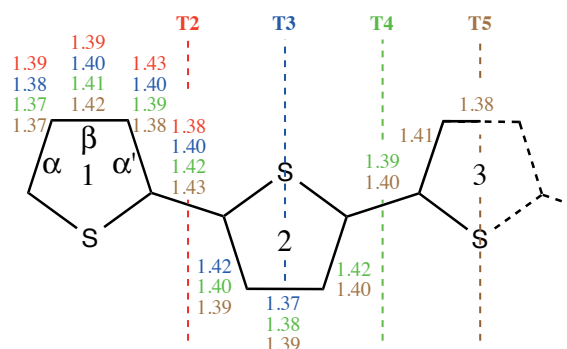


Figure 12: Equilibrium  $S_1$  geometry of oligothiophenes  $T_n$  family. Corresponding bond lengths for different oligothiophenes  $T_n$  are juxtaposed with each other next to individual bonds, whereas the dashed lines represent the end of the half-chain for each  $T_n$ . E.g., to the right of the dashed line marked as  $T_3$  there are only one or two bond-length values since those bonds are not present in the half-chain of  $T_2$  and  $T_3$ .

The time dependence of BLA, displayed for  $T_5$  in Figure 13 shows emission-induced oscillations between the quinoid and aromatic characters of individual rings. The inner rings are seen to be subjected to larger structural variations, while the outer rings remain aromatic, although the degree of aromaticity changes periodically. Hence, the quinoid

character of  $Tn$  in  $S_1$  is well localized over just 2-3 rings, as was shown also by Beljonne *et al.*,<sup>137</sup> while the emission process triggers deformation of the whole chain.

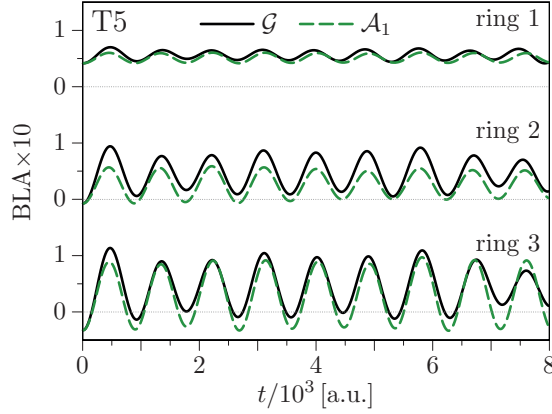


Figure 13: Time dependence of the bond length alternation (BLA) parameter during the dynamics induced by the emission in pentathiophene T5 [see Eq. (3.23) and Figure 12]. The character of the outer rings (rings 1 and 2) is mainly aromatic (positive BLA), while the transition to the quinoid structure (negative BLA) occurs almost exclusively within the inner ring (ring 3).

### 3.5.4 Analysis of the effective conjugation coordinate

Oligomer spectra are usually analyzed in terms of the so-called *effective conjugation coordinate*<sup>138-140</sup> (ECC), i.e., the totally symmetric internal coordinate the excitation of which triggers the conformational change between the aromatic to the quinoid structures of the molecule. This approach is especially popular within Raman spectroscopy.<sup>136, 141-144</sup> For the oligothiophene family  $Tn$ , ECC captures the alternation between adjacent bonds and is defined as

$$\mathcal{R} := \frac{1}{\sqrt{\bar{N}}} \sum_{a=1}^{\bar{N}} (-1)^{a-1} r_a, \quad (3.24)$$

where  $r_a$  is the Cartesian vector connecting the  $a$ th and  $(a + 1)$ th carbon atoms of the backbone comprised of  $\bar{N} = 4n - 1$  C-C bonds in total. Further insight is gained by restating Eq. (3.24) in the normal-mode coordinates. By employing transformation (1.38), we obtain

$$\mathcal{R} = \mathcal{R}_{\text{ref}} + \mathbf{R} \cdot \boldsymbol{\eta}, \quad \text{with } \mathbf{R} := \mathbf{S} \cdot \mathbf{T} \text{ and } \mathcal{R}_{\text{ref}} := \mathbf{S} \cdot \boldsymbol{\xi}_{\text{ref}}, \quad (3.25)$$

where  $\mathbf{T}$  is the transformation matrix of Eq. (1.38),  $\boldsymbol{\xi}_{\text{ref}}$  denotes Cartesian coordinates of a reference geometry, and

---


$$S := \frac{1}{\sqrt{N}} \sum_{a=1}^{\bar{N}} (-1)^a (P_a - P_{a+1}) \quad (3.26)$$

is a generalization of the projector  $P_b$  defined below Eq. (1.39).

Then, the normalized “coupling strength”  $v^j$  of the  $j$ th normal mode to  $\mathcal{R}$  reads

$$v^j := \frac{\text{Tr} Y_j^T \cdot R^T \cdot R \cdot Y_j}{\text{Tr} R^T \cdot R}, \quad (3.27)$$

where the square matrix  $Y_j$  is defined as  $(Y_j)_{kl} := \delta_{jk} \delta_{jl}$ .

However, the quantity  $\mathcal{R}$  changes during the dynamics and its variations are described in terms of

$$\delta \mathcal{R}^t := \mathcal{R}^t - \mathcal{R}^0 = R \cdot \bar{\eta}^t, \text{ with } \bar{\eta}^t := (\eta^t - \eta^0). \quad (3.28)$$

Now, in order to assess the importance of a particular normal mode with respect to  $\delta \mathcal{R}^t$ , we cannot use Eq. (3.27) directly, since  $v^j$  provides only a static picture. To remedy this, we introduce a more appropriate measure of dynamical coupling:

$$v^j := \frac{\zeta^j}{\sum_k \zeta^k}, \text{ with } \zeta^j := \int_0^t dt \bar{\eta}^t \cdot Y_j^T \cdot R^T \cdot R \cdot Y_j \cdot \bar{\eta}^t, \quad (3.29)$$

where the summation runs over all normal modes.

A comparison of individual normal modes for  $Tn$ ,  $n \in \{2, 3, 4, 5\}$ , in terms of  $v^j$  and  $v^j$  is shown in Figure 14, which demonstrates clearly that only certain modes contributing to  $\mathcal{R}$  are excited during the fluorescence process. This means that an analysis based merely on  $v^j$  would be incomplete.

In Subsection 3.3.3, individual normal modes were classified into independent groups  $\mathcal{A}_i$  [see Eq. (3.14)]. Using Eq. (3.29), we can estimate the dynamical influence of a particular group  $\mathcal{A}_i$  on  $\delta \mathcal{R}^t$  by employing

$$\kappa_i := \sum_{j \in \mathcal{A}_i} v^j. \quad (3.30)$$

Table 4 demonstrates that variations in  $\mathcal{R}$  can be assigned mostly to the group  $\mathcal{A}_1$ , and, hence, the  $\alpha$ -peaks [see Figure 8(a)] originate from the change of the ECC during the dynamics induced by the fluorescence process.

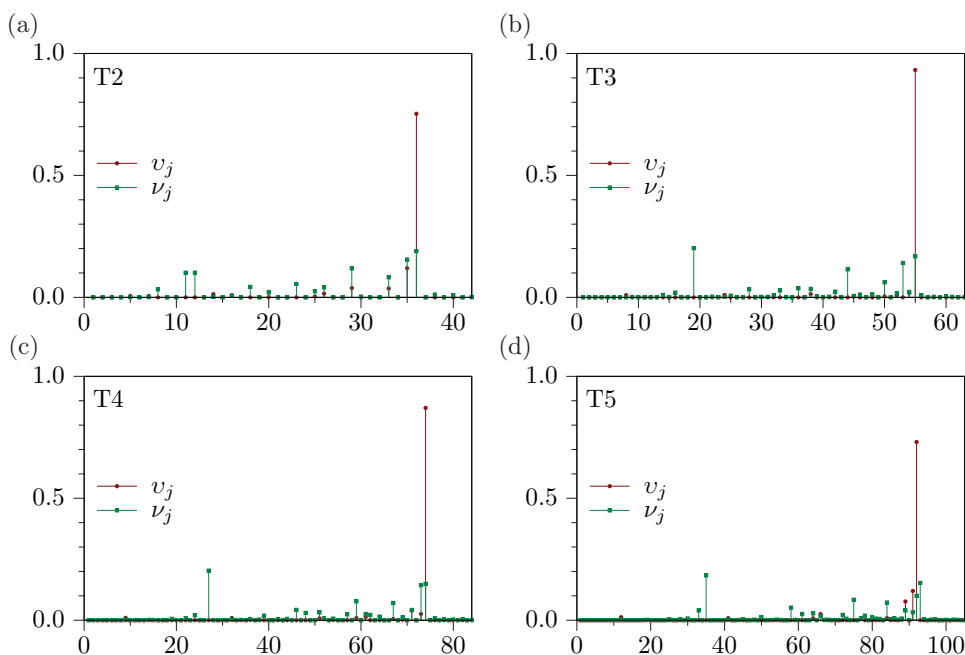


Figure 14: Comparison of the static,  $\nu_j$  [see Eq. (3.27)], and dynamic,  $v_j$  [see Eq. (3.29)], contribution of individual normal modes to the ECC  $\mathcal{R}$  of Eq. (3.24) for the oligothiophenes  $T_n$ ,  $n \in \{2, 3, 4, 5\}$

Table 4: Contribution of the  $i$ th group  $\mathcal{A}_i$  to ECC in terms of  $\kappa_i$  introduced in Eq. (3.30).

	$\mathcal{A}_1$	$\mathcal{A}_2$	$\mathcal{A}_3$	$\mathcal{A}_4$	$\mathcal{A}_5$	$\mathcal{A}_6$
T2	0.947	0.013	0.006	0.006	0.008	0.015
T3	0.962	0.010	0.009	0.001	0.000	0.003
T4	0.942	0.009	0.010	0.002	0.004	0.013
T5	0.927	0.008	0.000	0.012	0.001	0.025

In summary, Oligomer vibrational line shapes are usually analyzed in terms of the effective conjugation coordinate<sup>138-140</sup> (ECC)—a totally symmetric internal coordinate describing the variation of adjacent C-C backbone stretches, responsible for the change from the aromatic to quinoid structure. A detailed analysis of the dynamics shows that only some of the modes coupled to ECC are also excited by the fluorescence process. The overall contribution of the  $\mathcal{A}_1$  group to the ECC is more than 92% for all oligothiophenes and, hence, the  $\alpha$ -peaks originate from the change of the ECC during the dynamics induced by the fluorescence process.

---

### 3.5.5 Time dependence of the width matrix of the OTF-AI-TGA GWP

In floppy molecules, torsional degrees of freedom are typically associated with a potential of mild double-well character. In the electronic ground state of oligothiophene  $T_n$ , the  $n - 1$  floppy inter-ring torsional modes connect the twisted geometries through a planar “transition” geometry. An initial nuclear wave packet located at this planar “transition” geometry then splits into two parts moving towards the local minima. Obviously, a single-classical- trajectory approach such as OTF-AI-TGA can capture this behavior “only” qualitatively: the TGA GWP spreads along these torsional degrees of freedom (see Figure 15). This effect in turn causes damping of the correlation function and, hence, broadening of the resulting spectrum. Since these torsional degrees of freedom are usually low-frequency modes, they are less important in short-time dynamics. Note, that the OTF-AI-TGA is still robust even in this worst-case scenario and, should the need arise, the analysis of the TGA GWP width evolution in combination with the analysis techniques presented in Subsection 3.3.3 allows to identify these particular degrees of freedom so that they can be treated by more adequate methods.

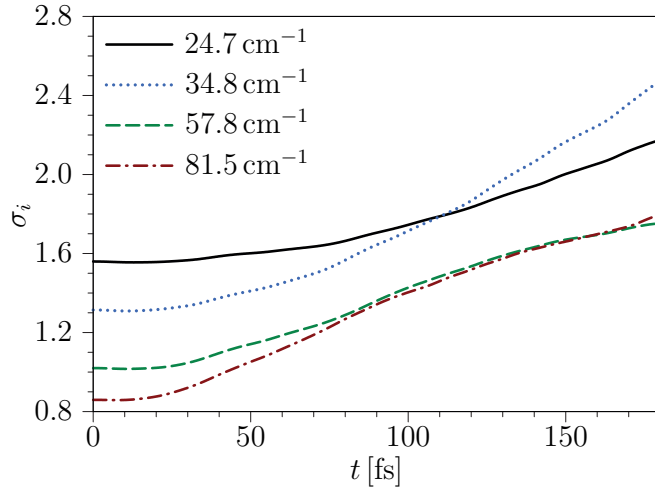


Figure 15: Time dependence of the Gaussian “nuclear-density” width  $\sigma_i(t) = (4\text{Re}A_{ii}^t)^{-1/2}$  along the  $i$ th mode in oligothiophenes T5. The quantity  $\sigma_i$  is shown for the four different modes in which the spreading of the GWP is most pronounced.

### 3.5.6 Comparison of the OTF-AI-TGA approach to the global harmonic approximation

A natural question in connection with the OTF-AI-TGA approach in our setting is whether and possibly to what extent does the popular global harmonic approximation (HA) of the PESs capture all important features of the emission spectrum in the oli-

---

gothiophene  $T_n$  family. Figure 16 provides direct answer. There we see that the agreement of HA with OTF-AI-TGA is quite good and that this agreement further improves with increasing  $n$  in accordance with the heuristic arguments provided in Subsection 3.5.1. The OTF-AI-TGA spectrum of T2 reproduces relative intensities of individual peaks better than the HA spectrum while the spectra of T5 are almost identical.

However, the HA method is in our context plagued with one major obstacle, namely the choice of the reference structure of  $S_0$ . We consider two different choices: the “ $S_0$  twisted” model is based on the ground-state twisted ab initio equilibrium (i.e., global minimum) geometry, while the “ $S_0$  planar” employs planar geometry obtained with constrained optimization. The planar  $S_0$  structure of  $T_n$  does not correspond to a local potential minimum since there are  $n - 1$  imaginary frequencies attributed to the  $n - 1$  torsional modes. In the calculations presented in Figure 16, these imaginary frequencies are projected out. For  $T_n$ , this leads thus to a harmonic  $20n + 1 = 3N(n) - 6 - (n - 1)$  dimensional model [see Eq. (3.15)] which is exactly solvable with TGA. Figure 16(a) shows that the choice of the reference structure is of paramount importance: The agreement of “ $S_0$  twisted” with OTF-AI-TGA and/or experimental data is rather poor.

In contrast to the HA, OTF-AI-TGA does not require an a priori knowledge of the landscape of the ground PES and thus in this sense provides a more robust tool for calculation of emission spectra in large molecules.

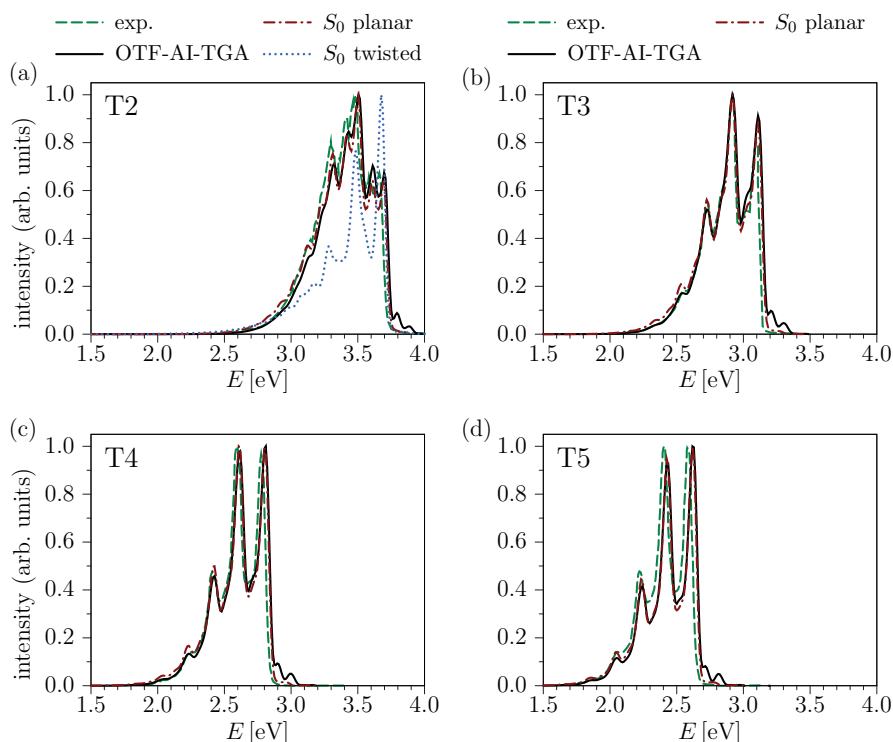


Figure 16: Emission spectra of the oligothiophenes  $T_n$  family: Comparison of global harmonic approximation (“ $S_0$  planar” and “ $S_0$  twisted”) to the OTF-AI-TGA approach and the experimental data. The “ $S_0$  twisted” case is shown only for T2.

### 3.6 Conclusion

All features of the experimental emission spectra of oligothiophenes with up to five rings (i.e., up to 105 vibrational DOFs) are well reproduced by our OTF-AI-TGA calculations. The efficiency of the TGA formulation is found to allow treating all vibrational DOFs on an equal footing even in case of larger systems especially since the OTF-AI scheme does not require an a priori knowledge of the potential energy surfaces and the TGA approach remains robust for floppy molecules. No symmetry considerations are necessary; in particular, neither the dynamics nor the analysis relies on any symmetry assumptions. Moreover, further considerable gain in efficiency without losing any substantial information can be obtained by employing Hessian interpolation.

Experimentalists try, often successfully, to translate the spectral features into a dynamical picture, which for theoreticians is often the starting point. The extraction of the essential information from the dynamical simulation, however, is often as difficult as the

---

simulation itself. We presented, therefore, a novel systematic approach to identify groups of vibrations that are essential for the dynamics and for the spectrum. This approach even allowed us to compare different oligothiophenes  $T_n$  and to study changes in their spectra with increasing  $n$ : Their vibrational line shapes are modulated by interring stretch and ring-squeeze vibrations, the latter contributing to the spectral broadening for longer chains. The ground and excited potential energy surfaces become more similar as the chain length increases; this, in turn, reduces the amplitude of the dynamics induced by emission and results in a shift of the intensity toward the 0–0 transition. The phenomenon is also reflected in the different dependences of the 0–0 and vertical transition energies on  $1/n$ .

The OTF-AI-TGA scheme also allowed us, by evaluating the bond length alternation, to study directly dynamical oscillations between the quinoid and aromatic characters of individual rings in the oligothiophene chain.

OTF-AI-TGA is also useful as a preliminary test. The expensive OTF-AI information stored during the TGA simulation can be reused in other semiclassical methods such as poor person’s Herman-Kluk (HK) propagator, where the HK prefactor is for all contributing trajectories assumed to be equal to the prefactor of the central trajectory.<sup>12</sup> In systems, which are too large to be treated with a more sophisticated quantum or semiclassical method, but for which the TGA is insufficient, e.g., due to the importance of interference effects, the analysis of the OTF-AI-TGA results can be used to define a subspace of reduced dimensionality, in which the most important dynamics occurs. Within this subspace, the effects that cannot be described with the TGA may be studied with less efficient yet better-suited methods.<sup>145</sup> Alternative approaches for constructing the information-flow matrix in order to maximize the decoupling of the DOFs with minimal impact on the resulting spectrum are the subject of our ongoing research.

Finally, let us note that the computational protocol presented here is not limited to linear spectroscopy; nonlinear spectra such as time-resolved stimulated emission can also be evaluated with the OTF-AI-TGA.



---

## Chapter 4 On-the-fly *ab initio* semiclassical dynamics of floppy molecules: Absorption and photoelectron spectra of ammonia

Because oligothiophenes are rather harmonic, we next studied how OTF-AI-TGA performs in situations where large amplitude anharmonic motions are crucial for spectra calculations. Therefore, we computed the absorption and photoelectron spectra of  $\text{NH}_3$ , which depends strongly on the well-known umbrella motion. The content of this chapter has been published in the *Journal of Physical Chemistry A*.<sup>146</sup>

### 4.1 Abstract

We investigate the performance of on-the-fly *ab initio* (OTF-AI) semiclassical dynamics combined with the thawed Gaussian approximation (TGA) for computing vibrationally resolved absorption and photoelectron spectra. Ammonia is used as a prototype of floppy molecules, whose potential energy surfaces display strong anharmonicity. We show that despite complications due to the presence of large amplitude motion, the main features of the spectra are captured by the OTF-AI-TGA, which—by definition—does not require any *a priori* knowledge of the potential energy surface. Moreover, the computed spectra are significantly better than those based on the popular global harmonic approximation. Finally, we probe the limit of the TGA to describe higher-resolution spectra, where long time dynamics is required.

---

## 4.2 Introduction

*Ab initio* semiclassical methods have proven to provide a powerful tool for decoding molecular spectra:<sup>4, 19, 109-110, 113, 147-149</sup> Not only do the classical trajectories underlying such methods help visualize the relevant physical and chemical processes, but, in contrast to popular *ab initio* classical molecular dynamics, nuclear quantum effects are taken into account at least approximately. Since the propagation requires only a local knowledge of the potential energy surface (PES), an on-the-fly *ab initio* (OTF-AI) scheme (see Subsection 1.5.1) can be applied, circumventing the construction of global PESs. The overall cost, however, limits almost all semiclassical methods to small systems.

Challenged by this limitation, we showed on the example of oligothiophenes that the efficiency of Heller’s thawed Gaussian approximation (TGA) (see Ref. [50] or Section 1.4) combined with the OTF-AI scheme permits calculating vibrationally resolved spectra of large systems with up to 105 degrees of freedom (DOFs) (see Chapter 3). Furthermore, we showed that this OTF-AI-TGA can sometimes capture qualitatively the effect of transitions to PESs with a double-well character, such as in the emission spectra of oligothiophenes the equilibrium geometries of which are twisted in the ground state and planar in the excited state. Within the OTF-AI-TGA, the nuclear vibrational wave function is described by a single Gaussian wave packet (GWP) whose time-dependent width is propagated using the local harmonic approximation of the PES (see Sections 1.4 and 1.5). Since the short-time dynamics is often well described by a thawed GWP, the OTF-AI-TGA has been developed with the purpose of computing broad vibronic spectra.

Here, we focus on how the OTF-AI-TGA performs on floppy molecules, the spectra of which depend strongly on large amplitude motions, and hope to find an improvement over the standard approach based on the more drastic, global harmonic approximation for the PESs. When the vibronic spectra of floppy molecules are calculated within the global harmonic approximation,<sup>104, 106-107, 150-154</sup> the choices of the coordinate system and reference structures are crucial. Furthermore, to produce satisfactory results, the global harmonic approximation often had to be combined with anharmonic potentials for the floppy DOFs,<sup>152, 155</sup> requiring a preliminary exploration of the PESs, which is rather cumbersome if not impossible for larger molecules. In contrast, the OTF-AI-TGA completely avoids this “prescreening” and treats all DOFs on an equal footing; yet, the anharmonicity is captured partially, and, if needed, the PES can be studied afterwards by extracting the most important DOFs using, e.g., the approach described in Subsection 3.3.3.

---

We use ammonia (NH<sub>3</sub>) as a prototype of a floppy molecule, on which, due to its small size, different and rather accurate levels of theory for the OTF-AI scheme can be compared, permitting to separate the errors due to electronic structure evaluation from those due to the dynamical approximation. The  $\tilde{A} \ ^1A_2'' \leftarrow \tilde{X} \ ^1A_1'$  ( $S_1 \leftarrow S_0$ ) absorption spectrum of ammonia is dominated by a long progression resulting from the activation of its well-known umbrella vibration,<sup>156-158</sup> along which the PES of the  $\tilde{X} \ ^1A_1'$  state has a shape of a double well with two degenerate minima with pyramidal geometry of C<sub>3v</sub> symmetry. In contrast, the trigonal planar equilibrium configuration of the  $\tilde{A} \ ^1A_2''$  excited state belongs to the D<sub>3h</sub> point group. Such a non-planar to planar electronic transition involves a substantial displacement between equilibria and, as a result, induces a large-amplitude nuclear motion exploring anharmonic regions of the excited PES. The spectral broadening is caused by the short lifetime of the  $\tilde{A}$  state, which has been assigned to strong pre-dissociation.<sup>159-160</sup> While we do not explore it here, the photodissociation of NH<sub>3</sub> due to the quasi-bound nature of the Franck-Condon region of  $\tilde{A}$  and its influence on the diffuse character of the spectrum have been studied by full-dimensional nonadiabatic quantum dynamics calculations.<sup>161-165</sup>

We also probe the limits of the OTF-AI-TGA's capability to describe long-time propagation required for higher-resolution vibronic spectra such as the  $\tilde{X} \ ^2A_2'' \leftarrow \tilde{X} \ ^1A_1'$  photoelectron spectrum of NH<sub>3</sub>  $\rightarrow$  NH<sub>3</sub><sup>+</sup> + e<sup>-</sup> that shows both a strong and weak progressions (see Edvardsson *et al.*<sup>166</sup> and references therein), and has served as a benchmark for spectra calculations of floppy molecules.<sup>152, 155</sup> The relevant dynamics is similar to the dynamics responsible for the absorption spectrum: The equilibrium geometry of the ionic ground state is also planar with D<sub>3h</sub> symmetry and the main vibration induced by the excitation is the umbrella motion resulting in a long, intense progression. In contrast to the absorption spectrum, however, another, weak progression appears. Theoretical studies using the multiconfiguration time-dependent Hartree (MCTDH) quantum dynamics method combined with high-level *ab initio* PESs<sup>167-169</sup> assigned this weak progression to the totally symmetric stretching motions.<sup>167-168</sup>

Our OTF-AI-TGA calculations of absorption and photoelectron spectra are compared with different global harmonic models in order to evaluate the effect of the global harmonic approximation on the peak spacing and progressions appearing in the spectra. Experimental absorption and photoelectron spectra serve as benchmarks.

---

## 4.3 Theory

### 4.3.1 Absorption and photoelectron spectra calculations

According to Section 1.2 [Eq. (1.19)], the spectrum is obtained, using the electric-dipole approximation, time-dependent perturbation theory, and Condon approximation, as the Fourier transform

$$\sigma(\omega) = \frac{2\pi}{3\hbar c} |\mu_{ge}|^2 \omega \int C_{\mu}(t) e^{i t(\omega + E_0/\hbar)} \quad (4.1)$$

of the autocorrelation function

$$C(t) = \langle \psi_{\text{init}} | e^{-i\hat{H}_e t/\hbar} | \psi_{\text{init}} \rangle, \quad (4.1)$$

the shape of which is modulated by the nuclear motion induced by the electronic excitation. The initial nuclear state  $\psi_{\text{init}}$ , stationary in the ground electronic state with energy  $E_0$ , starts to evolve with the excited-state Hamiltonian  $\hat{H}_e$  after excitation. Whereas the  $\text{NH}_3$  absorption spectrum arises from the light-induced nuclear motion on the  $\tilde{A} \ ^1A_2''$  electronic surface, the photoelectron spectrum is determined by the nuclear motion on the cationic surface  $\tilde{X} \ ^2A_2''$  generated by the ejection of an electron from the neutral molecule.

### 4.3.2 Global harmonic potential construction

When computing vibronic spectra, it is popular to approximate the relevant PESs globally by multidimensional harmonic oscillators; we refer to this as the global harmonic approximation and will show its limitations below. The reason for the widespread use of the global harmonic approximation is the existence of efficient exact algorithms allowing the treatment of even large molecules in this setting.<sup>104, 170-171</sup> However, one can also (and we do) evaluate the global harmonic spectra with the TGA since it, too, is exact in globally quadratic PESs.

The harmonic model for the PES  $i$  expressed in vibrational normal mode coordinates about the reference geometry  $\xi_{\text{ref}}$  has the general form

$$V_i(q) = V_{0,i} + \frac{1}{2} (q - d_i)^T \cdot K_i \cdot (q - d_i), \quad (4.2)$$

with a minimum  $V_{0,i}$  at position  $d_i$  and the force matrix  $K_i$  given by

$$\begin{aligned}
V_{0,i} &= V_i|_{q_i} - E_{\text{rea}} \\
d_i &= -K_i^{-1} \cdot \text{grad}_q V_i|_{q_i} + q_i \\
K_i &= \text{Hess}_q V_i|_{q_i},
\end{aligned} \tag{4.3}$$

where the energy  $V_i|_{q_i}$ , gradient  $\text{grad}_q V_i|_{q_i}$ , and Hessian  $\text{Hess}_q V_i|_{q_i}$  are the results of *ab initio* calculations at geometry  $\xi_i$  and transformed into normal mode coordinates  $q_i$  using Equations (1.40), (1.42), and (1.43). Finally,  $E_{\text{rea}} = \frac{1}{2} (d_i - q_i)^T \cdot K_i \cdot (d_i - q_i)$  is the rearrangement energy.

The global harmonic models are usually based on the following choices for  $\xi_{\text{ref}}$  and  $\xi_i$ .<sup>104, 107</sup> In the ground state global harmonic approximation,  $K_g$  is diagonal and  $d_g = \vec{0}$  since the ground state equilibrium geometry serves as a reference state ( $\xi_{\text{ref}} = \xi_g$ ). As for the excited state, there are two natural yet different choices for the harmonic PES: The adiabatic harmonic PES corresponds to *ab initio* data computed at the excited state equilibrium geometry  $\xi_e$ , whereas the vertical harmonic PES is constructed using *ab initio* data evaluated on the excited state at the ground state equilibrium geometry  $\xi_g$ . We constructed all three harmonic PESs; all of them had only real frequencies.

### 4.3.3 Derivation of the TGA Gaussian wave packet energy

The key ingredient of OTF-AI-TGA, the methods used here to calculate the spectra, is the *local harmonic approximation* (see Section 1.4). This approximation results in a time-dependent effective potential [Eq. (1.26)] and, therefore, the total GWP energy  $E_{\text{GWP}} = \langle \psi_{\text{GWP}} | \hat{V} + \hat{T} | \psi_{\text{GWP}} \rangle$  is not conserved. We follow the strategy used for Gaussian basis set methods<sup>48</sup> to derive an explicit expression for  $E_{\text{GWP}}$ , which is then used in Subsection 4.5.2 to analyse the limit of the TGA to describe higher-resolution spectra, where long time dynamics is required.

In the derivation, we will use the following three basic Gaussian integrals:

$$\begin{aligned}
I_0(\Sigma) &:= \int d^D q e^{-q^T \cdot \Sigma \cdot q} = \left( \frac{\pi^D}{\det \Sigma} \right) \\
I_1(\Sigma, b) &:= \int d^D q (b^T \cdot q) e^{-q^T \cdot \Sigma \cdot q} = 0 \\
I_2(\Sigma, \kappa) &:= \int d^D q (q^T \cdot \kappa \cdot q) e^{-q^T \cdot \Sigma \cdot q} = \frac{1}{2} I_0(\Sigma) \text{Tr}(\kappa \cdot \Sigma^{-1})
\end{aligned} \tag{4.4}$$

where  $\Sigma$  and  $\kappa$  are  $D \times D$  positive definite symmetric complex matrices and  $b$  denotes a  $D$ -dimensional complex vector.

The expectation value of the kinetic operator in the GWP state is

$$\langle \hat{T} \rangle^t = \frac{\hbar^2}{2} \int dq (\text{grad}_q \psi^t)^\dagger \cdot G^{-1} \cdot (\text{grad}_q \psi^t), \quad (4.5)$$

where  $G$  denotes the mass matrix ( $G$  is simply the identity matrix in mass-scaled coordinates, but we keep a general  $G$  here since the calculations are not more difficult) and the gradient of the normalized GWP [Eq. (1.25)] is given by

$$\text{grad}_q \psi^t = \psi^t \left\{ -2A^t(q - q^t) + \frac{i}{\hbar} p^t \right\}. \quad (4.6)$$

Using the Gaussian integrals from Eq. (4.4) and separating the total kinetic energy  $\langle \hat{T} \rangle^t = E_{\text{cl,kin}}^t + E_{\text{sc,kin}}^t$  into a ‘‘classical’’ (cl) kinetic energy of the central trajectory and a ‘‘semiclassical’’ (sc) contribution due to the width of the wavepacket, we can write:

$$\begin{aligned} E_{\text{cl,kin}}^t &= \frac{1}{2} (p^t)^T \cdot G^{-1} \cdot p^t \\ E_{\text{sc,kin}}^t &= \frac{1}{2} \hbar^2 \text{Tr} \left[ G^{-1} (A^t)^* (\text{Re } A^t)^{-1} A^t \right]. \end{aligned} \quad (4.7)$$

Since the effective potential  $V_{\text{eff}}^t(q)$  [Eq. (1.26)] is expanded to the second order due to the local harmonic approximation we can use the same strategy to evaluate the expectation value of the potential operator

$$\langle \hat{V} \rangle^t = \int dq (\psi^t)^* \cdot V_{\text{eff}}^t \cdot \psi^t. \quad (4.8)$$

Applying the Gaussian integrals [Eq. (4.4)] and separating the potential energy into classical and semiclassical contributions, we can write

$$\begin{aligned} E_{\text{cl,pot}}^t &= V|_{q^t} \\ E_{\text{sc,pot}}^t &= \frac{1}{4} \text{Tr} \left[ \text{Hess}_q V|_{q^t} \cdot (2 \text{Re } A^t)^{-1} \right]. \end{aligned} \quad (4.9)$$

The same separation can be applied to the total energy of the wave packet,  $E_{\text{GWP}}^t = E_{\text{cl}} + E_{\text{sc}}^t$ , where  $E_{\text{cl}} = E_{\text{cl,pot}}^t + E_{\text{cl,kin}}^t$  corresponds to the total classical energy of the central trajectory, whereas the total semiclassical energy  $E_{\text{sc}}^t = E_{\text{sc,pot}}^t + E_{\text{sc,kin}}^t$  is related

to the finite size of GWP. Note that  $E_{cl}$  is conserved exactly since the central trajectory feels the exact, time-independent potential.

#### 4.4 Computational Methods

Dunning’s correlation consistent triple-zeta basis set including polarization functions (aug-cc-pVTZ) was used in all *ab initio* calculations. The  $\tilde{A}^1A_2'' \leftarrow \tilde{X}^1A_1'$  absorption spectrum calculations were performed with either B3LYP or CASPT2 methods, where B3LYP denotes a DFT calculation for the ground state and TD-DFT calculation for the excited state, both using the b3lyp functional, and CASPT2 stands for a CASPT2 calculation with a CASSCF(8/8) reference electronic wave function of the ground or excited state depending on whether  $\tilde{X}^1A_1'$  or  $\tilde{A}^1A_2''$  calculations were performed. Photoelectron spectra were calculated with CCSD and MP2 methods. Here, the neutral  $\text{NH}_3$  molecule and  $\text{NH}_3^+$  cation defined the ground and excited electronic states for the calculations. Therefore, the unrestricted versions of the CCSD and MP2 methods were required for excited electronic state calculations. The Molpro2012.1<sup>172</sup> package was used for CASPT2 and GAUSSIAN09<sup>65</sup> for B3LYP, CCSD, and MP2 calculations. In the packages used, analytical gradients were available for all these methods, but analytical Hessians had been only implemented for MP2 and DFT. The initial GWP was the ground vibrational eigenstate of the harmonic fit to the PES at one of the two degenerate equilibrium geometries of the  $\tilde{X}^1A_1'$  state. The classical trajectory and stability matrix were propagated using the second order symplectic algorithm in the OTF-AI calculation and using an analytical formula in the global harmonic calculations. The GWP was propagated with a time step of 8 a.u.  $\approx$  0.2 fs for 1000 steps (a total time of 8000 a.u.  $\approx$  193.5 fs) for absorption spectra and for 2000 steps (a total time of 16000 a.u.  $\approx$  387.0 fs) for photoelectron spectra. The resulting spectra were shifted (Table 5) to eliminate the systematic errors of *ab initio* vertical excitation energies and broadened by a phenomenological (inhomogeneous) Gaussian with half-width at half-maximum of either 200  $\text{cm}^{-1} \approx$  0.025 eV (for absorption spectra) or 50  $\text{cm}^{-1} \approx$  0.006 eV (for photoelectron spectra).

Table 5: Overall energy shifts in eV introduced into the spectra.

	B3LYP	CASPT2	MP2	CCSD
OTF-AI-TGA	0.57	-0.04	-0.9	0.10
Vertical harmonic model	0.55	-0.05	-0.114	0.08
Adiabatic harmonic model	0.60	0.05	0.00	0.00

---

## 4.5 Results and discussion

### 4.5.1 Absorption spectrum

A single long progression due to the umbrella motion of  $\text{NH}_3$  is observed in the experimental absorption spectrum (see Figure 17), which exhibits substantial broadening, especially in the higher energy region, largely due to photodissociation. Such diffuse spectra depend only on short-time dynamics,<sup>1</sup> during which the OTF-AI-TGA GWP remains trapped in the quasi-bound region of  $\tilde{A}^1A_2''$ , making the comparison with global harmonic models straightforward; in all our calculations, the broadening was taken into account phenomenologically.

Figure 17 compares the experimental spectrum<sup>173</sup> with spectra calculated with the adiabatic harmonic, vertical harmonic, and our OTF-AI-TGA approach using CASPT2 and B3LYP levels of theory. In the adiabatic harmonic model, the stretching modes are overly excited due to their coupling to the bending mode in the Cartesian representation, which results in unphysical progressions.<sup>150, 152, 155</sup> Furthermore, the adiabatic harmonic model is very sensitive to the *ab initio* level of theory: Small changes in equilibrium geometries have a dramatic effect on the spectrum. The vertical harmonic model suffers much less from these two problems and, in addition, it obviously provides a better description of the Franck-Condon region important for spectra calculations.<sup>106, 150, 174</sup> Still, it is clear that neither of the two harmonic models can reproduce the anharmonic peak spacing. In contrast, the local harmonic approximation employed in the OTF-AI-TGA captures partially the anharmonicity of the PES, resulting in an almost perfect peak spacing in the OTF-AI-TGA spectrum. Furthermore, the progression is longer than in the vertical harmonic spectrum and the relative intensity distribution matches well the experiment. Finally, by comparing the B3LYP and CASPT2 calculations we conclude that the *ab initio* level of theory affects more the intensity distribution than the peak spacing.



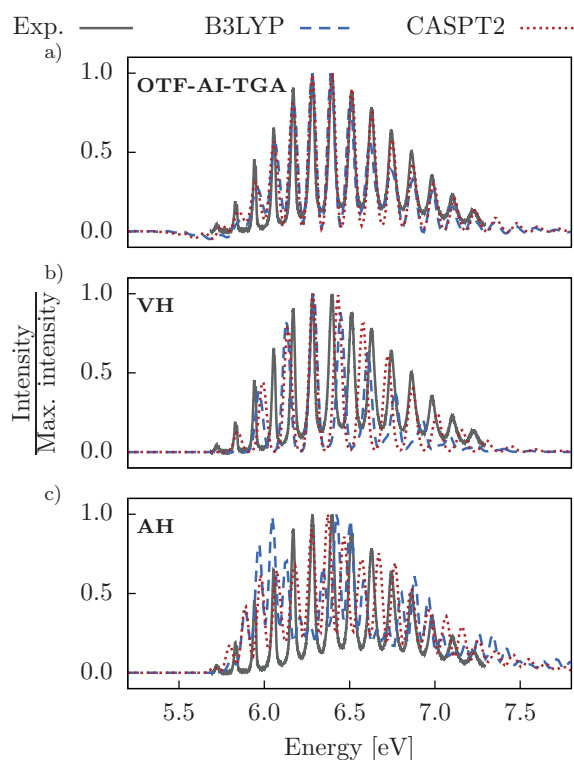


Figure 17: Absorption spectrum of  $\text{NH}_3$ : Comparison of the experimental spectrum<sup>173</sup> recorded at the temperature of 175 K with the spectra computed with the OTF-AI-TGA, vertical harmonic (VH), and adiabatic harmonic (AH) models within the B3LYP and CASPT2 *ab initio* methods. All spectra are rescaled so that the highest spectral peak in each spectrum is of unit intensity.

#### 4.5.2 Photoelectron spectrum

Figure 18 compares the experimental photoelectron spectrum<sup>166</sup> with spectra calculated using the OTF-AI-TGA, vertical harmonic, and adiabatic harmonic models within the CCSD and MP2 levels of theory. As expected, the adiabatic harmonic model fails completely, while the vertical harmonic spectrum contains both the intense and weak progressions, but the main progression is too short and the peak spacing is poor. Compared with the vertical harmonic model, the OTF-AI-TGA significantly improves both the peak spacing and intensity distribution of the main progression. Yet, the spectral intensities obtained with the OTF-AI-TGA combined even with the expensive CCSD method decay faster with increasing distance from the highest peak than do the experimental intensities because the TGA cannot capture the nonlinear spreading of the wave packet due to anharmonicities in the exact potential. Here this effect is stronger than in the absorption spectra since the photoelectron spectra depend on much longer dynamics, allowing the nonlinearities to accumulate. Interestingly, this affects mainly the spectral intensities and not the peak positions, implying that in the photoelectron dynamics of

ammonia the local harmonic approximation for the PES remains accurate for the phase of the thawed Gaussian but not for its density. Also, the weak progression is hidden: The OTF-AI-TGA spectrum exhibits noise and negative intensities, which appear, to a much lower extent, also in the lower-resolution absorption spectrum (see Figure 17). The origin of these negative intensities goes back to the local harmonic approximation, which results in a time-dependent effective potential [Eq. (1.26)] and, therefore, non-conservation of energy — positive intensities in spectra are only guaranteed for time-independent Hamiltonians. To explore this phenomenon in more detail, one can write the total energy of the GWP as a sum of the classical energy  $E_{cl}$  along the central trajectory and semiclassical energy  $E_{sc}$  due to the finite size of the nuclear wave packet (see Subsection 4.3.3). Figure 19 shows that in the OTF-AI propagation scheme,  $E_{cl}$  is conserved exactly since the central trajectory feels the exact, time-independent potential, while  $E_{sc}$  is growing with time. As a result, the total GWP energy is not conserved, which is reflected as noise in the spectrum. This effect does not appear in quadratic PESs (for which the local harmonic approximation does not change the exact potential), and is also negligible for short times.

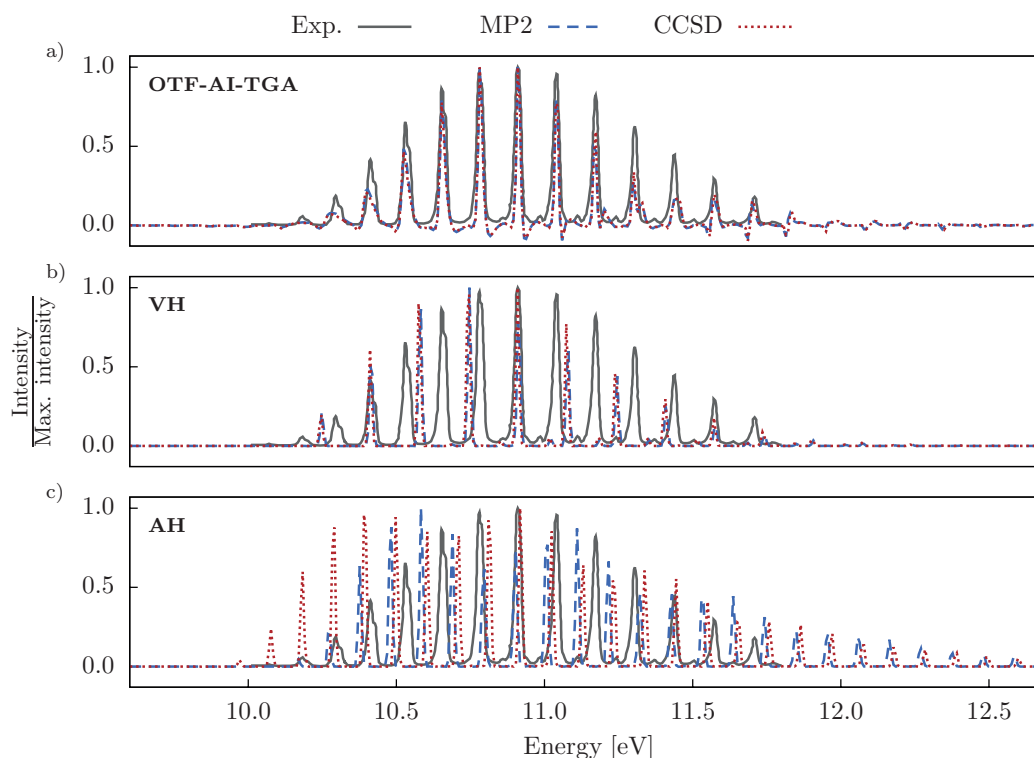


Figure 18: Photoelectron spectrum of  $\text{NH}_3$ : Comparison of the experimental spectrum<sup>166</sup> with the spectra computed with the OTF-AI-TGA, vertical harmonic (VH), and adiabatic harmonic (AH)

models using MP2 and CCSD *ab initio* methods. All spectra are rescaled so that the highest spectral peak in each spectrum is of unit intensity.

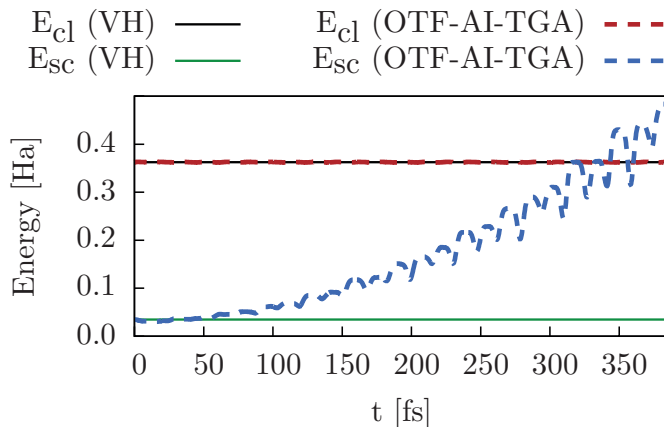


Figure 19: Time dependence of the classical ( $E_{cl}$ ) and semiclassical ( $E_{sc}$ ) energies for the OTF-AI-TGA and vertical harmonic (VH) model using CCSD level of theory. The total GWP energy  $E_{GWP}$  is the sum of  $E_{cl}$  evaluated along the central trajectory and  $E_{sc}$  resulting from the nuclear GWP width. The TGA is exact for quadratic PESs and, consequently,  $E_{GWP}$  is constant in the VH model. For general potentials, however,  $E_{cl}$  stays constant, whereas  $E_{sc}$  increases with time due to the time dependence of the effective potential.

## 4.6 Conclusion

In conclusion, we used ammonia as a prototype of floppy molecules in order to probe the ability of the OTF-AI-TGA to depict large amplitude nuclear motions. Additionally, we pushed the OTF-AI-TGA method to its limit by performing long time propagation in order to assess the accuracy of this approach in describing higher-resolution spectra. The absorption and photoelectron spectra were calculated within the OTF-AI-TGA method and compared with experiment and popular global harmonic approaches. As expected, the adiabatic harmonic model is not usable for floppy molecules with strongly anharmonic PESs, whereas the vertical harmonic model reproduces the main spectral features. The accuracy of the spectra is further significantly improved with the less severe local harmonic approximation employed in the OTF-AI-TGA. We found that in ammonia the simple OTF-AI-TGA is adequate even in the case of large amplitude motions: Both the peak spacing and intensity distributions of experimental spectra are well reproduced. Two drawbacks of the method are that, in contrast to, for example, methods employing Gaussian bases,<sup>16, 79, 175-176</sup> OTF-AI-TGA cannot describe wave packet splitting and that in the limit of long-time propagation necessary for higher-resolution spectra, the local harmonic approximation used in the OTF-AI-TGA induces

---

noise in the spectra that can hide weak progressions. Yet, the computed spectra are better than spectra obtained with the popular global harmonic approaches. Finally, although the OTF-AI-TGA is obviously less accurate than the full quantum dynamical calculation on analytical surfaces, it is much less expensive and does not require any prescreening of the PESs.

---

# Chapter 5 Influence of decoupling a thawed Gaussian wave packet dynamics on spectrum calculations

In Chapter 3, we decoupled the OTF-AI-TGA dynamics in order to decode oligothiophene spectra. For this, we employed a measure of the importance of the couplings between the DOFs based on the stability matrix [Eq. (3.8)]. This measure, however, captures only the couplings due to the propagation and not the couplings resulting merely from the properties of the initial GWP. This fact is not a problem for linear spectroscopy because the normal mode coordinates and the initial GWP are typically based on the same *ab initio* calculation and, therefore, the initial GWP width matrix is diagonal. However, for nonlinear spectra such as the time-resolved emission spectrum presented in Chapter 2, both sources of couplings should be captured. We accordingly test a measure based on the correlation of the GWP width that is able to capture both types of couplings, among others.<sup>177</sup>

## 5.1 Abstract

The thawed Gaussian approximation combined with on-the-fly *ab initio* (OTF-AI-TGA) makes it possible to not only efficiently calculate semiclassical vibronic spectra of medium-sized molecules but also to further analyze the underlying dynamics. This analysis is in general non-trivial since the degrees of freedom are typically coupled among themselves. Our strategy relies on estimating the strength of the couplings among individual degrees of freedom and assembling them into a so-called information flow matrix on the basis of which we then separate the overall dynamics. We employ several definitions of the information flow matrix with the goal of maximizing the extent of the decoupling while minimizing the impact on the final spectrum. Our study, which takes place within

---

a 15-dimensional harmonic model system of dithiophene, demonstrates that the computation can be significantly accelerated – with almost no impact on the spectrum – if the couplings are neglected in the correct frame of reference.

## 5.2 Introduction

In the course of spectroscopic calculations one is typically interested not only in the final result (i.e., in the computed spectrum) but more importantly also in its analysis to gain additional insight into associated physical and chemical processes. However, analyzing the spectral line shape of a vibronic spectrum is often as difficult as it is to calculate the spectrum particularly when an on-the-fly (OTF) scheme is used. Here, the only source of information is dynamics since the global potential energy surface (PES) is not available. One such method is the thawed Gaussian approximation (TGA)<sup>50</sup> combined with OTF *ab initio* (AI) implementation, which will be denoted below as OTF-AI-TGA. The phase-space center of the Gaussian wave packet (GWP) evolves classically on the corresponding PES; its time-dependent width matrix propagates within the local harmonic approximation (LHA) of the PES (see Sections 1.4 and 1.5 for additional details). Despite the apparent simplicity of OTF-AI-TGA we showed in Chapter 3 that it is sufficiently accurate and efficient to treat all 105 vibrational degrees of freedom (DOF) of pentathiophene.

Inspired by the marked dependence of the vibrational line shape of oligothiophenes  $T_n$  on the number  $n$  of elementary rings, we proposed a novel approach in Subsection 3.3.3 for analyzing emission spectra computed with OTF-AI-TGA. This approach allowed us not only to identify the most important DOFs but also to attribute specific spectral features of the oligothiophenes to the dynamical interplay between the quinoid and aromatic character of individual rings. Here, we provide a brief overview of our approach introduced in Subsection 3.3.3.

The principal idea is as follows: In order to globally assess couplings among individual DOFs, we assemble the presumed “measure” of the coupling strength for every pair of DOFs into the so-called *information flow* matrix  $B$ . The particular choice of the quantity measuring the coupling strength for the process of interest is of course not unique. However, we assume that it is chosen in such a way that higher values of  $B_{ij}$  imply higher importance of the coupling among the  $i$ th and  $j$ th DOFs. In loose terms, we expect that a high value of  $B_{ij}$  reflects a high “flow of information” among the corresponding DOFs. Within this spirit we can identify approximately decoupled subsets of DOFs; this step in turn simplifies any dynamical description of the studied process. The

---

full spectrum, for example, can then be computed from the individual contributions of these decoupled subsets.

Thus, we introduce a threshold  $\epsilon_B$  and decompose the set of all DOFs  $\mathcal{D}$  in terms of the so-called  $\epsilon_B$ -partitioning as

$$\mathcal{D} = \bigcup_{\alpha=1}^{c(\mathcal{D}, \epsilon_B)} \mathcal{D}_\alpha^{\epsilon_B}, \quad (5.1)$$

where  $c(\mathcal{D}, \epsilon_B)$  is the number of mutually disjoint subsets  $\mathcal{D}_\alpha^{\epsilon_B}$  defined as the maximal connected components of an undirected graph with adjacency matrix

$$G_{ij} := \begin{cases} 1 & \text{if } \max\{B_{ij}, B_{ji}\} \geq \epsilon_B \\ 0 & \text{otherwise} \end{cases}. \quad (5.2)$$

Briefly put, the spectrum is then decomposed into contributions stemming from individual subsets  $\mathcal{D}_\alpha^{\epsilon_B}$ . Furthermore, we have found that each subspace  $\mathcal{D}_\alpha^{\epsilon_B}$  can be typically associated with a characteristic motion: The induced classical motion within the subspace spanned by the DOFs belonging to  $\mathcal{D}_\alpha^{\epsilon_B}$ .

From the construction of the partitioning of Eq. (5.1), one can directly conclude that a larger threshold  $\epsilon_B$  implies a greater extent of decomposition  $c(\mathcal{D}, \epsilon_B)$ . However, we highlight that low values of  $c(\mathcal{D}, \epsilon_B)$  do not necessarily guarantee small errors per se in the resulting spectrum caused by the neglected couplings since the error also depends on the particular choice of  $B$  (see Subsection 5.3.3). Hence, we are interested in how various definitions of  $B$  perform for separating the  $S_0 \leftarrow S_1$  emission spectrum calculation of dithiophene. In addition, we also study the influence of neglecting different kinds of couplings, denoted *initial* and *dynamical couplings* (see Subsection 5.3.2), on the spectrum calculations. Since TGA is exact for quadratic potentials we evaluate the spectrum within a 15-dimensional harmonic model system, which employs totally symmetric DOFs of the  $S_0$  and the  $S_1$  PESs.

## 5.3 Theory

### 5.3.1 Spectrum calculation

According to Section 1.2 and Subsection 3.3.1, the emission spectrum is obtained as the Fourier transform

---


$$\sigma(\omega) \propto \int C(t) e^{i(\omega + E_{S_1}/\hbar)t} \quad (5.3)$$

of the autocorrelation function

$$C(t) = \langle \psi_{\text{init}} | e^{-i\hat{H}_{S_0}t/\hbar} | \psi_{\text{init}} \rangle, \quad (5.4)$$

where the initial nuclear state  $|\psi_{\text{init}}\rangle$ , stationary in the excited electronic state with energy  $E_{S_1}$ , starts to evolve under the influence of the ground-state Hamiltonian  $\hat{H}_{S_0}$  after undergoing a Franck-Condon transition. Within the  $\epsilon_B$ -partitioning of Eq. (5.1), the complete correlation function  $C(t)$  of Eq. (5.4) is approximated as the product of individual contributions evaluated independently on each subspace  $\mathcal{D}_\alpha^{\epsilon_B}$  [see Eq. (5.1)].

### 5.3.2 Harmonic model

Within the harmonic model employed in this work, we use an adiabatic approach<sup>104, 107</sup> and approximate the ground  $S_0$  and excited  $S_1$  PESs of dithiophene using globally harmonic potentials constructed with respect to the corresponding equilibrium geometries. As shown in the literature, the relevant equilibrium geometries for both electronic states exhibit  $C_{2h}$  symmetry and are planar even though the global equilibrium gas-phase geometry of  $S_0$  is twisted.<sup>108</sup>

Here, we construct the harmonic model in terms of Duschinsky rotation between two sets of normal mode coordinates. Let  $N$  be the number of atoms ( $N = 16$  for dithiophene) and let  $\xi_i$  denote the  $3N$ -vector representing the equilibrium geometry of the  $i$ th electronic state in Cartesian coordinates. The normal-mode vector  $q_i$  associated with  $\xi_i$  is then defined by

$$O_i \cdot q_i = G^{1/2}(\xi - \xi_i), \quad (5.5)$$

where  $G$  is the  $3N \times 3N$  diagonal mass matrix.  $O_i$  represents the leading  $3N \times (3N - 6)$  submatrix of the  $3N \times 3N$  orthogonal matrix  $\bar{O}_i$  diagonalizing the mass-scaled Cartesian Hessian of the  $i$ th PES evaluated at  $\xi_i$ , i.e.,  $\bar{O}_i^T G^{-1/2} \text{Hess}_\xi V|_{\xi_i} G^{-1/2} \bar{O}_i = \bar{\Omega}_i^2$ , where  $\bar{\Omega}_i$  denotes the diagonal matrix of the  $3N$  normal frequencies sorted in descending order.

In our model, we only consider the 15 totally symmetric modes of dithiophene (Table 6) since only these modes are active. This choice significantly reduces the complexity of our analysis. Formally, if we reorder the diagonal of  $\bar{\Omega}_i$  so that the frequencies associat-



---

ed with the totally symmetric modes appear first,  $O_i$  reduces to the  $3N \times 15$  leading submatrix of  $\bar{O}_i$ , and  $q_i$  can be identified with its projection onto the domain of  $O_i$ .

The globally harmonic potential of the  $i$ th PES in the (reduced) vibrational normal mode coordinates  $q_i$  then reads

$$V_i(q_i) = \frac{1}{2} q_i^T \cdot \Omega_i \cdot q_i. \quad (5.6)$$

Furthermore, given two PESs  $A$  and  $B$ , we can express the normal modes coordinates  $q_B$  in terms of  $q_A$  by using Eq. (5.5) as

$$\begin{aligned} q_B &= J \cdot (q_A - d) \\ J &= O_B^T O_A \\ d &= O_A^T G^{1/2} (\xi_B - \xi_A), \end{aligned} \quad (5.7)$$

where  $J$  is a rotation matrix known as the Duschinsky matrix<sup>174</sup> and  $d$  represents the displacement vector. Inserting Eq. (5.7) into Eq. (5.6) yields  $V_B$  expressed in the normal modes coordinates  $q_A$ , namely

$$\begin{aligned} V_B(q_A) &= \frac{1}{2} (q_A - d)^T \cdot K_B \cdot (q_A - d) \\ K_B &= J^T \Omega_B J. \end{aligned} \quad (5.8)$$

Here, the Duschinsky matrix  $J$  is immediately seen to cause couplings since the new Hessian  $K_B$  is obtained via a similarity transformation employing  $J$ .

To construct the harmonic model of dithiophene we can freely choose between the normal-mode coordinates of either the  $S_0$  or the  $S_1$  PES. However, the typical choice for OTF-AI-TGA is to use the normal modes of  $S_1$  since this choice is natural for specification of the initial wave packet  $\psi_{\text{init}}$ . In this setup the width matrix  $A^0$  of the initial GWP is diagonal and the couplings among individual DOFs arise merely due to the dynamics on  $V_{S_0}(q_{S_1})$ , which are denoted *dynamical couplings* below. In contrast, in an alternative setup where the potential is expressed in the normal modes coordinates of  $S_0$ , the dynamics is performed on the uncoupled potential  $V_{S_0}(q_{S_0})$ , but the width matrix  $A^0$  of the initial GWP is coupled and these couplings due to the initial condition are denoted as *initial couplings*.

Therefore, these two options allow us to study two different types of couplings that can arise: The *dynamical couplings* are due to the propagation of the initial GWP on a cou-

pled PES; the *initial couplings*, on the other hand, result merely from the properties of the initial GWP that is then propagated on an uncoupled PES.

### 5.3.3 Construction of the information flow matrix $B$

In this section we present several options for the choice of the information flow matrix  $B$  introduced above. We utilize only those quantities that are already essential for the propagation of the GWP itself so that no significant computational overhead is incurred.

In Subsection 3.3.3 the matrix  $B$  was defined in terms of the stability matrix  $M^t$  as

$$B_{ij}^M = \frac{|\beta_{ij}^M|}{|\beta_{ii}^M|} \quad (5.9)$$

$$\beta^M = \frac{1}{T} \int_0^T dt \left( |M_{qq}^t| + |M_{qp}^t| + |M_{pq}^t| + |M_{pp}^t| \right),$$

where  $|\cdot|$  denotes absolute value.

In addition to the original formulation of  $B^M$ , we test also the symmetrized version here:

$$\bar{B}_{ij}^M = \frac{|\beta_{ij}^M|}{\sqrt{|\beta_{ii}^M| |\beta_{jj}^M|}}. \quad (5.10)$$

Irrespective of how appealing Eqs. (5.9) and (5.10) might seem, if the potential on which the dynamic is performed is uncoupled then  $M^t$  is diagonal and therefore  $B^M$  and  $\bar{B}^M$  describe only the dynamical couplings and not the initial couplings (see Subsection 5.3.2).

To remedy this situation we introduce an alternative definition of  $B$  employing the concept of correlation matrix of a multi-dimensional GWP. Specifically, the correlation  $\rho_{ij}$  of the  $i$ th and  $j$ th DOFs of a GWP density at time  $t$  is defined as

$$\rho_{ij}^t = \frac{\Sigma_{ij}^t}{\sqrt{\Sigma_{ii}^t \Sigma_{jj}^t}} \quad (5.11)$$

$$\Sigma_{ij}^t = \langle \psi^t | (\hat{q} - q^t)_i (\hat{q} - q^t)_j | \psi^t \rangle = \left[ \frac{1}{4} (\text{Re } A^t)^{-1} \right]_{ij},$$

---

where  $\Sigma_{ij}$  denotes the covariance of the  $i$ th and  $j$ th DOFs. The overall strength of the couplings is then estimated by the global time-average of the correlation matrix elements

$$B_{ij}^{\rho} = \frac{1}{T} \int_0^T dt |\rho_{ij}^t|. \quad (5.12)$$

Clearly,  $B^{\rho}$  takes into account the dynamical as well as the initial couplings (see Subsection 5.3.2).

Within the harmonic model [Eq. (5.8)], couplings among the DOFs arise due to the linear coordinate transformation described by the Duschinsky matrix  $J$ . The strength of the coupling between the  $i$ th and  $j$ th DOFs can then be estimated by

$$B_{ij}^J = \sum_k |J_{ik}| |J_{jk}|. \quad (5.13)$$

We call  $B^J$  ‘static’ since it employs only information deduced from the particular form of the harmonic potential and as such cannot be directly applied to general potentials or OTF-AI simulations.

## 5.4 Computational details

The *ab initio* calculations were performed with the Gaussian09 package.<sup>65</sup> The DFT and TD-DFT calculations for the ground and excited states were based on the long-range corrected CAM-B3LYP functional with the 6-31+G(d,p) basis set. Optimizations were performed on the  $S_0$  as well as on the  $S_1$  state. We obtained  $S_0$  planar geometry with constrained optimization since its global *ab initio* equilibrium geometry is ‘twisted’. As noted above, the globally harmonic potential was constructed within the subspace spanned by the totally symmetric normal modes corresponding to the frequencies listed in Table 6. The GWP was propagated for a total time of 80000 au = 1935 fs in order to assure the convergence of  $B^M$ ,  $\bar{B}^M$ , and  $B^{\rho}$ . The resulting spectra were broadened by a phenomenological (inhomogeneous) Gaussian with half-width at half-maximum of 50  $\text{cm}^{-1}$  = 0.0062 eV and shifted by the zero-point energy difference of the full  $S_0$  and  $S_1$  harmonic potentials.

## 5.5 Results and discussion

### 5.5.1 Effect of fully decoupled harmonic models on the spectrum

We begin by studying the limit of high threshold  $\epsilon_B$  so that all DOFs become essentially decoupled, i.e.,  $c(\mathcal{D}, \epsilon_B) = 15$ . Figure 20 then compares the spectra within this limit neglecting either all dynamical or all initial couplings with the spectrum evaluated by taking all couplings into account. Furthermore, we also consider the spectrum calculated within the approximation  $J = \mathbb{I}$ , i.e., disregarding the Duschinsky rotation matrix in Eq. (5.8).

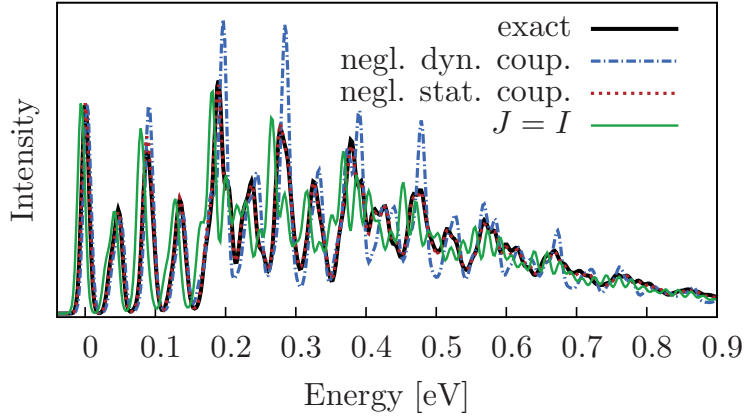


Figure 20: Spectrum of the harmonic model system: Comparison of the exact spectrum with the spectra calculated within three different decoupled harmonic models by neglecting the Duschinsky rotation ( $J = I$ ), neglecting the dynamical couplings (“negl. dyn. coup.”), or neglecting the initial couplings (“negl. init. coup.”).

The character of the potential  $V_{S_0}$  determines the positions of the spectral peaks [after substrating the global shift  $E_{S_1}$  in Eq. (5.3)]; the peak intensities are modulated by the initial GWP  $\psi_{\text{init}}$  defined by potential  $V_{S_1}$ . The initial couplings are therefore less important in the spectrum calculations: The decoupling procedure in terms of the  $\epsilon$ -partitioning affects only  $\psi_{\text{init}}$ , which typically results only in marginal changes in the spectral intensities compared with the exact spectrum (see Figure 20). On the other hand, the omission of the dynamical couplings alters the spectrum more significantly, especially its intensities. However, even though the intensity can change quite drastically, no “unphysical” peaks typically appear in contrast to the spectrum calculated with Duschinsky matrix rotation matrix set to identity matrix. The importance of mode mix-

---

ing due to Duschinsky rotation is well known and explicitly demonstrated by investigating the correlation function or the vibronic spectrum as a function of rotation angles.<sup>175-176</sup>

In summary, our results strongly suggest that if one wishes to employ a (partially) uncoupled harmonic model potential of a molecule then this model should be constructed in terms of the normal modes of the final PES [the target PES of the (de)excitation] taking into account the Duschinsky rotation and then neglecting the off-diagonal terms in the Hessian of the initial PES.

### 5.5.2 Effect of consecutive decoupling on the spectrum

The next question that we wish to address concerns the choice of the information flow matrix  $B$  for which the error introduced into the spectrum increases the slowest as a function of  $c(\mathcal{D}, \epsilon_B)$ . In other words, we seek to understand which measure of the coupling strength exhibits the smallest error for a given order of the  $\epsilon$ -partitioning. We quantify the error of the spectrum as

$$\delta(n) = \sqrt{\frac{\int dE [\sigma_{\text{full}}(E) - \sigma_n(E)]^2}{\int dE [\sigma_{\text{full}}(E)]^2}}, \quad (5.14)$$

where the threshold  $\epsilon_B$  is implicitly defined for a given number of subsets  $n = c(\mathcal{D}, \epsilon_B)$ . The exact spectrum  $\sigma_{\text{full}}$  is calculated with no decoupling ( $n = 1$ ), while the spectrum  $\sigma_n$  is constructed from individual contributions from the  $d$  subspaces  $\mathcal{D}_\alpha^{\epsilon_B}$ . Note that the quantity  $\delta$  takes into account changes in intensities as well as in peak positions. When Duschinsky rotation is neglected  $\delta$  attains a value of  $\delta_j = 0.50$ .

Furthermore, the spectrum calculation can be significantly accelerated since the correlation function  $C(t)$ , necessary for the spectrum evaluation [Eq. (4.1)], can now be obtained as a product of individual contribution evaluated independently on each subset  $\mathcal{D}^{\epsilon_B}$ . This separation significantly reduces the computational costs (CC) that we estimate by

$$\text{CC}(\epsilon_B) = \sum_{i=1}^{c(\mathcal{D}, \epsilon_B)} \text{card}(\mathcal{D}_i^{\epsilon_B})^3, \quad (5.15)$$

where  $\text{card}(\mathcal{D}_i^{\epsilon_B})$  denotes the cardinality of the subset  $\mathcal{D}_i^{\epsilon_B}$  and the third power corresponds to the anticipated scaling of the computational costs of the TGA dynamics with dimensionality due to the inherent determinant and matrix inverse operations.

### 5.5.2.1 Effect of dynamical couplings

First, we test the influence of the dynamical couplings on the spectrum – the couplings that are due to the propagation on a coupled PES. Here, the harmonic model system is constructed in  $S_1$  normal-mode coordinates, which results in a coupled harmonic potential  $V_{S_0}(q_{S_1})$ . It is important to note that the dynamical couplings due to the propagation of the GWP on the  $S_0$  PES cannot be avoided for general potentials. The density plots of  $B^M$ ,  $\bar{B}^M$ , and  $B^J$  displayed in Figure 21 reveal similar patterns that show, in contrast to the pattern in the plot of  $B^\rho$ , strong coupling in the vicinity of the diagonal, i.e., DOFs with close frequencies are linked more strongly.

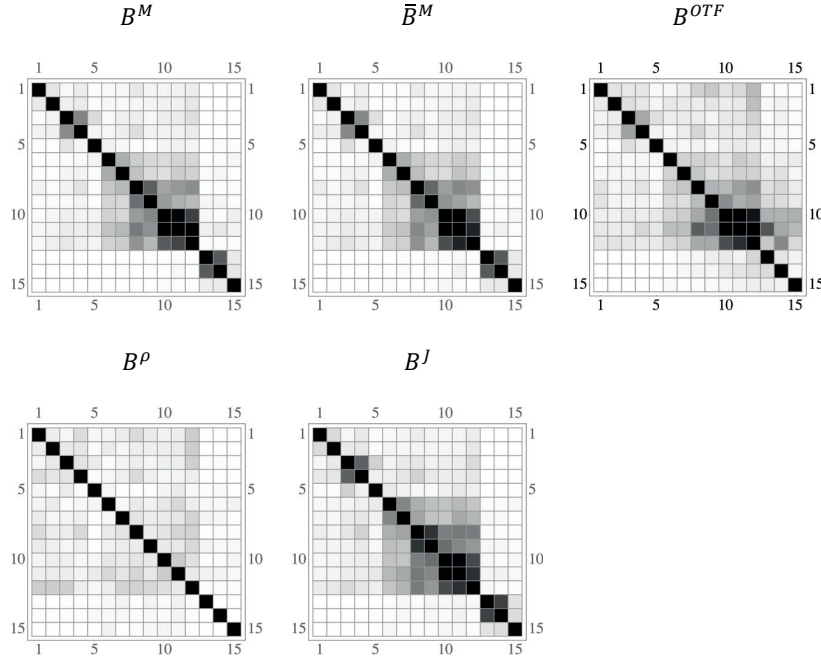


Figure 21: Density plots showing the extent of the couplings between different DOFs. The couplings are estimated by different choices for the information flow matrix  $B$  [Eqs. (5.9), (5.10), (5.12), (5.13)]. Here, the couplings arise due to the propagation of the GWP on the coupled harmonic potential, i.e., the dynamical couplings. The 15 normal mode coordinates  $q_{S_1}$  are labeled consecutively starting with the coordinate associated with the lowest frequency. Darker shades correspond to stronger couplings between two DOFs.

In Figure 21 we also show  $B^{\text{OTF}}$ , the information flow matrix based on the stability matrix [Eq. (5.9)] that corresponds to the OTF-AI-TGA dynamics performed in Chapter 3. While the overall pattern of  $B^{\text{OTF}}$  and its harmonic analogue  $B^M$  are similar,  $B^{\text{OTF}}$  is

---

slightly wilder. This fact indicates that the couplings are more pronounced in the OTF-AI dynamics even in a rather harmonic molecule such as T2. For instance,  $B^{\text{OTF}}$  predicts that mode 13 is coupled to mode 11, which is not described by  $B^M$ . Note that due to the short-time nature of the OTF-AI dynamics, the elements of  $B^{\text{OTF}}$  corresponding to low-frequency DOFs do not converge to the same relative accuracy as the high-frequency components.

Figure 22 shows the error of the spectrum introduced by increasing  $c(\mathcal{D}, \epsilon_B)$  for a particular choice of  $B$ . Note that this error is not guaranteed to increase monotonically with increasing  $c(\mathcal{D}, \epsilon_B)$ . This fact is observed especially for  $B^\rho$ . In terms of the density plot pattern,  $B^M$ ,  $\bar{B}^M$ , and  $B^J$  perform similarly with a slightly better error progression for  $B^M$ . For low decoupling order, i.e.  $c(\mathcal{D}, \epsilon_B) < 9$ ,  $B^\rho$  outperforms the other alternatives. However, the error increases drastically at  $c(\mathcal{D}, \epsilon_B) = 8$ . A closer look at the adjacency matrices, displayed in Figure 23, reveals that the drastic change in the error at  $c(\mathcal{D}, \epsilon_B) = 9$  and for  $B^\rho$  and at  $c(\mathcal{D}, \epsilon_B) = 14$  for  $B^M$ ,  $\bar{B}^M$ , and  $B^J$  is due to the decoupling of the 12th DOF from DOFs 11 and 12. This phenomenon can be explained by the concept of *relative displacement*  $\varrho$  [Eq. (3.11)] that was introduced in Subsection 3.3.3 to estimate the “dynamical importance” of a DOF. The width of the GWP is taken into account in the formulation of  $\varrho$  because a small displacement of a high-frequency (stiff) mode affects the spectrum much more than the same displacement of a low-frequency (soft) mode. In the case of a harmonic potential, the relative displacement for the  $i$ th DOF can be defined as

$$\varrho_i := |2d_i| (A_{ii}^0 / \ln 2)^{1/2}, \quad (5.16)$$

where the scaling factor  $A_{ii}^0$  is the diagonal width matrix element of the initial GWP. Since the relative displacement of a DOF is associated with its importance for the spectrum evaluation, a small error introduced by decoupling DOF 12 (which has the largest  $\varrho$ ; see Table 6) yields a pronounced change in  $\delta_{\text{spec}}$ . Obviously,  $B^\rho$  underestimates the couplings of this important DOF since its decouplings causes a large jump in error at  $c(\mathcal{D}, \epsilon_B) = 9$ . The adjacency matrices furthermore support the observation that  $B^M$ ,  $\bar{B}^M$ , and  $B^J$  measure coupling strengths between DOFs on the same level, which results in the same structure of subsets in the  $\epsilon_B$ -partitioning with only a few exceptions (see Figure 23). The corresponding adjacency matrices exhibit a block-diagonal pattern in contrast to the adjacency matrices for  $B^\rho$  in which the DOFs associated with significantly different frequencies remain coupled even for higher decoupling orders.

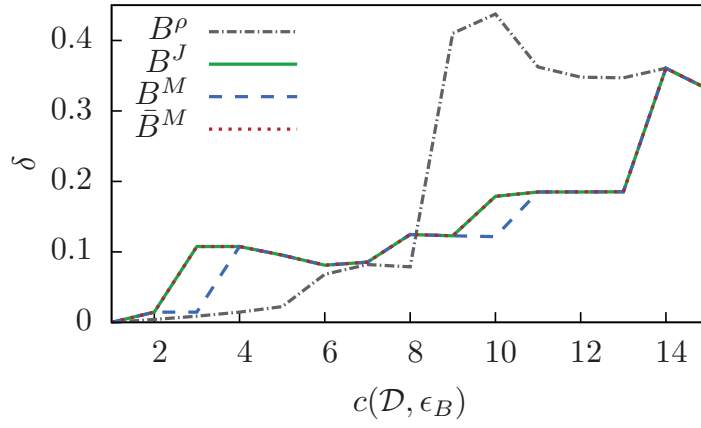


Figure 22: Error in the spectrum calculation [defined in Eq. (5.14)] introduced as a function of the extent of the decoupling  $c(\mathcal{D}, \epsilon_B)$  [Eq. (5.1)]. Here, the couplings arise due to the propagation of the GWP on the coupled harmonic potential, and these dynamical couplings are measured by  $B^\rho, B^M, \bar{B}^M$ , or  $B^J$  introduced in Subsection 5.3.3.



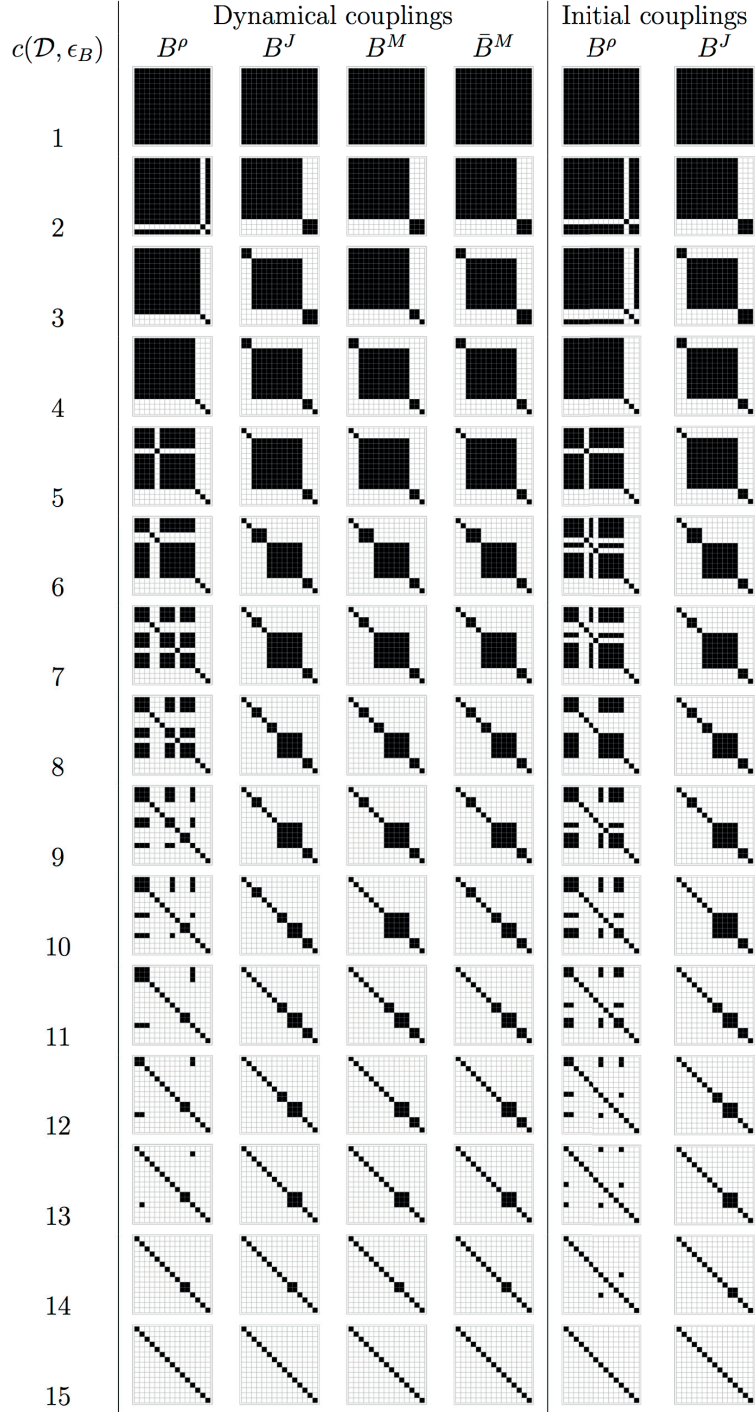


Figure 23: Adjacency matrices [Eq. (5.2)] as a function of the extent of the decoupling  $c(\mathcal{D}, \epsilon_B)$  (1 to 15) and different measure of couplings ( $B^\rho, B^M, \bar{B}^M, B^J$ ) introduced in Subsection 5.3.3. Each adjacency matrix shows which pairs of modes are coupled (black squares) and which are decoupled (white squares). In the panel “dynamical couplings” the couplings arise due to the propagation of the GWP on the coupled harmonic potential; the couplings in the panel “initial couplings” are due to the properties of the initial GWP. The frequencies of the corresponding normal mode coordinates increase from top to bottom and from left to right.

Figure 24 shows that the computational costs can be reduced by an order of magnitude with only a minimal impact on the spectrum of  $\delta \approx 0.1$ . Neglecting all dynamical couplings, i.e.,  $c(\mathcal{D}, \epsilon_B) = 15$ , introduces a smaller error in the spectrum  $\delta_{\text{dyn. coup.}}(15) = 0.33$  than neglecting the Duschinsky rotation; the computational costs are the same for both uncoupled harmonic model systems  $\text{CC}(15) = 15$ .

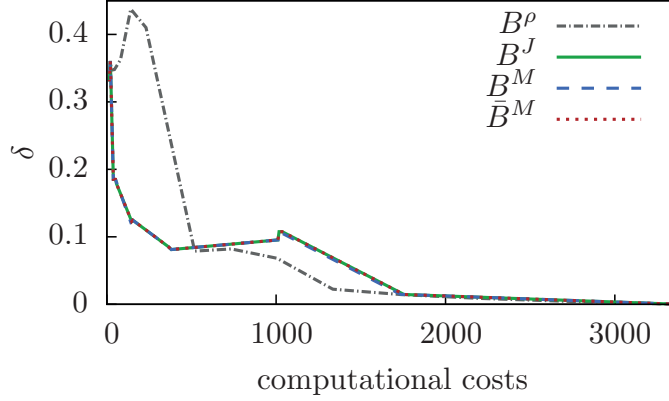


Figure 24: Error in the spectrum [defined in Eq. (5.14)] as a function of computational cost of spectrum calculations estimated using Eq. (5.15). The error in the spectrum calculations is due to neglecting the couplings among the DOFs, i.e., forming uncoupled subsets. The couplings are measured by  $B^\rho$ ,  $B^M$ ,  $\bar{B}^M$ , or  $B^J$ , and they are due here to the propagation of the GWP on the coupled harmonic potential, i.e., dynamical couplings.

### 5.5.2.2 Effect of initial couplings

Here, the GWP dynamics is performed on the uncoupled  $V_{S_0}(q_{S_0})$  and the  $\epsilon_B$ -partitioning, and a particular choice of  $B$  affects the initial GWP width matrix  $A^0$ . Neglecting all initial couplings results in an error of  $\delta^{\text{stat. coup.}}(15) = 0.033$ , which is an order of magnitude smaller than that when neglecting all dynamical couplings  $\delta^{\text{dyn. coup.}}(15) = 0.33$ . This finding agrees with the almost perfect reproduction of the exact spectrum (see Figure 20). As expected, matrices  $B^J$  and  $B^\rho$  exhibit quite different patterns in Figure 25, which are, however, similar to their counterparts in the dynamical couplings picture (Figure 21). The largest jumps in error occur at  $c(\mathcal{D}, \epsilon_B) = 3$  for the  $B^J$  and at  $c(\mathcal{D}, \epsilon_B) = 11$  for the  $B^\rho$   $\epsilon_B$ -partitionings that are shown in Figure 26. Considering the adjacency matrices in Figure 23, these jumps can be related to the decoupling of DOFs 1 and 2 with DOF 3. It is important to note that a drastic increase in error

occurs when the coupled low-frequency DOFs have a large relative displacement of  $\varrho > 1$  (see Table 6). This finding is in contrast with dynamical-coupling studies, where couplings between higher frequency DOFs are responsible for a drastic increase in the error. The importance of the couplings of these low-frequency DOFs is better estimated using  $B^\rho$  and it therefore outperforms  $B^J$  in this case.

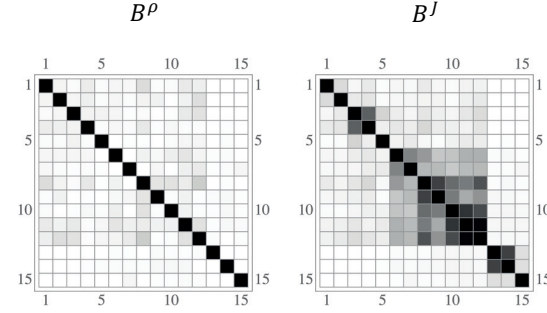


Figure 25: Density plots showing the extent of the couplings between different DOFs. The couplings are estimated by two different choices for the information flow matrix  $B$  [Eqs. (5.12), (5.13)]. Here, the couplings are due to the properties of the initial GWP, which are then propagated on an uncoupled PES, i.e., initial couplings. The 15 normal mode coordinates  $q_{S_1}$  are labeled consecutively starting with the coordinate associated with the lowest frequency. Darker shades correspond to stronger coupling between two DOFs.

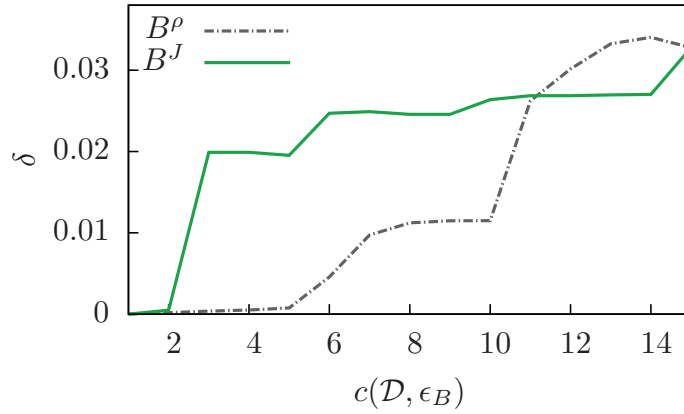


Figure 26: Error in the spectrum calculation [defined in Eq. (5.14)] introduced as a function of the extent of the decoupling  $c(\mathcal{D}, \epsilon_B)$  [Eq. (5.1)]. Here, the couplings are the initial couplings, due to the properties of the initial GWP, which is then propagated on an uncoupled PES. These couplings were measured using  $B^\rho$  or  $B^J$  introduced in Subsection 5.3.3.

Table 6: Frequencies  $\omega$ , given in  $\text{cm}^{-1}$ , and relative displacements Eq. (5.16) corresponding to the normal mode coordinates of  $S_0$ , i.e.,  $q_{S_0}$ , and  $S_1$ , i.e.,  $q_{S_1}$ .

$i$		1	2	3	4	5	6	7	8	9	10	11	12	13	14	15
$q_{S_0}$	$\omega$	297.3	385.0	696.8	762.6	880.9	1082.8	1118.2	1271.6	1294.7	1424.3	1532.4	1642.5	3238.9	3253.5	3287.6
	$\rho$	1.09	1.59	1.84	1.22	0.06	0.71	0.55	0.18	0.07	0.02	2.12	1.6	0.05	0.05	0.03
$q_{S_1}$	$\omega$	290.4	386.5	673.7	712.8	873.2	1102.9	1106.0	1211.3	1316.7	1450.0	1507.2	1657.7	3243.6	3259.2	3282.6
	$\rho$	1.11	1.54	2.16	0.54	0.18	0.36	0.41	0.7	0.44	0.24	0.64	2.57	0.04	0.03	0.02

## 5.6 Conclusions

We tested the performance of four particular choices to estimate the coupling strength between the DOFs with the intent to separate the TGA dynamics and thus decompose the resulting spectra into individual independent contributions. We focused on testing four particular choices for measuring the importance of the couplings on a 15-dimensional harmonic model system, employing the totally symmetric DOFs of the  $S_0$  and the  $S_1$  PESs of dithiophene. As a byproduct, we were able to reduce the computational costs while keeping the error, introduced due to neglecting some of the couplings, small.

We found that if the spectrum was evaluated within a harmonic model, its analysis should be done in the final state normal-mode coordinates. Omission of the *initial couplings*, which are due to the initial condition, results in a spectrum that is almost indistinguishable from the exact one. The computational costs, however, are significantly reduced since the spectrum can be now evaluated in an uncoupled harmonic system. In contrast, the vibronic spectra calculated within an uncoupled harmonic model system that is constructed by neglecting Duschinsky rotation are much harder to interpret due to the appearance of spurious unphysical peaks.

In the case of what we call *dynamical couplings*, the couplings are due to the propagation of the initial GWP on a coupled PES. Here, measures of their importance bases on the stability matrix ( $B^M$ ,  $\bar{B}^M$ ) or the Duschinsky rotation matrix ( $B^J$ ) decouple the system in a similar way by forming block-diagonal adjacency matrices, i.e., the DOFs associated with neighboring frequencies mix more strongly. On the other hand, a measure based on the correlation of the GWP width ( $B^\rho$ ) couples the DOFs more uniformly and, consequently, the resulting partitioning forms different subsets. In general,  $B^\rho$  underestimates the strength of the couplings among the DOFs associated with higher frequen-

---

cies;  $B^M$ ,  $\bar{B}^M$ , and  $B^J$  exhibit coupling strengths that are too low for low-frequency DOFs.

For general potentials – and especially when an OTF scheme is applied – the reference coordinate system is often fixed and couplings are inevitable. Only  $B^p$  can feel the initial couplings and the dynamical couplings in this situation. However,  $B^M$  can still be used for separating the dynamics even when initial couplings are present: The initial couplings affect the spectrum only weakly and the importance of the high-frequency DOFs couplings is better estimated using  $B^M$ . Moreover, these couplings are more important due to the shorter timescales of an OTF calculation.

Knowledge is often limited about the PES on which the dynamics is performed when the OTF scheme is employed in calculations. The OTF-AI-TGA can provide useful information for defining subspaces of reduced dimensionality. In the spirit of Grossmann and coworkers<sup>145, 178-180</sup>, the few DOFs of the subspaces that are important for the spectral features can be studied using less-efficient but better-suited methods and the remaining DOFs, loosely interpreted as the bath, can be calculated within OTF-AI-TGA. To this end, alternative approaches for constructing the information flow matrices that maximize the degree of decoupling and minimize the impact on the resulting spectrum and the computational costs are an ongoing subject of our research. An optimized coordination reference frame that minimizes all types of couplings could then be extracted from this information.



---

## Chapter 6 Conclusion and outlook

In this thesis, we explored different ways to accelerate the calculations of electronic spectra and presented a systematic approach for their analyses.

First, we showed that the efficiency of quantum dynamics performed on an equidistant grid using a split-operator approach, suitable for small systems, is increased with higher-order splitting schemes. However, care has to be taken as to the numerical stability of these splitting schemes with respect to the grid spacing.

We combined the *thawed Gaussian approximation* (TGA) with an on-the-fly *ab initio* (OTF-AI) scheme to consider, at least to some extent, the nuclear quantum effects for larger molecular systems for which direct quantum treatment meets its demise. While the TGA wave packet dynamics is efficient enough to treat all vibrational DOFs on an equal footing, the OTF-AI scheme overcomes the problem of the computationally costly construction of the potential energy surfaces required in alternative methods.

This efficient framework, despite its apparent simplicity, reproduces almost perfectly the emission spectra of oligothiophenes as well as the absorption and photoelectron spectra of ammonia. Hence, the OTF-AI-TGA paves the way for semiclassical calculations of spectra of larger systems. Furthermore, it yields good performance especially for spectra that depend strongly on large amplitude motions.

In spectroscopic calculations, one is usually interested not only in the final product, i.e., in the resulting spectrum, but more importantly also in its analysis. It is the analysis that provides additional insight into the associated physical and chemical processes. Therefore, we presented a novel approach for analyzing spectra computed with OTF-AI-TGA: Information gathered during the dynamics is used to identify groups of the most important DOFs. This not only allows specific spectral features to be attributed to the underlying motion, but also to explain their differences (see Figure 27).

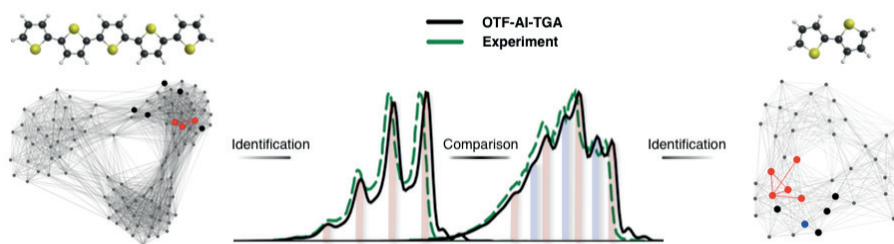


Figure 27: Overview of the analysis approach: First, groups of the most important DOFs are identified on the basis of OTF-AI-TGA dynamics. Second, the underlying classical motion within the DOFs comprising these groups is attributed to specific spectral features.

Note that the OTF-AI-TGA framework is not restricted merely to linear spectroscopy; nonlinear spectra such as time-resolved stimulated emission spectra (displayed in Figure 28) can also be simulated. To be able to explain, for example, the change in line shape with increasing delay times between pump and probe pulses, the analysis approach introduced in Subsection 3.3.3 and further studied in Chapter 4, has to be extended. Clearly, this generalization would constitute a useful tool in the investigation of such questions. It would ensure that the relevant information does not get obscured in the high complexity of the process (and/or system) or by the amount of data generated.

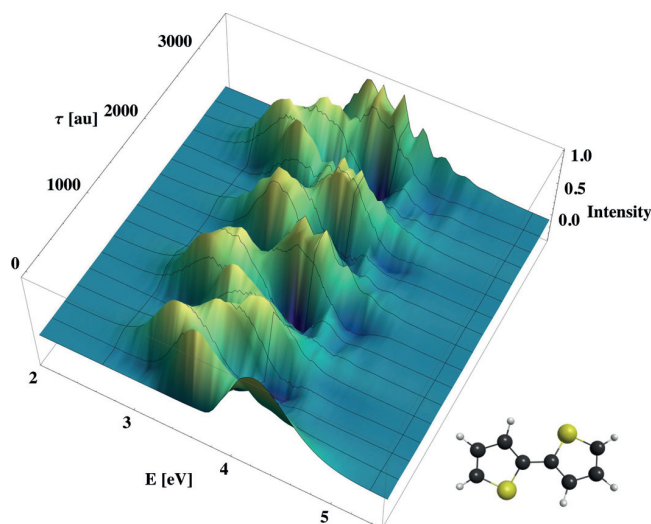


Figure 28: Time-resolved stimulated emission spectrum [Eq. (2.3)] of dithiophene computed with OTF-AI-TGA using b3lyp/6-31+G(d,p) *ab initio* setup. The larger the delay time  $\tau$  between the pump and the probe pulses, the better the resolution of the spectrum. Such effects were already reported in experiments with similar molecules.<sup>181</sup>



---

The OTF-AI framework has become steadily more and more popular thanks to increasing availability of computational resources and advances in electronic structure methods. In this field, pragmatic methods such as OTF-AI-TGA fill the gap between classical and full quantum treatments. Although many purely quantum effects such as interference, wave-packet splitting, or non-adiabatic transitions cannot be captured by OTF-AI-TGA, this method undoubtedly provides a useful preliminary test in such situations. The analysis of the OTF-AI-TGA dynamics can be used to define a subspace of reduced dimensionality, within which the most important dynamics occurs. Consequently, less efficient yet better-suited methods can be used within this subspace.

For example, employing the multi-trajectory Herman-Kluk method on the important subspace combined with TGA for the remaining DOFs (loosely interpreted as the bath) results in the semiclassical hybrid dynamics introduced by Grossmann.<sup>145, 178-180</sup> Inspired by these ideas, we intend to combine OTF-AI-TGA with, in principle, exact quantum dynamics in an OTF-AI time-dependent Gaussian basis generated with an optimized sampling algorithm. Within this framework, the number of trajectories is expected to be drastically reduced versus the pioneering semiclassical OTF-AI study by Tatchen and Pollak<sup>19</sup> who calculated the Herzberg-Teller absorption spectrum of formaldehyde.

The OTF-AI-TGA method opens the door to large molecules: Its simplicity, efficiency, and robustness are well-suited for tackling *a priori* unknown molecular systems and—in combination with the novel analysis approach—provides the first crucial step in a possible hierarchical protocol for computing and analyzing spectra of large systems.



---

## Chapter 7 Bibliography

1. Heller, E. J. *Acc. Chem. Res.* **1981**, *14* (12), 368-375.
2. Kosloff, R.; Hammerich, A. D.; Tannor, D. *Phys. Rev. Lett.* **1992**, *69* (15), 2172-2175.
3. Tannor, D. *Introduction to Quantum Mechanics: A Time Dependent Perspective*. University Science Books: 2006.
4. Zimmermann, T.; Vaníček, J. *J. Chem. Phys.* **2014**, *141* (13), 134102.
5. Van Vleck, J. H. *Proc. Nat. Acad. Sci. USA* **1928**, *14* (2), 178-188.
6. Herman, M. F.; Kluk, E. *Chem. Phys.* **1984**, *91* (1), 27.
7. Herman, M. F. *Annu. Rev. Phys. Chem.* **1994**, *45* (1), 83-111.
8. Kay, K. G. *J. Chem. Phys.* **1994**, *100* (6), 4377-4392.
9. Kay, K. G. *J. Chem. Phys.* **1994**, *100* (6), 4432-4445.
10. Brewer, M. L.; Hulme, J. S.; Manolopoulos, D. E. *J. Chem. Phys.* **1997**, *106* (12), 4832-4839.
11. Wehrle, M.; Šulc, M.; Vaníček, J. *Chimia* **2011**, *65* (5), 334-338.
12. Tatchen, J.; Pollak, E.; Tao, G.; Miller, W. H. *J. Chem. Phys.* **2011**, *134* (13), 134104.
13. Gelabert, R.; Giménez, X.; Thoss, M.; Wang, H.; Miller, W. H. *J. Phys. Chem. A* **2000**, *104* (45), 10321-10327.
14. Kaledin, A. L.; Miller, W. H. *J. Chem. Phys.* **2003**, *118* (16), 7174-7182.
15. Burant, J. C.; Batista, V. S. *J. Chem. Phys.* **2002**, *116* (7), 2748-2756.
16. Walton, A. R.; Manolopoulos, D. E. *Mol. Phys.* **1996**, *87* (4), 961.
17. Miller, W. H. *J. Phys. Chem. A* **2001**, *105* (13), 2942-2955.
18. Heller, E. J. *J. Chem. Phys.* **1981**, *75* (6), 2923.
19. Tatchen, J.; Pollak, E. *J. Chem. Phys.* **2009**, *130* (4), 041103.
20. Vaníček, J.; Heller, E. J. *Phys. Rev. E* **2003**, *68* (5), 056208.
21. Vaníček, J. *Phys. Rev. E* **2004**, *70* (5), 055201.
22. Vaníček, J. *Phys. Rev. E* **2006**, *73* (4), 046204.
23. Miller, W. H.; Smith, F. T. *Phys. Rev. A* **1978**, *17* (3), 939-953.
24. Hubbard, L. M.; Miller, W. H. *J. Chem. Phys.* **1983**, *78* (4), 1801-1807.
25. Peres, A. *Phys. Rev. A* **1984**, *30* (4), 1610-1615.

- 
26. Mukamel, S. *J. Chem. Phys.* **1982**, *77* (1), 173-181.
  27. Mukamel, S.; Islampour, R. *Chem. Phys. Lett.* **1984**, *108* (2), 161-165.
  28. Shi, Q.; Geva, E. *J. Chem. Phys.* **2005**, *122* (6), 064506.
  29. McRobbie, P. L.; Hanna, G.; Shi, Q.; Geva, E. *Acc. Chem. Res.* **2009**, *42* (9), 1299-1309.
  30. Li, Z.; Fang, J. Y.; Martens, C. C. *J. Chem. Phys.* **1996**, *104* (18), 6919-6929.
  31. Egorov, S. A.; Rabani, E.; Berne, B. J. *J. Chem. Phys.* **1998**, *108* (4), 1407-1422.
  32. Egorov, S. A.; Rabani, E.; Berne, B. J. *J. Chem. Phys.* **1999**, *110* (11), 5238.
  33. Shemetulskis, N. E.; Loring, R. F. *J. Chem. Phys.* **1992**, *97* (2), 1217.
  34. Rost, J. M. *J. Phys. B: At., Mol. Opt. Phys.* **1995**, *28* (19), L601.
  35. Li, B.; Mollica, C.; Vaníček, J. *J. Chem. Phys.* **2009**, *131* (4), 041101.
  36. Zimmermann, T.; Ruppen, J.; Li, B.; Vaníček, J. *Int. J. Quantum Chem* **2010**, *110* (13), 2426.
  37. Wang, W.-g.; Casati, G.; Li, B.; Prosen, T. *Phys. Rev. E* **2005**, *71* (3), 037202.
  38. Ares, N.; Wisniacki, D. A. *Phys. Rev. E* **2009**, *80* (4), 046216.
  39. Ignacio, G.-M.; Diego, A. W. *J. Phys. A: Math. Theor.* **2011**, *44* (31), 315101.
  40. Wisniacki, D. A.; Ares, N.; Vergini, E. G. *Phys. Rev. Lett.* **2010**, *104* (25), 254101.
  41. Zimmermann, T.; Vaníček, J. *J. Chem. Phys.* **2010**, *132* (24), 241101.
  42. Zimmermann, T.; Vaníček, J. *J. Chem. Phys.* **2012**, *136* (9), 094106.
  43. Zimmermann, T.; Vaníček, J. *J. Chem. Phys.* **2012**, *137* (22), 22A516.
  44. Mollica, C.; Vaníček, J. *Phys. Rev. Lett.* **2011**, *107* (21), 214101.
  45. Heller, E. J. *J. Chem. Phys.* **1991**, *94* (4), 2723-2729.
  46. Zambrano, E.; Šulc, M.; Vaníček, J. *J. Chem. Phys.* **2013**, *139* (5), 054109.
  47. Šulc, M.; Vaníček, J. *Mol. Phys.* **2012**, *110* (9-10), 945-955.
  48. Šulc, M.; Hernández, H.; Martínez, T. J.; Vaníček, J. *J. Chem. Phys.* **2013**, *139* (3), 034112.
  49. Zambrano, E.; Ozorio de Almeida, A. M. *Phys. Rev. E* **2011**, *84* (4), 045201.
  50. Heller, E. J. *J. Chem. Phys.* **1975**, *62* (4), 1544-1555.
  51. Lee, S. Y.; Heller, E. J. *J. Chem. Phys.* **1982**, *76* (6), 3035-3044.
  52. Lee, S. Y.; Heller, E. J. *J. Chem. Phys.* **1979**, *71* (12), 4777-4788.
  53. Myers, A. B.; Mathies, R. A.; Tannor, D. J.; Heller, E. J. *J. Chem. Phys.* **1982**, *77* (8), 3857-3866.
  54. Heller, E. J.; Sundberg, R.; Tannor, D. *J. Phys. Chem.* **1982**, *86* (10), 1822-1833.
  55. Tannor, D. J.; Heller, E. J. *J. Chem. Phys.* **1982**, *77* (1), 202-218.
  56. Worth, G. A.; Robb, M. A.; Lasorne, B. *Mol. Phys.* **2008**, *106* (16-18), 2077-2091.
  57. Worth, G. A.; Robb, M. A. Applying Direct Molecular Dynamics to Non-Adiabatic Systems. In *The Role of Degenerate States in Chemistry*, John Wiley & Sons, Inc.: 2003; pp 355-431.

- 
58. Wehrle, M.; Šulc, M.; Vaníček, J. *J. Chem. Phys.* **2014**, *140* (24), 244114.
59. Hougen, J. T.; Watson, J. K. G. *Can. J. Phys.* **1965**, *43* (2), 298-320.
60. Özkan, İ. *J. Mol. Spectrosc.* **1990**, *139* (1), 147-162.
61. Kudin, K. N.; Dymarsky, A. Y. *J. Chem. Phys.* **2005**, *122* (22), 224105.
62. Kearsley, S. *Acta Crystallographica Section A* **1989**, *45* (2), 208-210.
63. Coutsiias, E. A.; Seok, C.; Dill, K. A. *J. Comput. Chem.* **2004**, *25* (15), 1849-1857.
64. *Mathematica*, Version 9.0; Wolfram Research Inc: 2012.
65. Frisch, M. J.; Trucks, G. W.; Schlegel, H. B.; Scuseria, G. E.; Robb, M. A.; Cheeseman, J. R.; Scalmani, G.; Barone, V.; Mennucci, B.; Petersson, G. A., et al. *Gaussian-09 Revision C.01*.
66. Buchowiecki, M.; Vaníček, J. *J. Chem. Phys.* **2010**, *132* (19), 194106.
67. Zimmermann, T.; Vaníček, J. *J. Chem. Phys.* **2009**, *131* (2), 024111.
68. Zimmermann, T.; Vaníček, J. *J. Mol. Model.* **2010**, *16* (11), 1779.
69. Meyer, H.-D.; Gatti, F.; Worth, G. A. *Multidimensional Quantum Dynamics: MCTDH Theory and Applications*. Wiley-VCH: Weinheim, 2009.
70. Lubich, C. *From Quantum to Classical Molecular Dynamics: Reduced Models and Numerical Analysis*. 12 ed.; European Mathematical Society: 2008.
71. Feit, M. D.; Fleck, J. A.; Steiger, A. *Journal of Computational Physics* **1982**, *47* (3), 412.
72. Forest, E.; Ruth, R. D. *Physica D* **1990**, *43* (1), 105.
73. Yoshida, H. *Phys. Lett. A* **1990**, *150* (5-7), 262.
74. Suzuki, M. *Phys. Lett. A* **1995**, *201* (5-6), 425.
75. Bandrauk, A. D.; Dehghanian, E.; Lu, H. *Chem. Phys. Lett.* **2006**, *419* (4-6), 346.
76. Prosen, T.; Pižorn, I. *J. Phys. A: Math. Gen.* **2006**, *39* (20), 5957.
77. Suzuki, M. New Scheme of Hybrid Exponential Product Formulas. In *Computer Simulation Studies in Condensed-Matter Physics*, Landau, D. P.; Mon, K.-K.; Schüttler, H.-B., Eds. Springer: Berlin, 1995; Vol. VIII, p 169.
78. Trotter, H. F. *Proc. Amer. Math. Soc.* **1959**, *10*, 545.
79. Chin, S. A. *Phys. Lett. A* **1997**, *226* (6), 344.
80. Gutzwiller, M. C. *J. Math. Phys.* **1967**, *8* (10), 1979.
81. Miller, W. H. *J. Chem. Phys.* **1970**, *53* (9), 3578.
82. Miller, W. H. *J. Phys. Chem. A* **2001**, *105* (13), 2942.
83. Heller, E. J. *J. Chem. Phys.* **1991**, *94* (4), 2723.
84. Mukamel, S. *Principles of Nonlinear Optical Spectroscopy*. OUP USA: 1999.
85. Li, Y.; Carter, S.; Hirsch, G.; Buenker, R. J. *Mol. Phys.* **1993**, *80* (1), 145.
86. Kosloff, R.; Tal-Ezer, H. *Chem. Phys. Lett.* **1986**, *127* (3), 223.
87. Baer, R.; Kosloff, R. *J. Phys. Chem.* **1995**, *99* (9), 2534.
88. widths are approximately equal to (15.73,11.08), the centre is shifted by (10.8, 3.1) a.u.

- 
89. Pollard, W. T.; Lee, S. Y.; Mathies, R. A. *J. Chem. Phys.* **1990**, *92* (7), 4012.
  90. Kay, K. G. *J. Chem. Phys.* **1994**, *101* (3), 2250.
  91. Walton, A. R.; Manolopoulos, D. E. *Chem. Phys. Lett.* **1995**, *244* (5-6), 448.
  92. Perepichka, D. F.; Perepichka, I. F. *Handbook of Thiophene-Based Materials*. John Wiley and Sons: 2009.
  93. Mishra, A.; Ma, C.-Q.; Bäuerle, P. *Chem. Rev.* **2009**, *109* (3), 1141-1276.
  94. Perepichka, I. F.; Perepichka, D. F.; Meng, H.; Wudl, F. *Adv. Mater.* **2005**, *17* (19), 2281-2305.
  95. Perepichka, D. F.; Meng, H.; Wudl, F. *Organic Electronics: Materials, Manufacturing, and Applications*. Wiley-VCH Verlag: 2006.
  96. Yang, A.; Kuroda, M.; Shiraishi, Y.; Kobayashi, T. *J. Phys. Chem. B* **1998**, *102* (19), 3706-3711.
  97. Yang, A.; Hughes, S.; Kuroda, M.; Shiraishi, Y.; Kobayashi, T. *Chem. Phys. Lett.* **1997**, *280* (5-6), 475-480.
  98. Becker, R. S.; Seixas de Melo, J.; Maçanita, A. L.; Elisei, F. *J. Phys. Chem.* **1996**, *100* (48), 18683-18695.
  99. Zade, S. S.; Bendikov, M. *Org. Lett.* **2006**, *8* (23), 5243-5246.
  100. Hutchison, G. R.; Zhao, Y.-J.; Delley, B.; Freeman, A. J.; Ratner, M. A.; Marks, T. J. *Physical Review B* **2003**, *68* (3), 035204.
  101. Thémans, B.; Salaneck, W. R.; Brédas, J. L. *Synth. Met.* **1989**, *28* (1-2), 359-364.
  102. Avila Ferrer, F. J.; Cerezo, J.; Stendardo, E.; Improta, R.; Santoro, F. *J. Chem. Theory Comput.* **2013**, *9* (4), 2072-2082.
  103. Jacquemin, D.; Planchat, A.; Adamo, C.; Mennucci, B. *J. Chem. Theory Comput.* **2012**, *8* (7), 2359-2372.
  104. Biczysko, M.; Bloino, J.; Santoro, F.; Barone, V. Time-Independent Approaches to Simulate Electronic Spectra Lineshapes: From Small Molecules to Macrosystems. In *Computational Strategies for Spectroscopy*, John Wiley & Sons, Inc.: 2011; pp 361-443.
  105. Tatchen, J.; Pollak, E. *J. Chem. Phys.* **2008**, *128* (16), 164303.
  106. Cerezo, J.; Zúñiga, J.; Requena, A.; Ávila Ferrer, F. J.; Santoro, F. *J. Chem. Theory Comput.* **2013**, *9* (11), 4947-4958.
  107. Avila Ferrer, F. J.; Santoro, F. *Phys. Chem. Chem. Phys.* **2012**, *14* (39), 13549-13563.
  108. Stendardo, E.; Avila Ferrer, F.; Santoro, F.; Improta, R. *J. Chem. Theory Comput.* **2012**, *8* (11), 4483-4493.
  109. Ianculescu, R.; Tatchen, J.; Pollak, E. *J. Chem. Phys.* **2013**, *139* (15), 154311.
  110. Wong, S. Y. Y.; Benoit, D. M.; Lewerenz, M.; Brown, A.; Roy, P.-N. *J. Chem. Phys.* **2011**, *134* (9), 094110.
  111. Ceotto, M.; Valteau, S.; Tantardini, G. F.; Aspuru-Guzik, A. *J. Chem. Phys.* **2011**, *134* (23), 234103.
  112. Ceotto, M.; Atahan, S.; Tantardini, G. F.; Aspuru-Guzik, A. *J. Chem. Phys.* **2009**, *130* (23), 234113.

- 
113. Ceotto, M.; Atahan, S.; Shim, S.; Tantardini, G. F.; Aspuru-Guzik, A. *Phys. Chem. Chem. Phys.* **2009**, *11* (20), 3861-3867.
114. Lami, A.; Santoro, F. Time-Dependent Approaches to Calculation of Steady-State Vibronic Spectra: From Fully Quantum to Classical Approaches. In *Computational Strategies for Spectroscopy*, John Wiley & Sons, Inc.: 2011; pp 475-516.
115. Bakken, V.; Millam, J. M.; Bernhard Schlegel, H. *J. Chem. Phys.* **1999**, *111* (19), 8773-8777.
116. Hratchian, H. P.; Schlegel, H. B. *J. Chem. Theory Comput.* **2005**, *1* (1), 61-69.
117. Millam, J. M.; Bakken, V. r.; Chen, W.; Hase, W. L.; Schlegel, H. B. *J. Chem. Phys.* **1999**, *111* (9), 3800-3805.
118. Lourderaj, U.; Song, K.; Windus, T. L.; Zhuang, Y.; Hase, W. L. *J. Chem. Phys.* **2007**, *126* (4), 044105.
119. Wu, H.; Rahman, M.; Wang, J.; Loudaraj, U.; Hase, W. L.; Zhuang, Y. *J. Chem. Phys.* **2010**, *133* (7), 074101.
120. Ceotto, M.; Zhuang, Y.; Hase, W. L. *J. Chem. Phys.* **2013**, *138* (5), 054116.
121. Zhuang, Y.; Siebert, M. R.; Hase, W. L.; Kay, K. G.; Ceotto, M. *J. Chem. Theory Comput.* **2013**, *9* (1), 54-64.
122. Cederbaum, L. S.; Gindensperger, E.; Burghardt, I. *Phys. Rev. Lett.* **2005**, *94* (11), 113003.
123. Picconi, D.; Avila Ferrer, F. J.; Improta, R.; Lami, A.; Santoro, F. *Faraday Discuss.* **2013**, *163* (0), 223-242.
124. Stock, G.; Woywod, C.; Domcke, W.; Swinney, T.; Hudson, B. S. *J. Chem. Phys.* **1995**, *103* (16), 6851-6860.
125. Ben-Nun, M.; Martínez, T. J. Ab Initio Quantum Molecular Dynamics. In *Adv. Chem. Phys.*, John Wiley & Sons, Inc.: 2002; pp 439-512.
126. Worth, G. A.; Robb, M. A.; Burghardt, I. *Faraday Discuss.* **2004**, *127* (0), 307-323.
127. Shalashilin, D. V.; Child, M. S. *J. Chem. Phys.* **2000**, *113* (22), 10028-10036.
128. Kay, K. G. *Annu. Rev. Phys. Chem.* **2005**, *56* (1), 255-280.
129. Thoss, M.; Wang, H. *Annu. Rev. Phys. Chem.* **2004**, *55* (1), 299-332.
130. Belletete, M.; Leclerc, M.; Durocher, G. *J. Phys. Chem.* **1994**, *98* (38), 9450-9456.
131. Chadwick, J. E.; Kohler, B. E. *J. Phys. Chem.* **1994**, *98* (14), 3631-3637.
132. Becker, R. S.; de Melo, J. S.; Maçanita, A. L.; Elisei, F. *Pure Appl. Chem.* **1995**, *67* (1), 9-16.
133. Gierschner, J.; Cornil, J.; Egelhaaf, H. J. *Adv. Mater.* **2007**, *19* (2), 173-191.
134. Lumpi, D.; Horkel, E.; Plasser, F.; Lischka, H.; Fröhlich, J. *ChemPhysChem* **2013**, *14* (5), 1016-1024.
135. Ponce Ortiz, R.; Casado, J.; Rodríguez González, S.; Hernández, V.; López Navarrete, J. T.; Viruela, P. M.; Ortí, E.; Takimiya, K.; Otsubo, T. *Chemistry – A European Journal* **2010**, *16* (2), 470-484.
136. Fazzi, D.; Canesi, E. V.; Negri, F.; Bertarelli, C.; Castiglioni, C. *ChemPhysChem* **2010**, *11* (17), 3685-3695.

- 
137. Beljonne, D.; Cornil, J.; Friend, R. H.; Janssen, R. A. J.; Brédas, J. L. *JACS* **1996**, *118* (27), 6453-6461.
138. Zerbi, G.; Castiglioni, C.; Del Zoppo, M. Structure and Optical Properties of Conjugated Oligomers from their Vibrational Spectra. Müllen, K.; Wegner, G., Eds. Wiley-VCH Verlag GmbH: 2007; pp 345-402.
139. Zerbi, G.; Castiglioni, C.; Lopez Navarrete, J. T.; Bogang, T.; Gussoni, M. *Synth. Met.* **1989**, *28* (3), D359-D368.
140. Geisselbrecht, J.; Kürti, J.; Kuzmany, H. *Synth. Met.* **1993**, *57* (2-3), 4266-4271.
141. Castiglioni, C.; Tommasini, M.; Zerbi, G. *Philos. Trans. R. Soc. A* **2004**, *362* (1824), 2425-2459.
142. Ortí, E.; Viruela, P. M.; Viruela, R.; Effenberger, F.; Hernández, V.; López Navarrete, J. T. *J. Phys. Chem. A* **2005**, *109* (39), 8724-8731.
143. Zerbi, G.; Chierichetti, B.; Ingánas, O. *J. Chem. Phys.* **1991**, *94* (6), 4637-4645.
144. Lopez Navarrete, J. T.; Zerbi, G. *J. Chem. Phys.* **1991**, *94* (2), 965-970.
145. Grossmann, F. *J. Chem. Phys.* **2006**, *125* (1), 014111.
146. Wehrle, M.; Oberli, S.; Vanicek, J. *J. Phys. Chem. A* **2015**.
147. Ceotto, M.; Tantardini, G. F.; Aspuru-Guzik, A. *J. Chem. Phys.* **2011**, *135* (21), 214108.
148. Wolf, T. J. A.; Kuhlman, T. S.; Schalk, O.; Martinez, T. J.; Moller, K. B.; Stolow, A.; Unterreiner, A. N. *Phys. Chem. Chem. Phys.* **2014**, *16* (23), 11770-11779.
149. Conte, R.; Aspuru-Guzik, A.; Ceotto, M. *J. Phys. Chem. Lett.* **2013**, *4* (20), 3407-3412.
150. Borrelli, R.; Peluso, A. *J. Chem. Phys.* **2006**, *125* (19), 194308.
151. Borrelli, R.; Peluso, A. *J. Chem. Phys.* **2008**, *128* (4), 044303.
152. Capobianco, A.; Borrelli, R.; Noce, C.; Peluso, A. *Theor. Chem. Acc.* **2012**, *131* (3), 1-10.
153. Hazra, A.; Chang, H. H.; Nooijen, M. *J. Chem. Phys.* **2004**, *121* (5), 2125-2136.
154. Reimers, J. R. *J. Chem. Phys.* **2001**, *115* (20), 9103-9109.
155. Peluso, A.; Borrelli, R.; Capobianco, A. *J. Phys. Chem. A* **2009**, *113* (52), 14831-14837.
156. Douglas, A. E. *Discuss. Faraday Soc.* **1963**, *35* (0), 158-174.
157. Walsh, A. D.; Warsop, P. A. *Trans. Faraday Soc.* **1961**, *57* (0), 345-358.
158. Tang, S. L.; Imre, D. G.; Tannor, D. *J. Chem. Phys.* **1990**, *92* (10), 5919-5934.
159. Baronavski, A. P.; Owrutsky, J. C. *J. Phys. Chem.* **1995**, *99* (25), 10077-10080.
160. Wells, K. L.; Perriam, G.; Stavros, V. G. *J. Chem. Phys.* **2009**, *130* (7), 074308.
161. Giri, K.; Chapman, E.; Sanz, C. S.; Worth, G. *J. Chem. Phys.* **2011**, *135* (4), 044311.
162. Lai, W.; Lin, S. Y.; Xie, D.; Guo, H. *J. Chem. Phys.* **2008**, *129* (15), 154311.
163. Ma, J.; Xie, C.; Zhu, X.; Yarkony, D. R.; Xie, D.; Guo, H. *J. Phys. Chem. A* **2014**, *118* (51), 11926-11934.
164. Ma, J.; Zhu, X.; Guo, H.; Yarkony, D. R. *J. Chem. Phys.* **2012**, *137* (22), 22A541.



- 
165. Xie, C.; Ma, J.; Zhu, X.; Zhang, D. H.; Yarkony, D. R.; Xie, D.; Guo, H. *J. Phys. Chem. Lett.* **2014**, *5* (7), 1055-1060.
166. Edvardsson, D.; Baltzer, P.; Karlsson, L.; Wannberg, B.; Holland, D. M. P.; Shaw, D. A.; Rennie, E. E. *J. Phys. B: At., Mol. Opt. Phys.* **1999**, *32* (11), 2583.
167. Viel, A.; Einfeld, W.; Evenhuis, C. R.; Manthe, U. *Chem. Phys.* **2008**, *347* (1-3), 331-339.
168. Viel, A.; Einfeld, W.; Neumann, S.; Domcke, W.; Manthe, U. *J. Chem. Phys.* **2006**, *124* (21), 214306.
169. Woywod, C.; Scharfe, S.; Krawczyk, R.; Domcke, W.; Köppel, H. *J. Chem. Phys.* **2003**, *118* (13), 5880-5893.
170. Borrelli, R.; Capobianco, A.; Peluso, A. *Can. J. Chem.* **2013**, *91* (7), 495-504.
171. Mukamel, S.; Abe, S.; Islampour, R. *J. Phys. Chem.* **1985**, *89* (2), 201-204.
172. Werner, H. J.; Knowles, P. J.; Knizia, G.; Manby, F. R.; Schütz, M.; Celani, P.; Korona, T.; Lindh, R.; Mitrushenkov, A.; Rauhut, G., et al. *MOLPRO, version 2012.1, a package of ab initio programs*; Cardiff, UK, 2012.
173. Chen, F. Z.; Judge, D. L.; Wu, C. Y. R.; Caldwell, J. *Planet. Space Sci.* **1999**, *47* (1-2), 261-266.
174. Duschinsky, D. *Acta Physicochim. URSS* **1937**, *7*, 551.
175. Pavlov-Verevkin, V. B.; Leyh, B.; Lorquet, J. C. *Chem. Phys.* **1989**, *132* (1-2), 175-183.
176. Yan, Y. J.; Mukamel, S. *J. Chem. Phys.* **1986**, *85* (10), 5908-5923.
177. Wehrle, M.; Vaníček, J. *unpublished* **2015**.
178. Goletz, C.-M.; Koch, W.; Grossmann, F. *Chem. Phys.* **2010**, *375* (2-3), 227-233.
179. Goletz, C.-M.; Grossmann, F. *J. Chem. Phys.* **2009**, *130* (24), 244107.
180. Buchholz, M.; Goletz, C.-M.; Grossmann, F.; Schmidt, B.; Heyda, J.; Jungwirth, P. *J. Phys. Chem. A* **2012**, *116* (46), 11199-11210.
181. Braem, O.; Penfold, T. J.; Cannizzo, A.; Chergui, M. *Phys. Chem. Chem. Phys.* **2012**, *14* (10), 3513-3519.





## Marius Wehrle

Austrasse 13  
9242 Oberuzwil, Switzerland  
wehrle.marius@gmail.com

Nationality: Swiss  
Date of Birth: 24.5.1983

### Education

- present* Ph.D. Student in the Laboratory of Theoretical Physical Chemistry at EPFL, Switzerland
- 2010 Master of Science Msc in Molecular and Biological Chemistry, EPFL, Switzerland
- 2008 Bachelor of Science BSc in Chemistry and Chemical Engineering at EPFL, Switzerland
- 2006 Assessment year at the School of Criminal Justice (ESC), Unil, Switzerland

### Languages

- German Mother tongue
- English Fluent written and oral
- French Fluent written and oral

### Publications

- 2011 "Time-Resolved Electronic Spectra with Efficient Quantum Dynamics Methods" published in *CHIMIA* [Wehrle, M.; Šulc, M.; Vaniček, J. *Chimia* **2011**, 65 (5), 334-338]
- 2014 "On-the-Fly ab initio Semiclassical Dynamics: Identifying Degrees of Freedom Essential for Emission Spectra of Oligothiophenes" published in the *Journal of Chemical Physics* [Wehrle, M.; Šulc, M.; Vaniček, J. *J. Chem. Phys.* **2014**, 140 (24), 244114]
- 2015 "On-the-Fly ab initio Semiclassical Dynamics of Floppy Molecules: Absorption and Photoelectron Spectra of Ammonia" published in the *Journal of Physical Chemistry A* [Wehrle, M.; Oberli, S.; Vaniček, J. *J. Phys. Chem. A* **2015**, DOI:10.1021/acs.jpca.5b03907]

### Prizes

- 2011 Best Poster Award in Computational Chemistry – Swiss Chemical Society Fall Meeting.
- 2013 Teaching Excellency Award – École Polytechnique Fédérale de Lausanne.

### Passed exams

ATTENDED COURSES	LECTURERS	CREDITS
Computation of molecular properties	François Rotzinger	2
Density functional theory	Tomasz Adam Wesolowski	2
Electronic spectroscopy	Majed Chergui	3
Surface and thin films processes	Ayat Karimi	2
Ultrafast phenomena	Frank van Mourik	4